Scholars' Mine

Fall 2018

Bio-inspired geomaterial improvement and development of innovative characterization methods

Junnan Cao

Follow this and additional works at: https://scholarsmine.mst.edu/doctoral_dissertations

Part of the Civil Engineering Commons

Department: Civil, Architectural and Environmental Engineering

BIO-INSPIRED GEOMATERIAL IMPROVEMENT AND DEVELOPMENT OF

INNOVATIVE CHARACTERIZATION METHODS

by

JUNNAN CAO

A DISSERTATION

Presented to the Faculty of the Graduate School of the

MISSOURI UNIVERSITY OF SCIENCE AND TECHNOLOGY

In Partial Fulfillment of the Requirements for the Degree

DOCTOR OF PHILOSOPHY

in

CIVIL ENGINEERING

2018

Approved by:

Bate Bate, Advisor
Wen Deng, Co-advisor
Melanie Mormile
J. David Rogers
Jianmin Wang

PUBLICATION DISSERTATION OPTION

This dissertation has been prepared using publication option.

Paper I (pages 11-50) is a manuscript entitled "Influences of Size and Content of Enzyme Induced Calcite Precipitates on the Stiffness of A Fine Sand − A Spectral Induced Polarization Study." This manuscript is pending submission for publication in the *Journal of Geophysical Research – Biogeosciences*.

Paper II (pages 51-64) is a manuscript entitled "Complex Conductivity and Shear Wave Velocity Responses of Sand-Calcite Mixture." This manuscript was accepted for publication in the *8th International Congress on Environmental Geotechnics (ICEG2018), Hangzhou, China*.

Paper III (pages 65-97) is a manuscript entitled "Microscopic and Physicochemical Studies of Polymer – Modified Kaolinite Suspensions." This manuscript was published in the *Colloids and Surfaces A: Physicochemical and Engineering Aspects*.

Paper IV (pages 98-133) is a manuscript entitled "On the Soil Water Characteristic Curves of Poorly-Graded Granular Materials in Aqueous Polymer Solutions." This manuscript was published in the *Acta Geotechnica*.

Paper V (pages 134-154) is a manuscript entitled "Measuring Retardation Factors of ^{133}Cesium and ^{88}Strontium Cations Using Column Test." This manuscript is under review for publication in the *Journal of Geotechnical and Geoenvironmental Engineering-ASCE*.

ABSTRACT

This study experimentally investigated the bio-inspired improvement on geomaterials, including enzyme induced calcite precipitation (EICP) and biopolymers. This study also developed several innovative characterization tools to advance the state-of-the-art testing techniques, including SIP-BE column, rotational sedimental panel, and backpressure saturated constant hydraulic gradient break through column. Firstly, EICP test was performed on Ottawa 50-70 sand in a newly developed SIP-BE column. Non-destructive techniques – spectral induced polarization (SIP) and bender element were used to monitor the precipitation process and shear wave velocities (V_s). SIP, V_s, and SEM results all suggest contact cementation as the preferential precipitation pattern of calcite. Secondly, a series of sedimentation tests were conducted on kaolinite in biopolymers (xanthan gum, chitosan, polyacrylic acid and polyacrylamide) solutions with time-lapsed photography technique. The interaction mechanisms of biopolymers and kaolinite particles were revealed to be electrostatic force (xanthan gum), charge neutralization (chitosan and PAA) and steric stabilization (PAM), respectively. Thirdly, A column test setup was developed with constant hydraulic gradient and full soil sample saturation using a triaxial cell to measure the retardation factors (R_d) of Sr and Cs for natural silty sand. The measured R_d values of the tested sand for Sr and Cs were 3.561 and 27.369, respectively. The column setup developed in this study eliminates the uncertainties from partial saturation and fluctuating pressure difference across the sample column in a traditional flow-through column test setup, and is recommended to be used for future breakthrough curve measurements. In the study of SWCC, biopolymers were found to significantly increase the water retention capacity, especially at pendular regime.

ACKNOWLEDGMENTS

I would like to thank my advisor, Dr. Bate Bate, for his great advising, professional guidance and patient assistance during my Ph.D. study. Without his help, valuable suggestion and encouragement, this work would not be accomplished as smoothly as it was. Words cannot express how grateful I am to have such an amazing advisor.

I would like to thank my co-advisor, Dr. Wen Deng, and the members of my advisory committee, Dr. Melanie Mormile, Dr. J. David Rogers and Dr. Jianmin Wang, for their valuable suggestions and help on part of the chemical stuff and equipment that I used in my research. I want to thank Dr. Xiong Zhang for his encouragement and kind help on SEM tests during the last year of my Ph.D. study. I would like to thank Dr. David J. Westenberg for his valuable suggestions on the usage of microbial equipment. I also want to thank Dr. Estella A. Atekwana, Dr. Chi Zhang and Dr. Gamal Z. Abdel Aal for their valuable guidance on SIP configuration.

I would like to thank my graduate student colleagues, Xin Kang, Jianfeng Zhu, Xiaoyi Zhao and Chao Zeng, for their help on my experimental setup. Thanks also go to the civil department staff, Brian Swift, Gary Abbott, John Bullock, Greg Leckrone, and Mike Lusher, for their technical assistance and support.

I want to thank my husband, Song Wang, and our parents. Their love and support in my life are selfless and priceless. I also want to thank my lovely daughter, Selena Wang, who always cheers me up and makes me feel full of energy.

TABLE OF CONTENTS

LIST OF ILLUSTRATIONS

LIST OF TABLES

1. INTRODUCTION

1.1. RESEARCH OVERVIEW

Bio-inspired geomaterial improvement, as an emerging and promising method in ground soil improvement, includes biopolymers, biofilms, microbial induced calcite precipitation (MICP) and enzyme induced calcite precipitation (EICP). In MICP, bacteria work as a catalyst through generating urease enzyme to catalyze urea into carbonate ions (DeJong et al. 2006; van Paassen et al. 2010), whereas, free urease enzyme, instead of bacteria, is directly adopted in EICP to generate carbonate precipitation (Hamdan and Kavazanjian 2016; Hamdan et al. 2013). Both MICP and EICP are very suitable for the coarse-grained soil, such as sand, due to the relative sizes of soil particles and bacteria or enzyme (Mitchell and Santamarina 2005). Much research has been performed on MICP and EICP to investigate the permeability, shear strength, and unconfined compressive strength (DeJong et al. 2006; Hamdan and Kavazanjian 2016). The soils used in this study are typically Ottawa 50-70 and 20-30 sands. After the modification, the permeability was found to be reduced, while the soil strength, stiffness was reported to be enhanced. The disadvantages of MICP and EICP include high cost of nutrients (e.g. urea in ureolysis), environmental impacts, maintenance of anaerobic conditions in field and control of uniform distribution of bacteria. Biopolymers emerged as new engineering materials in recent decades due to their environmental-friendly nature, minimal carbon footprint, and high efficiency. Biofilms and biopolymers also have the potential to improve the shear strength, stiffness and erosion resistance behavior of geomaterials (Bate and Burns 2010; Kang and Bate 2016; Kim and Palomino 2009). Biopolymer modified soils have also been used as barrier materials for contaminant containment

before (Di Emidio et al. 2015; Di Molfetta and Sethi 2006). Although they have been successfully used in previous studies, a potential drawback is their long-term sustainability. For example, nutrients might be continuously needed for microorganisms to sustain biofilm production (DeJong et al. 2013).

Many behaviors of aforementioned bio-inspired engineered geomaterials are of interest to the academic study and engineering practice, including mechanical properties relevant to traditional geo-structures (strength, stiffness and hydraulic conductivity), chemical and physicochemical properties relevant to chemical transportation (retardation factor or distribution coefficient) and slurry deposition (zeta potential), conduction properties related to monitoring (electrical conductivity and shear wave velocity) and unsaturation properties relevant to matric suction and water retention (Soil-water characteristic curve). Several new characterization testing systems were developed to advance current state-of-the-practice methods, including time-lapsed photography of a sedimentation panel, backpressured breakthrough column with constant hydraulic gradient, spectral induced polarization (SIP)-bender element composite testing system, and a hanging column attachment in conjunction with Tempe cell so as to unveil characteristics of bio-inspired geomaterials that were not observed previously.

1.2. OBJECTIVE AND SCOPE OF RESEARCH

The primary objective of this research is to investigate biopolymer and EICP modification methods, with several proposed improvement on the traditional test methods. A pilot study to monitor 100% eggshell power (the substitution of $CaCO_3$) and Ottawa sand mixtures by spectral induced polarization (SIP) and bender element (BE) two non-destructive techniques was initiated, to investigate the relationship between the

precipitated particles and stiffness properties of geomaterial. Secondly, a SIP-BE column was designed to conduct the enzyme induced calcite precipitation (EICP) bioremediation method, and to well elucidate the relationships between the electrical conductivity, shear wave velocity, precipitated particle size, $CaCO_3$ solid contents and association patterns. For the biopolymer section, sedimentation tests are initially performed on fine-grained kaolinite suspensions in four different biopolymer mixtures with time-lapsed photography recording, to extensively investigate the fundamental mechanisms on the effects of biopolymer with kaolinite. Secondly, soil-water characteristic curves (SWCC) are measured by a newly developed hanging column attachment to reveal the unsaturated properties of polymer modified geomaterials. And finally, a new flow-through column test setup is proposed to provide more accurate retardation factors, one of the most important parameters in the improvement of containment and pollutant remediation by bio-inspired geomaterials.

The scope of this study is:

(1) Review the relative literatures;

(2) Develop four experimental setups: time-lapsed photography of a sedimentation panel, backpressured breakthrough column with constant hydraulic gradient, spectral induced polarization (SIP)-bender element composite testing system, and a hanging column attachment in conjunction with Tempe cell;

(3) Perform relative tests on enzyme induced calcite precipitation (EICP) with Ottawa 50-70 sands, kaolinite-biopolymer sedimentations, soil-water characteristic curve (SWCC) and measurement of retardation factors;

(4) Investigate relationships between precipitate characteristics and the stiffness properties of geomaterials, and elucidate fundamental mechanisms between biopolymers and engineering soils;

(5) Summarize major findings, make conclusions and develop recommendations.

1.3. DISSERTATION OUTLINE

This dissertation contains three sections. Section 1 includes a brief background introduction, research significance, primary objective and scope of work. Section 2 includes a detailed literature review establishing the state-of-the-art. Paper section includes five journal papers that present experimental investigations of conduction, unsaturation, mechanical and physicochemical properties, fundamental interaction mechanisms and monitoring techniques on EICP and biopolymers modified geomaterials. Section 3 summarizes all the work done in this study, major findings and conclusions, and also a proposal for future research.

2. LITERATURE REVIEW

2.1. MICROBIAL AND ENZYME INDUCED CALCITE PRECIPITATION

Microbial induced calcite precipitation (MICP) and enzyme induced calcite precipitation (EICP) are two recognized modification methods used in bioremediation, as demonstrated with many laboratory investigations and one field application (DeJong et al. 2006; DeJong et al. 2013; Kavazanjian and Hamdan 2015; Kavazanjian and O'Donnell 2015; Weil et al. 2012; Whiffin et al. 2007). MICP was successfully used in many areas including slope stability (Salifu et al. 2016), erosion control (Jiang et al. 2017; Maleki et al. 2016), bearing capacity of shallow foundations (Martinez and DeJong 2009), dust control (Hamdan and Kavazanjian 2016) and liquefaction (Montoya et al. 2012). For example, DeJong et al. (2006) successfully developed a treatment procedure to enhance the uncemented cohesionless soil by using *Bacillus pasteurii* bacteria. After the modification, they observed that the undrained monotonic shear capacity increased, as well as the initial shear stiffness and elastic capacity compared to untreated loose specimens. Lin et al. (2016) performed MICP on treatment of Ottawa 20-30 and 50-70 sands before using drained triaxial and confined compression tests with P-wave and S-wave velocity measurements. Their experimental results showed that the peak deviator stress of Ottawa 20-30 with 1.6% calcium carbonate and Ottawa 50-70 with 1% calcium carbonate increased by an average of 93% and 171% respectively after the treatment. In addition, the increased shear wave velocity, peak shear strength and cohesion were also reported in this study. Both MICP and EICP are suitable for the coarse-grained soils with pore sizes larger than the size of bacteria. Even though advantages such as the significantly increment of compressive and shear strength were studied for MICP, bio-

clogging and generation of toxic affiliations were also encountered during the application. Due to these limitations, ground improvement using MICP met a lot of challenges.

The first and only field application of MICP was performed by van Paasson in 2011 on bio-grouting the granular soils in Netherlands. Even though the measured result on disturbed soil samples taken from excavation demonstrated that up to 6% of the total dry weight calcium carbonate was generated in this modification, effective monitoring tools were lacking. Providing evidence and efficiency of cementation after the treatment was very difficult. In addition, significant heterogeneity was also observed in this study.

Enzyme induced calcite precipitation (EICP) by using plant derived urease enzyme instead of bacteria exhibited many advantages and solved the major problems occurred in MICP. Unlike the bacteria, urease enzyme could be evenly distributed among soil particles. It would not accumulate near the nutrients injection points. In addition, the small size (on the order of 10nm) of enzyme molecules could also significantly mitigate bio-clogging allowing it penetrate into the fine-grained soils such as silt (Kavazanjian and Hamdan 2015). Many studies have been done on EICP modified sandy soils (Hamdan and Kavazanjian 2016; Kavazanjian and Hamdan 2015). One experiment was conducted by Kavazanjian and Hamdan (2015) on sand columns. After treatment, peak unconfined compressive strengths equaled 529 kPa and 391 kPa were reported for Ottawa 20-30 sand at 0.8% axial strain and F-60 sand at 1.7% axial strain, respectively. Until now, most EICP studies were mainly focused on investigation of the mechanical properties relevant to traditional geo-structures such as strength, stiffness and hydraulic conductivity. However, the conduction properties such as electrical conductivity and shear wave velocity have rarely been investigated. In additions, relationships between

conduction/polarization and mechanical properties (shear wave velocity, hydraulic conductivity) also need to be elucidated. Of note, precipitated $CaCO_3$ particle size and distribution in EICP could significantly influence the efficiency of ground soil improvement. The direct measurement of these precipitated particles poses challenges to the existing non-destructive methods.

2.2. BIOPOLYMER MODIFIED ENGINEERING SOIL

Biopolymer modification has been widely used in several applications, including chemical enhanced oil recovery (Espinasse and Siffert 1979; Pefferkorn 1999), soil erosion control (Lentz and Sojka 2000; Lentz et al. 1992; Nugent et al. 2010), dewatering of mine tailings (Beier et al. 2013; McFarlane et al. 2006; Mpofu et al. 2003), dredging of sediments (Hunter et al. 2006; Wang and Chen 1977), waste water treatment (Letterman and Pero 1990) and soil stabilizations (Ates 2013; Kang and Bate 2016). The most widely used biopolymers include xanthan gum, guar gum, chitosan, polyacrylic acid (PAA), polyacrylamide (PAM) and so on. Xanthan gum, a component of biofilm derived from the bacterium, *Xanthomonas campestris*, is reported to increase the shear strength of sand from 30 kPa to 190 kPa with only up to 5% (by weight) addition (Çabalar and Çanakci 2005). Xanthan gum and guar gum were also used to stabilize mine tailings with measured increment in liquid limit and undrained shear strength before (Chen et al. 2013). Despite these applications and advantages, the interaction mechanisms between polymers and soil particles have not been fully explored.

Currently, most of the studies on polymer modified geomaterials focused on evaluating their large strain strength, small strain stiffness, hydraulic conductivity and erosion resistance properties in saturated conditions. However, only a few studies

investigated those properties at unsaturated conditions (Cao et al. 2016; Jung and Jang 2016; Puppala et al. 2006). Desaturation could result in dramatically change on mechanical properties of geomaterials, as reported by previous studies (Bate and Zhang, 2013; Fredlund et al. 1994).

2.3. SOIL WATER CHARACTERISTIC CURVE

Bio-inspired geomaterials, such as organoclays, could have significant improvement in the containment and remediation of pollutants (Bate and Burns 2010; Javadi et al. 2017). Polymeric solutions retention and transportation in porous media are commonly seen phenomena found in many engineering fields including soil contaminant containment barriers (Di Emidio et al. 2015; Javadi et al. 2017; Scalia et al. 2014; Zhao et al. 2017) and bioremediation of geomaterials (Ivanov and Chu 2008; Yeom et al. 2010).

Most current work on polymer modified geomaterials has focused on evaluating their swelling/shrinkage, large strain strength, small strain stiffness, hydraulic conductivity and erosion resistance properties in either saturated or compacted condition. Only a few studies controlled for unsaturation conditions, such as matric suction (Cao et al. 2016; Jung and Jang 2016; Puppala et al. 2006). Under field conditions, however, soils are not always saturated due to seasonal groundwater level change, precipitation, and evaporation, or in the applications like soil vapor sparging, CO_2 sequestration, shale gas production, imbibition, contaminant transport and petroleum leakage onto soil particle surface, and projects involving methane hydrate (Dai et al. 2012; Espinoza and Santamarina 2010). Due to the variability of polymeric solutions, the viscosity, surface tension and the contact angle between liquid and porous media varies. This will lead to highly variable flow behaviors and liquid retention capability of the hosting porous media.

Once desaturation occurs, the mechanical properties of geomaterials could change drastically (Bate and Zhang 2013; Fredlund et al. 2012; Lu 2016; Lu et al. 2009; Lu et al. 2007; Mitarai and Nori 2006).

2.4. MEASUREMENT OF RETARDATION FACTOR

Batch and flow-through column test are the two most commonly used methods to measure retardation factor (USEPA 1999). Batch test often identifies soil properties when contaminants are thoroughly mixed with soils, or are at equilibrium in adsorption and ion exchange with soils; while column test simulates contaminant transport process under hydraulic and mechanical conditions similar to those in the field, and mimics the process of contaminant persistence in soil column in terms of breakthrough curve (BTC). Therefore, column tests are residence time dependent (Reddy and Al-Hamdan 2013; Reddy et al. 2011).

A well-detailed procedure for column test is provided by USEPA (1999). However, a major disadvantage of the USEPA method is its inability to guarantee sample saturation (van Genuchten and Wierenga 1986). Hydraulic conductivity (k) of a porous medium, which the flow rate is proportional to, is highly dependent on the degree of saturation, as several orders of magnitude reduction in k could occur when the degree of saturation decreases by only 20% (Fredlund et al. 2012). Backpressure (ASTM D5084-16a), or pressurizing the soil sample with additional pore water pressure, is the primary technique used to increase the degree of saturation of a soil sample. Redmond and Shackelford (1994) used backpressure and a constant flow rate column setup by automated syringe control. Javadi et al. (2017) used backpressure and falling head column setup with fluctuating hydraulic gradient. To date, backpressure has not been

used under constant hydraulic gradient testing setup. Another disadvantage of the USEPA method is the side leakage-prone rigid wall design, a problem especially pronounced for coarse-grained materials, such as gravel and sand.

PAPER

I. INFLUENCES OF SIZE AND CONTENT OF ENZYME INDUCED CALCITE PRECIPITATIONS ON THE STIFFNESS OF A FINE SAND-A SPECTRAL INDUCED POLARIZATION STUDY

Junnan Cao[1], Bate Bate[2] and Chi Zhang[3]

[1]Graduate Research Assistant, Department of Civil, Architectural, and Environmental Engineering, 1401 North Pine Street, Missouri University of Science and Technology, Rolla, MO 65409. Email: jcg83@mst.edu

[2]Research Professor, Institute of Geotechnical Engineering, College of Civil Engineering and Architecture, Zhejiang University, 866 Yuhangtang Road, Hangzhou, China 310058. Email: batebate@zju.edu.cn; Formerly, Assistant Professor, Department of Civil, Architectural, and Environmental Engineering, 1401 North Pine Street, Missouri University of Science and Technology, Rolla, MO 65409

[3]Assistant Professor, College of Liberal Arts and Sciences – Geology, University of Kansas, chizhang@ku.edu

ABSTRACT

Enzyme induce calcite precipitation (EICP) was conducted in this study. Ottawa 50-70 sands were evenly mixed with urease enzyme and packed in a new developed SIP-BE column. Urea and calcium chloride solutions were amended into soil sample to generate calcite precipitations. Two non-destructive techniques, spectral induced polarization and bender elements were used to monitor the catalytic reaction process of calcite precipitation in EICP and shear wave velocity of the enhanced sand, respectively. Two precipitation characteristics, particle size and calcite content, could be obtained from the peak frequency and chargeability of SIP. In order to elucidate the relationship between characteristics of precipitations and stiffness properties of geomaterials, three

conceptually association models with β parameter representing the association patterns were postulated. It was found that β equaled to 2/3, 1 and 0 for uniform surface coating, perfect contact cementation and pore filling respectively. β value was around 3.4 in this study suggesting that the contact cementation held the larger possibility to dominant the EICP of this study. The possible reason for this association pattern was attributed to the formation of stationary eddies at the pore throats among sand particles in Darcy flow and the nucleation of calcite crystals.

KEYWORDS: EICP, spectral induced polarization, shear wave velocity, precipitated particle size, solid content, stiffness, association pattern, eddy, nucleation.

1. INTRODUCTION

The use of biological systems for engineering applications has drawn attention for decades ((DeJong et al. 2014; DeJong et al. 2006; Hamdan and Kavazanjian 2016). For example, microbial induced calcite precipitation (MICP) has been extensively investigated (DeJong et al. 2014; DeJong et al. 2006; Whiffin et al. 2007). It holds promising potential applications in slope stability (Salifu et al. 2016), erosion control (Jiang et al. 2017; Maleki et al. 2016), bearing capacity of shallow foundations (Martinez and DeJong 2009), dust control (Hamdan and Kavazanjian 2016) and liquefaction mitigation (Islam et al. 2018; Montoya et al. 2012). It is suitable for the coarse-grained soils with pore sizes larger than the size of bacteria. Even though advantages such as a significantly increment of compressive and shear strength, were identified, bio-clogging and generation of toxic byproducts (such as ammonium, nitrite and nitric oxide) were

also encountered during the application. Due to these limitations, ground improvement by using MICP was met many challenges to implementation. Enzyme induced calcite precipitation (EICP), using plant derived urease enzyme instead of bacteria, provides many advantages and resolves the disadvantages of MICP. When the urea-$CaCl_2$ mixture solution was injected into a soil matrix pre-treated with urease enzyme, either by deep soil mixing or injecting, the enzyme starts to catalyze urea into NH_4^+ and CO_3^{2-} progressively. The produced CO_3^{2-} then reacts with Ca^{2+} immediately to form calcium carbonate (calcite) precipitation. The formula of chemical reaction is shown below:

$$CO(NH_2)_2 + 2H_2O + CaCl_2 = CaCO_3 \downarrow + 2NH_4Cl \qquad (1)$$
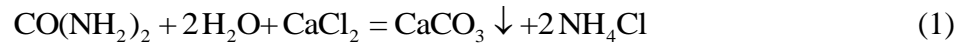
Due to the small size of the enzyme molecules (on the order of 10 nm) (Kavazanjian and Hamdan 2015) bio-clogging can be mitigated.

Many studies have been performed on MICP and EICP (DeJong et al. 2006; Hamdan and Kavazanjian 2016; Weil et al. 2012). However, the investigations were primarily focused at the laboratory scale. Until now, there was only one field application case reported. It was conducted by van Paasson (van Paassen 2011). He used MICP method to bio-grout the granular soils in Netherlands. After the treatment, significant soil heterogeneity was observed. Besides the high cost of this project, another disadvantage was the lack of efficient monitoring tools to provide information on the effect of the bio-grouting.

In addition, the size, content, and distribution of $CaCO_3$ precipitates generated in MICP and EICP in the geomaterial matrix are the fundamental governing factors (Fernandez Santamarina 2001; DeJong et al. 2006) for the improvement of mechanical properties. Direct measurement of these precipitated particles, however, poses challenges

when existing non-destructive methods are used. Spectral induced polarization (SIP), an emerging noninvasive geophysical method that quantifies the low frequency (usually from 0.001 Hz to 100 Hz) complex conductivity (σ^*) and is used to determine the accompany polarization mechanisms of a multiphase porous medium (eg. glass bead and sand), and has shown great promise in obtaining the size, content, and accumulation pattern of $CaCO_3$ precipitates. Laboratory column SIP test is often performed using two current electrodes to generate alternating current at a prescribed frequency range across the sample, and using multiple pairs of potential electrodes to detect the potential between each pair of electrodes (Breede et al. 2011; Revil 2012). Generally, the precipitates are negatively charged. After generating the alternative current, ions in the electrical double layers move to the direction of the current direction, resulting in the local current changes around the particles. Since this phenomenon can be detected by SIP potential electrodes, the signal from SIP is postulated to be a reflection of characteristics of the precipitations by two parameters: one is the relaxation time, reflecting the precipitated particle size; another is the chargeability, relating to the solid content of the precipitated particles.

Spectral induced polarization has been applied in monitoring the process of calcite precipitation (Wu et al. 2010), zero valence iron oxidation (Wu et al. 2005), mineral precipitation in porous media (Zhang et al. 2012), MICP (Kruschwitz et al. 2016) and biofilm formation (Abdel et al. 2004; Atekwana and Slater 2009). However, no studies were found to be done by using EICP. Moreover, as opposed to the presence of complicated microbial populations in MICP processes, the reactants and the products during an EICP process are an enzyme and simple chemical compounds (Eq. 1), which

facilitates SIP detection of the characteristics of the precipitates. Prior studies on EICP modified sandy soils mainly focused on the mechanical properties, such as strength, stiffness and hydraulic conductivity (Hamdan and Kavazanjian 2016; Kavazanjian and Hamdan 2015). However, conduction properties, such as electrical conductivity and mechanical wave conduction, have rarely been reported. Relationship between conduction and mechanical properties (shear wave velocity, hydraulic conductivity) also needs to be elucidated. Therefore, EICP was selected as a pilot study for this research.

The goal of this study is to better understand the relationships between calcite precipitate characteristics and the stiffness properties of geomaterials. The following tasks were performed: 1. A SIP-BE column was developed for the measurement of SIP and shear wave velocity simultaneously. 2. SIP monitors the whole precipitation process during the reaction and bender elements detect the shear wave velocities of the enhanced sands. 3. Relationships between the electrical conductivity, shear wave velocity, precipitated particle size, $CaCO_3$ solid contents, particle distributions and association patterns are finally well elucidated.

2. BACKGROUND

2.1. SPECTRAL INDUCED POLARIZATION

The spectral induced polarization or complex conductivity can be expressed as

$$\sigma^*(\omega) = \sigma'(\omega) + i\sigma''(\omega) \tag{2}$$

where ω is the angular frequency, σ' the real conductivity that represents the conduction (or energy loss) component, σ'' the imaginary conductivity that represents the

polarization (or energy storage) component (Knight and Nur 1987; Slater and Lesmes 2002; Zhang et al. 2012), and $i = \sqrt{-1}$. Alternatively,

$$\sigma' = |\sigma| \cos\varphi \tag{3}$$

$$\sigma'' = |\sigma| \sin\varphi \tag{4}$$

where $|\sigma|$ is the conductivity magnitude, and φ the phase shift.

In a multiphase porous medium, two pathways exist for the transfer of electric field, namely electrolytic conduction that occurs in the fluid-filled pore spaces inside the solid matrix, and surface conduction that occurs through the electrical double layer (EDL) adjacent to the liquid-solid interfaces. Theoretically, the differential effective medium theory can be used to model the complex conductivity properties of porous media, which relates to the intrinsic electrical properties and the shape of particles in the porous media (Slater and Lesmes 2002). Simply, it is assumed that above two pathways can be superposed in parallel (Börner et al. 1996; Lesmes and Frye 2001; Slater and Lesmes 2002; Vinegar and Waxman 1984; Waxman and Smits 1968); although Revil (2012) suggested that the assumption of parallel pathways may not always be true, the diffuse layer nature of surface conductivity at very low salinities should also be considered. Therefore, the complex conductivity of a saturated porous medium at low frequencies ($<$ 1000 Hz) can be generally written as

$$\sigma^* = \sigma_{el} + \sigma^*_{surf}(\omega) = \sigma_{el} + \sigma'_{surf}(\omega) + i\sigma''_{surf}(\omega) \tag{5}$$

where σ_{el} is the DC conductivity of the electrolytes in the pore space, $\sigma'_{surf}(\omega)$ and $\sigma''_{surf}(\omega)$ are the frequency-dependent real and imaginary components of the surface complex conductivity (σ^*_{surf}). DC conductivity σ_{el} is governed by the DC conductivity of pore

fluid (σ_f), porosity (n) and connectivity of the electrolyte filled pore space. In a saturated medium, σ_{el} is well characterized by Archie's law (Archie 1942):

$$\sigma_{el} = a \cdot \sigma_f \cdot (n)^b = (1/F) \cdot \sigma_f \tag{6}$$

where a and b are parameters related to the tortuosity of the pore space, F is the formation resistivity factor.

Surface complex conductivity relates to medium mineralogy, particle size and electrical conductivity of pore fluid (Breede et al. 2011). Cole-Cole model is often used to describe the complex conductivity (σ^*) of geomaterials (Cole and Cole 1941; Pelton et al. 1978; Wu et al. 2010), the equation is shown below

$$\sigma^*(\omega) = \sigma_0 \left[1 + m \left(\frac{(i\omega\tau)^c}{1 + (i\omega\tau)^c (1+m)} \right) \right] \tag{7}$$

where σ_0 is the DC conductivity; $m = 1 - \sigma_0/\sigma_\infty$ is the chargeability, representing the polarization magnitude; σ_∞ the conductivity at high frequency; c the shape parameter, ranging from 0.2 to 0.8 for unconsolidated soils (Zhang et al. 2012); τ the mean relaxation time, which is related to the particle/pore size. Typically, parameter m_n ($= m \times \sigma_0$) is often adopted to represent global measures of induced polarization magnitude (Lesmes and Frye 2001). τ (s) and particle diameter d (m) can be related by (Schwarz (1962)):

$$\tau = \frac{d^2}{8D_s} \tag{8}$$

where D_s is the diffusion coefficient (m^2/s). Many other studies (Kruschwitz et al. 2010; Revil et al. 2012; Scott and Barker 2003) also reported positive correlations between

mean relaxation time τ and pore throat size Λ for granular materials with average pore size of over 10 μm:

$$\tau = \frac{\Lambda^2}{2D_s}$$

(9)

2.2. BENDER ELEMENT

Bender element (BE) is a nondestructive method to measure the shear wave velocity (V_s) of geomaterials (P.V. Lade 2016; Lee and Santamarina 2005; Bate et al. 2013 SDEE; Zhu et al. 2018), which, in turn, can be converted to the shear modulus (G_0) by:

$$G_0 = \rho V_s^2$$

(10)

The tip-to-tip distance (L) was selected as the travel distance. The first arrival time (t_c) was determined using the zero-crossing point with the x-axis of the half peak before the first major peak (Lee and Santamarina 2005). Shear wave velocity (m/s) is then calculated by

$$V_s = \frac{L}{t_c}$$

(11)

3. MATERIALS AND EXPERIMENTAL METHODS

3.1. MATERIALS

Ottawa 50-70 silica sand (U.S. Silica Holdings Inc., Chicago, IL) with a particle diameter at 50% finer by mass (d_{50}) of 0.26 mm, maximum (e_{max}) and minimum (e_{min}) void ratios of 0.87 and 0.55, was used. Urease enzyme (Acros Organics, CAS: 9002-13-

5), urea (Acros Organics, CAS: 57-13-6) and $CaCl_2$ (Acros Organics, CAS: 10043-52-4) were used as received.

3.2. SIP-BE COLUMN SETUP

The spectral induced polarization-bender element column (short as SIP-BE column) is consisted of an acrylic tube (30cm in length and 10cm in inner diameter) with pre-drilled holes for SIP electrodes or bender elements, acrylic cap that can move vertically, base, two copper plates (10cm in diameter and 0.5 cm in thickness) embedded into the cap and base to exert a uniform current through cross-section of the column specimen for SIP measurement (Fig. 1b). Five Ag/AgCl electrodes were installed into the pre-drilled holes along the side of glass tube with 5 cm apart as potential electrodes for SIP measurement (Fig. 1b). A pair of BE was installed at the center of top and bottom plates. Another five BE pairs were installed along the side of the tube with 5cm apart. Urea and $CaCl_2$ solution is introduced from the base and discharged from the cap (Fig. 1b). O-rings were used so as to avoid both fluid leakage and the unwanted side transmission of mechanical waves (Fig. 1c and d). The bottom two rows of bender elements and Ag/AgCl electrodes were used in this study.

3.3. SAMPLE PREPARATION AND NUTRIENT INJECTION SEQUENCE

Ottawa sand was firstly immersed in 91% isopropyl alcohol for 24 hours, and then washed with deionized water at least five times, oven-dried (100 °C) for 24 hours before usage. 1954 grams of sands thoroughly mixed with 6.5 grams of urease enzyme was air pluviated into the SIP/BE column (Bate and Zhang 2013) and tamped into a final height of 15cm, and a relative density (D_r) of 85% (void ratio of 0.598, porosity of 0.37) (Fig.

1a). Vertical stress of 5kPa was then applied to the sample cap via a loadframe (Master loader HM-3000, Humboldt MFG. CO., Norridge, IL). A pore volume (PV) (approximately 441 ml) of the nutrient solution (0.05M urea and 0.05 M $CaCl_2$) was pumped into the sample with a peristaltic pump (Fig.1a) at a flow rate of 5 ml/min. About 90 min later, the sample was closed for 24 - 36 hours to ensure sufficient time for the chemical reaction to reach equilibrium (as suggested by both the constant real conductivity from SIP measurement and the constant V_s signals from bender element testing, see also the Discussion). Then another pore volume of the nutrient solution was pumped into the sample. Meanwhile, the DC conductivity of the outflow fluid was measured (Fisher Scientific, XL 60 conductivity probe). This procedure was repeated for the first 6 pore volumes. From the 7th to the 10th PV, the concentration of $CaCl_2$ solution in the nutrient solution was increased to 0.4M to accelerate calcite precipitation. Test was ended when the theoretical amount of $CaCO_3$ precipitation reached 4% by weight.

After that, the cemented soil sample was then extruded and cut into approximately four equal parts (Fig. 1e) to determine $CaCO_3$ content via acid digestion(Kavazanjian et al. 2015; Lin et al. 2016). Firstly, the samples were washed with deionized water five times and then oven dried for 48h. The dry sample mass were measured. Secondly, the samples were digested with 350ml 1M HCl 10 hours to remove $CaCO_3$ before being washed with deionized water five times and oven-dried for 24 hours. Finally, the $CaCO_3$ content was calculated according to the weight difference before and after digestion for each part.

3.4. PREPARATION OF BENDER ELEMENT AND TESTING SYSTEM

The BE testing system used in this study consisted of five pairs of bender elements, a waveform generator (33210A, Agilent), a filter (3364, Krohn-Hite), a signal amplifier and an oscilloscope (54622A, Agilent) (Fig. 1a).

BE testing system used in this study is similar to that used in prior studies of the authors (Kang and Bate 2016; Kang et al. 2014; Zhu et al. 2018), and a brief description was given below. The trimmed piezoceramic plate (Piezo Systems, Inc.) (12.7mm $\times$ 8.0 mm $\times$ 0.6mm, length $\times$ width $\times$ thickness) was connected to a coaxial cable in parallel to minimize the electromagnetic coupling (Lee and Santamarina 2005) , coated with at least three layers of polyurethane as the electrical isolator and waterproofing, and fixed in a nylon screw (inner diameter $\times$ height = 12.7mm $\times$ 15.88mm) by epoxy with 5 mm-long tip extruded in the air (Fig. 1d). The extruded portion was also coated with epoxy for protection and covered with plastic wrap to minimize crosstalk (Zhu et al. 2018).

3.5. IMAGING WITH SEM AND EDS

SEM samples were taken from the four parts mentioned above separately at least three for each part. Energy dispersive X-ray spectroscopy (EDS) was also conducted at the same time with SEM to elaborate Si and Ca mapping.

4. RESULTS

4.1. TYPICAL SIP RESULTS

Typical real and imaginary conductivities in low frequency spectrum (0.001 Hz – 100 Hz) (Fig. 2), as during the 4th and 7th pore volume injections, revealed the following

trends: (1) real conductivity increased slightly (4th PV: from 0.195 to 0.217 S/m, 7th PV: 1.255 to 1.380 S/m) towards an asymptotic value with time; (2) drastic changes initially, followed by stable values after approximate 21h (4th PV) to 28h (7th PV) were observed for imaginary conductivities; (3) two peak frequencies were presented on imaginary conductivity curves for both pore volumes: 0.5-2.5Hz and 0.01-0.1Hz for the 4th PV, and 3-20Hz and < 0.01Hz for the 7th PV; (4) magnitudes of imaginary conductivity at the dominant peak frequencies increased with time. The real conductivity (σ') trends reflect the enzyme reactions of calcite precipitation as shown in Eq. 1. Real conductivity at 1Hz evolution curves of selected injected pore volumes (Fig. 3) demonstrated that σ' increased slightly at the first 8-10 hours due to depletion of $CaCO_3$ and the generation of NH_4Cl during EICP reaction, and then became constant afterward due to the cessation of the chemical reaction. DC conductivity of outflow fluid (σ_f) has similar trends as the real conductivities at equilibrium (Fig. 4). This suggested that electrolytic DC conductivity (σ_{el}) was the major component of real conductivity. In addition, σ' and σ_f were proportional throughout the experiment (average σ': σ_f = 0.226:1.088 S/m for 1st-6th PV, 1.33:6.206 S/m for 7th-10th PV), confirming the dominance of σ_{el} on total σ'. With Eq. 6, the formation factor (F) of the sand sample column was 4.64. The evolution of imaginary conductivity reveals information regarding the characteristics of precipitates, as will be elaborated on in Discussion.

4.2. BENDER ELEMENT RESULTS

Shear wave velocities generally increased monotonically with injections of nutrients (Fig. 5), which is reasonably due to the continuous generation of $CaCO_3$ precipitates within the solid skeleton. Differences among the four pairs of bender

elements suggested the heterogeneous property of sands after the treatment. In fact, large CaCO$_3$ /sand solids were indeed observed near BE-1 and 3 (close to the injection point) (Fig. 7c and e) after the sample being extruded. Even though the soil mixture was still soft near BE-2 and 4, SEM image (Fig. 7d and f) revealed the precipitation of CaCO$_3$ among sand particles. Shear wave velocity curves at equilibrium with mass percentage of CaCO$_3$ were demonstrated in Fig. 6, as followed by the experimental results from Martinez et al. (2013) on MICP column test in Ottawa 50-70 sand (relative density > 100%). Similar trend but relatively higher V_s values were measured in this study.

Fig. 7 summarized the normalized shear wave velocity versus CaCO$_3$ content for this study (D_r = 85%), Kavazanjian et al. (2015), DeJong et al. (2014) and Weil et al. (2012). Similar with this study, DeJong et al. (2014) and Weil et al. (2011) performed the tests in Ottawa 50-70 sand but with MICP method. The relative densities were 84% and 40-60%, respectively. Kavazanjian et al. (2015) conducted the test in Ottawa 20-30 sand (D_r = 45%) with denitrification method. The data showed that V_s/V_0 values were close to each other when CaCO$_3$ content < 1.0% for all studies even though the sand types and relative densities were different. Similar trends were observed for this study and DeJong et al. in the whole tested CaCO$_3$ content range. This was probably due to the very close initial relative density of Ottawa sand and similar experimental conditions (non-continuous inflow injection). Significantly higher V_s/V_0 values were detected in Weil et al. study, especially when CaCO$_3$ content > 1.5%. One of the possible reasons could be the higher vertical stress added on the top of soil samples in Weil et al. study (100kPa > 5kPa of this study).

4.3. SEM AND EDS RESULTS

SEM and EDS images were exhibited in Fig. 8. It was observed that: (1) urease enzyme could attach on the surface of sand particles possibly by electrostatic force after being thoroughly mixed (Fig. 8b); (2) Images (Fig. 8c-f) for the treated sands near the four individual bender elements elucidated significant heterogeneity of soil. More calcite precipitated near BE-1 and 3; (3) EDS image (Fig. 8g) clearly showed the contact cementation association pattern among sand particles; and (4) different sizes of calcite-soil clusters were generated during the process of EICP (Fig. 8h).

5. DISCUSSION

5.1. EVOLUTION OF MEAN PARTICLE SIZE

The imaginary conductivity at equilibrium versus frequency curves for each pore volume were shown in Fig. 9. From which, the mean particle diameter could be calculated with Schwarz equation (Eq. 8), whereas the mean relaxation time (τ) in Eq. 8 is the inverse of the frequency corresponding to the peak imaginary conductivity. Diffusion coefficients of 1.838×10^{-9} m^2/s and 1.883×10^{-9} m^2/s (for 0.1 M and 0.7 M NH$_4$Cl solutions, respectively) (Hall et al. 1953) were adopted. The calculated average calcite precipitation diameters (0.086 to 0.543 mm) (Table 1) were comparable with sand particles (0.212 – 0.300 mm) in the first 4 pore volumes. Larger calculated average precipitate diameters (0.068 to 1.530 mm) were obtained during the 5th to the10th PV. This was postulated to be due to the attachment of CaCO$_3$ on the surface of Ottawa sand (1st-4th PV) and the forming of aggregates or clusters of calcite with sand particles (5th -

10th PV). This postulation was vindicated/supported/substantiated by the increasing shear wave velocities (Fig. 5) and SEM images (Fig. 8).

5.2. CALCULATION OF CaCO$_3$ CONTENTS

CaCO$_3$ content (CaCO$_3$ mass/sand mass) could be obtained from the normalized chargeability – m_n parameter in Cole-Cole model (Eq. 7). m_n, similar with imaginary conductivity (σ''), is another parameter reflecting the induced polarization magnitude. As the solid contents of CaCO$_3$ increase, the specific surface areas of precipitates increase as well, resulting in the increased surface charges and thereby the imaginary conductivity. The relation between m_n and CaCO$_3$ content was depicted in Fig. 10. It was found that cumulative gamma distribution was the best fitting curve for m_n versus CaCO$_3$% with R^2 = 0.989. Equation for the fitting curve was also shown in the figure. Wu et al. (2010) performed laboratory calcite precipitation test before by inducing CaCl$_2$ and Na$_2$CO$_3$ into 3mm glass beads packed column. Linear relationship between m_n and CaCO$_3$ content was observed before the occurrence of pore clogging in their study (Fig. 10). The curve for imaginary conductivity (σ'') at major peak frequency versus CaCO$_3$ solid content was also plotted as a reference in the figure. Similar trend with m_n was observed.

Actual mass percentage of CaCO$_3$ produced in each PV could be calculated from Eq. 1 and concentrations of NH$_4$Cl (two times of CaCO$_3$ concentration). Concentration of NH$_4$Cl could be derived from outflow conductivities (Fig. 4) if outflow solution was assumed to be pure NH$_4$Cl. The calculated mass percentages of CaCO$_3$ with the theoretical values were listed in Table 2. It was observed that calculated and theoretical mass percentage were almost the same for 1st - 6th pore volume (0.05M urea + CaCl$_2$) and calculated mass% = 74%-78% theoretical values for 7th – 10th pore volume (0.4M urea +

CaCl$_2$). The precipitation efficiency of EICP in this study was higher than the maximum efficiency of 66% of the MICP on Ottawa 50-70 sand ($Dr = 80\text{-}100\%$) by Martinez et al. (2013). This was probably due to the relative longer reaction time, low flow rate and more uniform distribution of urease enzyme in this study.

Results of actual CaCO$_3$ content for the divided four parts of soil sample (Fig. 1e) were summarized in Table 4. The weight difference between original dry sand and total weight after digestion was calculated to be less than 2%. Total mass percentage of CaCO$_3$ agreed well with the theoretical value in Table 2. Larger value in part (1) was consistent with shear wave velocity data (Fig. 5) and SEM images (Fig. 8), representing higher solid content of CaCO$_3$ precipitations near BE 1.

5.3. MONITORING EICP FROM THE VIEW OF PARTICLE SIZE AND CaCO$_3$ CONTENT

Since peak frequency related to precipitated particle size, and imaginary conductivity magnitudes at peak frequency reflected the quantity of precipitations, the dynamic EICP process of this study could be mimicked by mean particle size and quantities of carbonate precipitations. Although the size of individual carbonate particle might vary during the reaction (Wu et al. 2010), quantities of the precipitations kept increasing with the continuous catalyzing of urea. Eventually, numbers of the individual particles aggregated into relatively large particles (Choi et al. 2016; DeJong et al. 2006). Large particles would attach on the surface or contact area of Ottawa sand due to the gravity force. Therefore, the average particle size, as well as the specific surface area of CaCO$_3$ increased with the increasing of time. Increased particle size resulted in the decrement of peak frequency, and increased surface area caused the increment of

imaginary conductivity magnitude. Changing of peak frequencies, calculated particle sizes and magnitudes at peak frequencies from 1st to10^{th} PV at equilibrium were summarized in Fig. 11. A brief description was given below: (1) from 1st to 4th PV, sizes of major $CaCO_3$ aggregates were very close and the values were smaller than 0.2mm. Magnitude of imaginary conductivity increased from 0.0006 to 0.002 S/m, representing the increment of small aggregate (< 0.6mm) quantities from 0.11% to 0.44%; (2) from 4th -5th PV, magnitude decreased from 0.002 to 0.001 S/m. Size equaled to 1mm aggregate was measured in 5th PV, suggesting the formation of large sizes of aggregate from the precipitated small size of $CaCO_3$; (3) from 5th to 10th PV, large size of aggregates (> 1mm) dominated. The kept increasing magnitude of imaginary conductivity represented the continuous increment of quantities (from 0.56% to 4.30%) of these aggregates. The above changing trends of precipitated particle size and magnitude were coincided with the increasing trend of shear wave velocities (Fig. 5).

5.4. POSTULATED PARTICLE ASSOCIATION MODELS

In order to investigate the relationship between calcite precipitate characteristics (particle size and $CaCO_3$ content) and the stiffness properties (shear modulus, shear wave velocity) of geomaterials, three conceptually association models were postulated: surface coating, contact cementation and pore filling (Fig. 12). Since increasing $CaCO_3$ content could enlarge the contact area of particles by cementing on sand surfaces and V_s is positively correlated to the contact area of adjacent particles (Eq. 10), the relationship between V_s and $CaCO_3$ content is obvious. Previous studies have derived equations describing the relationship between normal modulus and cementation content (Fernandez and Santamarina 2001), bulk modulus and contact area (Briscoe and Klein 2007; Briscoe

et al. 2006) of particles. Converting normal and bulk modulus to shear modulus, the general equation relating V_s and $CaCO_3$ content could be expressed as

$$V_s = V_0 + \alpha \left[\left(1 + CaCO_3 \% \right)^\beta - 1 \right]^{\frac{1}{4}} \tag{12}$$

where V_0 (m/s), α and β are experimentally determined parameters. V_0 is the initial shear wave velocity of sand without $CaCO_3$. α relates to shear modulus of material, solid density and Poisson's ratio. β here is used to represent the possible association pattern of $CaCO_3$. Detailed derivations of α and β values for the three ideal association models are described as follows:

(1) Uniform surface coating (Fig. 12a). Fernandez and Santamarina (2001) derived the equation about the relation of tangent elastic modulus (E_T) and $CaCO_3\%$:

$$E_T = \frac{G_m}{1 - v_m} \sqrt{ \left(CaCO_3 \% + 1 \right)^{\frac{2}{3}} - 1 + \left[\left(\frac{3(1-v_m)}{2} \frac{\sigma}{G_m} \right)^{\frac{1}{3}} \right]^2 } \tag{13}$$

where G_m is shear modulus of the material, v_m is Poisson's ratio and σ is the average normal stress on contact area. The relation of tangent modulus (E_T) and shear modulus (G_0) is expressed as

$$E_T = 2G_0 \left(1 + v_m \right) \tag{14}$$

Combining Eqs. 10, 13 and 14,

$$V_s = \left\{ \frac{G_m}{2\rho \left(1 - v_m^2 \right)} \sqrt{ \left(CaCO_3 \% + 1 \right)^{\frac{2}{3}} - 1 + \left[\left(\frac{3(1-v_m)}{2} \frac{\sigma}{G_m} \right)^{\frac{1}{3}} \right]^2 } \right\}^{\frac{1}{2}} \tag{15}$$

Therefore, $\alpha = \left(\dfrac{G_m}{2\rho\left(1 - v_m^2\right)} \right)^{\frac{1}{2}}$ and $\beta = \dfrac{2}{3}$.

(2) Perfect contact cementation (Fig. 12b): previous studies had no equations directly describing the relationship between cementation content and stiffness of geomaterials for this model. However, basic ideas from Briscoe and Klein (2007) and Cao et al. (2018) could be used to derive it. Detailed procedures are given below. Two elastic spheres with equal radius R are considered as Hertz contact. The subjected normal load is P. Therefore, the radius (a) of the circular contact area can be expressed as

$$a = \sqrt[3]{\frac{3\left(1 - v_m\right)}{8G_m} PR} \tag{16}$$

For cubic packing, $P = 4\sigma R^2$, substituting into Eq. 16,

$$\frac{a}{R} = \sqrt[3]{\frac{3\left(1 - v_m\right)\sigma}{2G_m}} \tag{17}$$

Therefore, the tangent elastic modulus (E_T) is equal to

$$E_T = \frac{d\sigma}{d\varepsilon} = \frac{3}{2}\left[\frac{2}{3\left(1 - v_m\right)}\right]^{\frac{2}{3}}\left(\frac{\sigma}{G_m}\right)^{\frac{1}{3}}G_m = \frac{G_m}{1 - v_m}\sqrt[3]{\frac{3\left(1 - v_m\right)\sigma}{2G_m}} = \frac{G_m}{1 - v_m}\frac{a}{R} \tag{18}$$

where $\varepsilon = \dfrac{a^2}{R^2}$ is the strain.

To simplify the result, the density of sand and calcium carbonate are assumed equal. Thus,

$$\mathrm{CaCO_3}\% = \frac{V_{\mathrm{CaCO_3}}}{V_{sand}} = \frac{V_{cylinder} - V_{cap}}{V_{sand}} = \frac{\pi a_c^2 H - \frac{\pi H}{6}\left(3a_c^2 + H^2\right)}{\frac{1}{4}\cdot\frac{4}{3}\pi R^3}$$

$$= \frac{1}{2}\left(\sqrt{1-\left(\frac{a_0}{R}\right)^2} - \sqrt{1-\left(\frac{a_c}{R}\right)^2}\right)\left[3\left(\frac{a_c}{R}\right)^2 - \left(\sqrt{1-\left(\frac{a_0}{R}\right)^2} - \sqrt{1-\left(\frac{a_c}{R}\right)^2}\right)^2\right] \quad (19)$$

where $H = \sqrt{R^2 - a_0^2} - \sqrt{R^2 - a_c^2}$ is half of cement height.

Since $\dfrac{a_c}{R} \to 1$ with the increment of $\mathrm{CaCO_3}\%$, Eq. 19 could be simplified as

$$\mathrm{CaCO_3}\% \approx \frac{3}{2}\sqrt{1-\left(\frac{a_0}{R}\right)^2}\left[\left(\frac{a_c}{R}\right)^2 - \frac{1}{2}\left[1-\left(\frac{a_0}{R}\right)^2\right]\right]^{\frac{3}{2}} \quad (20)$$

Combining Eqs. 10, 14, 18 and 20,

$$\mathrm{CaCO_3}\% \approx \frac{3}{2}\sqrt{1-\left(\frac{3(1-v_m)\sigma}{2G_m}\right)^{\frac{2}{3}}}\left[\left(\frac{E_T(1-v_m)}{G_m}\right)^2 - \frac{1}{2}\left[1-\left(\frac{3(1-v_m)\sigma}{2G_m}\right)^{\frac{2}{3}}\right]\right]^{\frac{3}{2}}$$

$$= \frac{3}{2}\sqrt{1-\left(\frac{3(1-v_m)\sigma}{2G_m}\right)^{\frac{2}{3}}}\left[\left(\frac{2\rho V_s^2(1-v_m^2)}{G_m}\right)^2 - \frac{1}{2}\left[1-\left(\frac{3(1-v_m)\sigma}{2G_m}\right)^{\frac{2}{3}}\right]\right]^{\frac{3}{2}} \quad (21)$$

Rearranging,

$$V_s \approx \sqrt{\frac{G_m}{2\rho\left(1-v_m^2\right)}} \sqrt[4]{\frac{2}{3}\frac{1+\text{CaCO}_3\%}{\sqrt{1-\left[\frac{3\left(1-v_m\right)\sigma}{2G_m}\right]^{\frac{2}{3}}}} + \frac{1}{3}\frac{\left(\sqrt{1-\left[\frac{3\left(1-v_m\right)\sigma}{2G_m}\right]^{\frac{2}{3}}}\right)^3 - 1}{\sqrt{1-\left[\frac{3\left(1-v_m\right)\sigma}{2G_m}\right]^{\frac{2}{3}}}}}$$

$$= \left\{ \frac{G_m^2}{6\rho^2\left(1-v_m^2\right)^2\sqrt{1-\left[\frac{3\left(1-v_m\right)\sigma}{2G_m}\right]^{\frac{2}{3}}}} \left[\left(1+\text{CaCO}_3\%\right)-1\right] + \frac{G_m^2}{12\rho^2\left(1-v_m^2\right)^2} \frac{\left(\sqrt{1-\left[\frac{3\left(1-v_m\right)\sigma}{2G_m}\right]^{\frac{2}{3}}}\right)^3 + 1}{\sqrt{1-\left[\frac{3\left(1-v_m\right)\sigma}{2G_m}\right]^{\frac{2}{3}}}} \right\}^{\frac{1}{4}}$$

$$(22)$$

Therefore, $\alpha = \left(\dfrac{G_m^2}{6\rho^2\left(1-v_m^2\right)^2\sqrt{1-\left[\frac{3\left(1-v_m\right)\sigma}{2G_m}\right]^{\frac{2}{3}}}} \right)^{\frac{1}{4}}$ and $\beta = 1$.

(3) Pore filling (Fig. 12c): $\beta = 0$ if it was pore filling because of the slightly or no influences on increasing the contact area and therefore V_s.

Overall, the above theoretical values were calculated based on the uniform and ideal cementation models, and cubic packing was assumed in deriving the relation of normal load and stress for Hertz contact. Therefore, $2/3 \leq \beta < 1$ and $\beta \geq 1$ could be postulated for surface coating and contact cementation respectively, to represent the actual association patterns.

5.5. RELATION OF PRECIPITATE CHARACTERISTICS AND STIFFNESS PROPERTIES OF GEOMATERIAL

Theoretical α and β values for uniform surface coating and ideal contact cementation were summarized in Table 3. $G_m = 90$ MPa (Delfosse-Ribay et al. 2004), $\rho = 1.659 \times 10^3$ kg/m^3 and $v_m = 0.25$ for Ottawa sands were adopted to calculate α values as references. Fitted α and β values from Eq. 12 for BE 1-2 and 3-2 of this study and test values at measured point B of Martinez et al. (2013) were presented in Fig. 13 and Table 3 as well. Fitting process on Martinez et al. (2013) curve was divided into two parts at CaCO$_3$% = 5%, considering the different changing trends of V_s. Comparing the theoretical and experimental results of α and β, the following observations are made: (1) β values for BE 1-2 and 3-2 of this study were larger than theoretical ideal contact cementation value. Contact cementation was postulated as the dominant association pattern in this study; (2) β was larger than theoretical contact cementation value for Martinez et al. 2013-1 and very close to theoretical value for Martinez et al. 2013-2. Thus, contact cementation pattern was suggested for Martinez et al. 2013 MICP study. When CaCO$_3$% $\geqslant$ 5%, MICP behaved like the perfect contact cementation pattern as the model described above; (3) α values for this study and Martinez et al. 2013 were close to each other. Compared to theoretical contact cementation value, larger experimental α values could be attributed to the formation of calcium carbonate crystals and thereby the increased G_m. Results of this study consisted with SEM images shown in Fig. 8, which elucidated the contact cementation pattern with few CaCO$_3$ crystals on sand surfaces in this study. The cementation type of MICP in Martinez et al. (2013) was also reported to be contact cementation.

5.6. POSSIBLE EXPLANATIONS OF POSTULATED ASSOCIATION PATTERN IN EICP

Fig. 7 showed that at least two times increment was observed in shear wave velocities (V_s/V_0) with less than 4.5% $CaCO_3$ precipitations, no matter which remediation methods (MICP, EICP or denitrification) were used. This probably also demonstrated the precipitations of $CaCO_3$ crystals in contact areas of sand particles due to the property of this association pattern: significantly enlarged contact area and thereby the shear wave velocity. Combing the conclusions of β value drawn above and SEM images (Fig, 8), contact areas were postulated to be the most prone precipitated locations in bio-mediation. This could be elaborated by the formation of eddies (Darcy flow regime) and the nucleation of $CaCO_3$ crystals during the precipitation process. When the inflow solution was continuously introduced into the soil column (porous media), stationary eddies were formed near the pore throats based on the numerical simulation result of previous study (Chaudhary et al. 2011) if Darcy's law was assumed valid. The area of eddy was investigated and occupied about 1/5 of the pore volume (Chaudhary et al. 2011). A cartoon showing of the stationary eddy was given in Fig. 12d. Different from those bacteria/enzyme in other flow fields which had higher possibilities to be flushed out by the influent solution, bacteria (MICP and denitrification) or enzyme (EICP) distributed in eddies were much easier to settle down and attach on the sand surfaces due to the local and stationary properties of these pore throat eddies. Previous study (Ferris et al. 1987) also observed that bacteria could work as nucleation site to precipitate minerals and crystals. Therefore, most of $CaCO_3$ crystals finally started to precipitate in the eddy area, i.e. the contact areas of sand particles and upon which, as the initial formed nucleation sites, additional $CaCO_3$ precipitates deposited and accumulated as the crystals grew.

5.7. ADVANTAGE OF EICP OBSERVED IN THIS STUDY

Both test results and SEM images (Fig. 7) of this study suggested that most of urease enzymes pre-mixed with sands was not flushed out by the injected influent solution. After being evenly pre-mixed, it could significantly improve the heterogeneous problem that was often encountered in bio-treatment and largely increase the efficiency, no matter for laboratory or field applications.

6. CONCLUSION

Enzyme induced calcite precipitation (EICP) test was conducted in this study on Ottawa 50-70 sand by introducing the urea and calcium chloride solutions into evenly pre-mixed sand with urease enzyme soil sample. Non-destructive spectral induced polarization (SIP) technique was used to monitor the precipitation process during the catalytic reaction. Bender element was selected to detect the shear wave velocities of the enhanced soil. A SIP-BE column was developed in order to measure SIP and shear wave velocity simultaneously. And three conceptual association models were postulated to elucidate the relationship between precipitation characteristics and the stiffness properties of geomaterials. The following conclusions can be made:

(1) Real conductivity trends from SIP can reflect the catalytic reaction of calcite precipitation during EICP. Similar trends of outflow DC conductivity and real conductivity suggests that electrolytic DC conductivity is the major component of real conductivity in this study.

(2) The evolution of imaginary conductivity reveals information about characteristics (particle size and solid content) of precipitations. Mean particle sizes are

calculated from peak frequencies and Schwarz equation; solid content obtains from the normalized chargeability parameter in Cole-Cole model of complex conductivity.

(3) Three conceptual association models are postulated: surface coating, contact cementation and pore filling. β parameters, representing the possible association patterns, are 2/3, 1 and 0 for uniform surface coating, perfect contact cementation and pore filling respectively.

(4) $CaCO_3$ crystals are more prone to precipitate and accumulate near the contact areas of sand particles in bio-mediation. Contact cementation is observed to be dominant association pattern in this study.

(5) In Darcy flow, stationary eddies forming near the pore throats among sand particles seem to be the reason that larger possibilities of $CaCO_3$ precipitates attach near the contact areas of sand particles. Those eddies can also behave as the nucleation sites for the accumulation of additional $CaCO_3$ crystals.

Figure 1. (a) Experimental setup of SIP/BE testing system; (b) side view of SIP/BE unit; (c) a bender element unit; (d) enlarged schematic setup of bender element with O-rings; and (e) equally divided four parts of sample for $CaCO_3$ content determination.
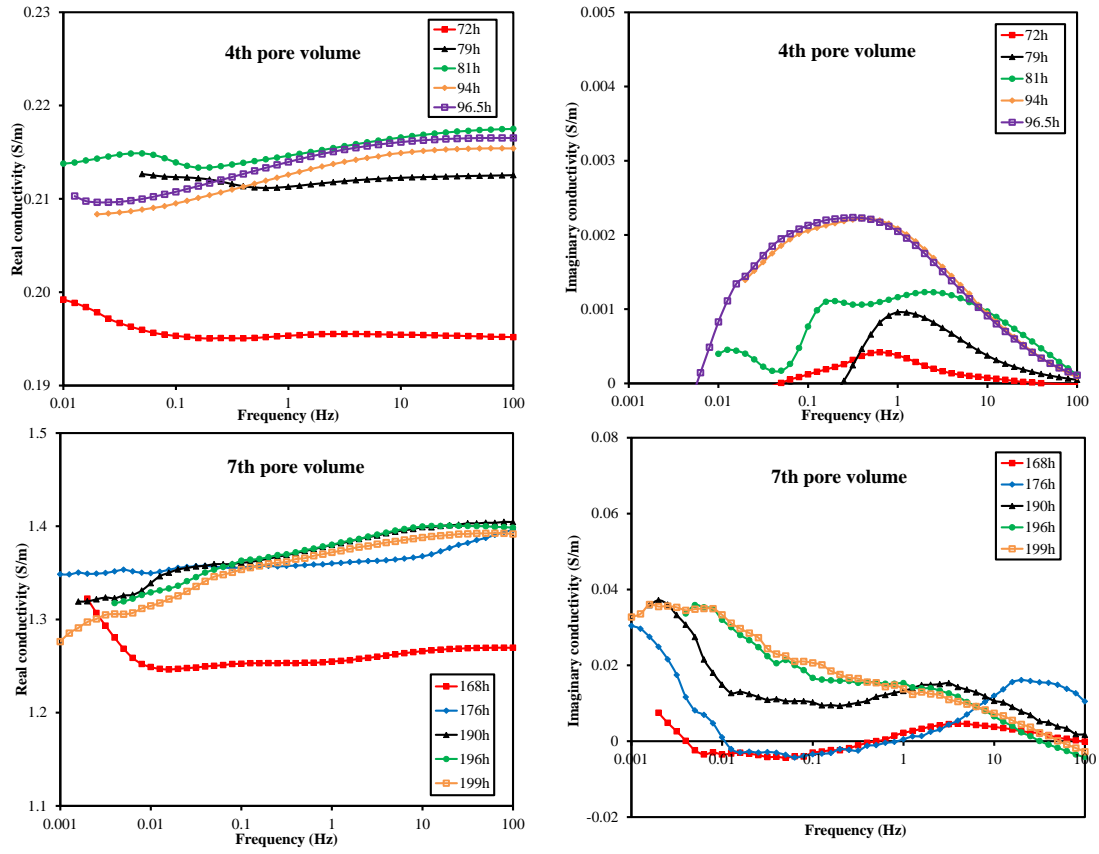
Figure 2. Real and imaginary conductivities at 4th and 7th pore volumes (time was continuous from the 1st pore volume).
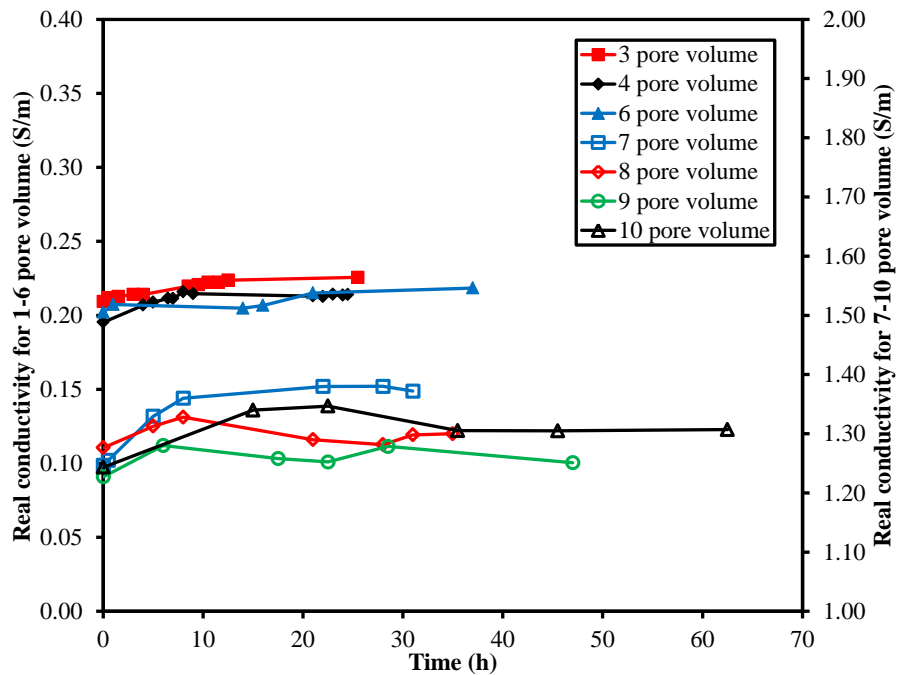
Figure 3. Changing of real conductivity with time for each pore volume.
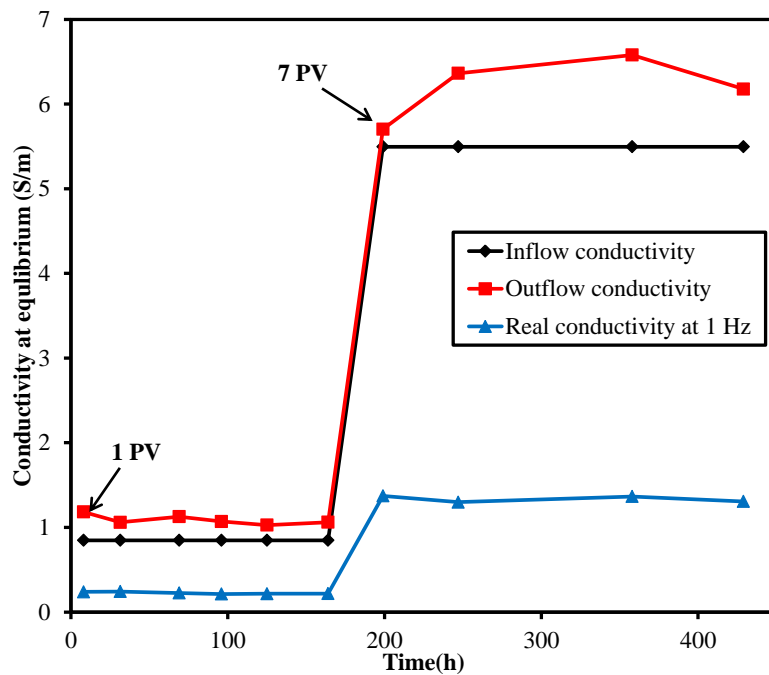
Figure 4. Inflow, outflow and real (1Hz) conductivities at equilibrium state for each PV.
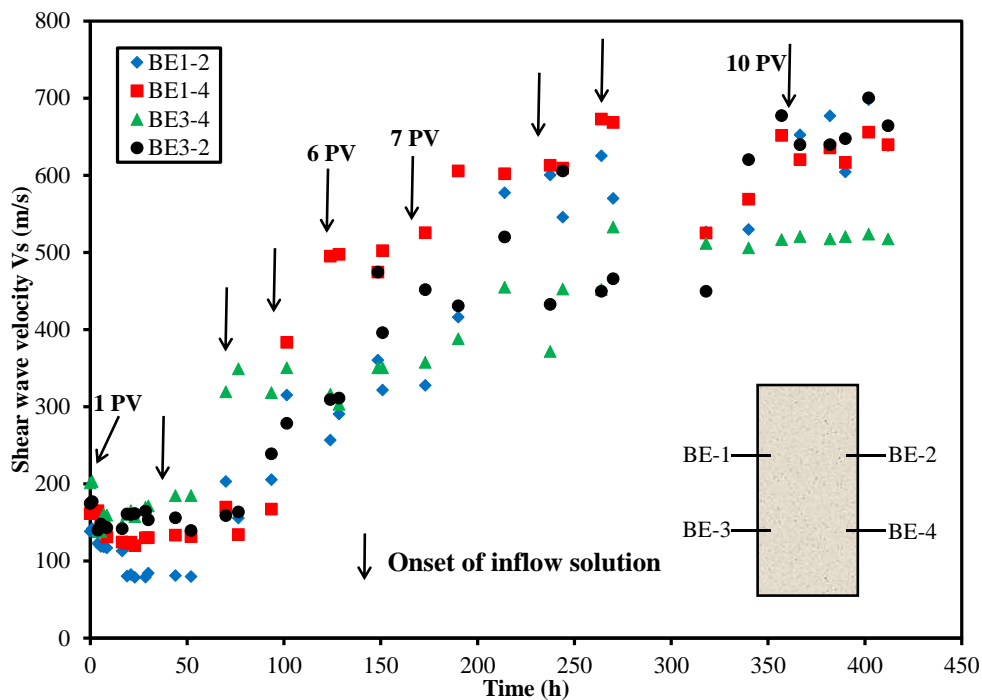
Figure 5. Shear wave velocity as a function of reaction time for the four pairs of bender element.
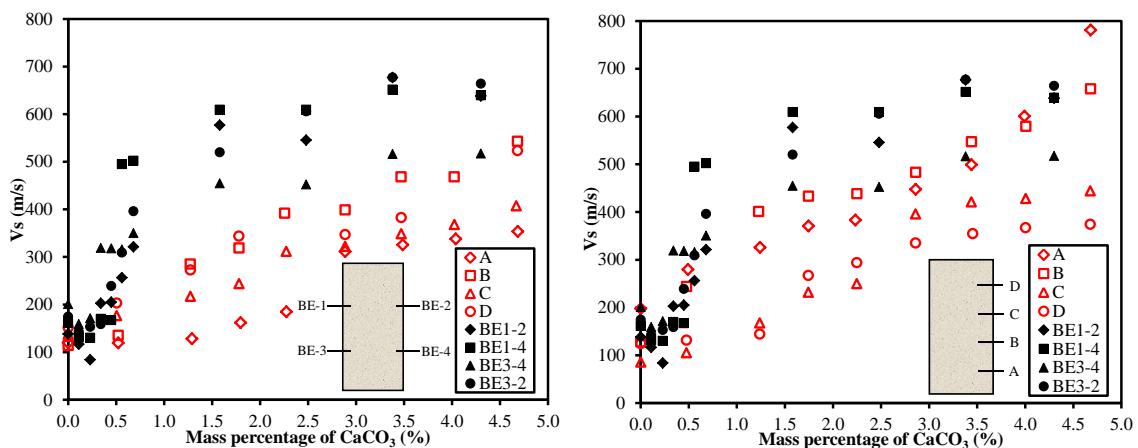
Figure 6. Shear wave velocities changing with mass percentage of calcium carbonate (this study: black solid symbols; Martinez et al. 2013: red open symbols, a. stopped-flow and b. continuous flow).
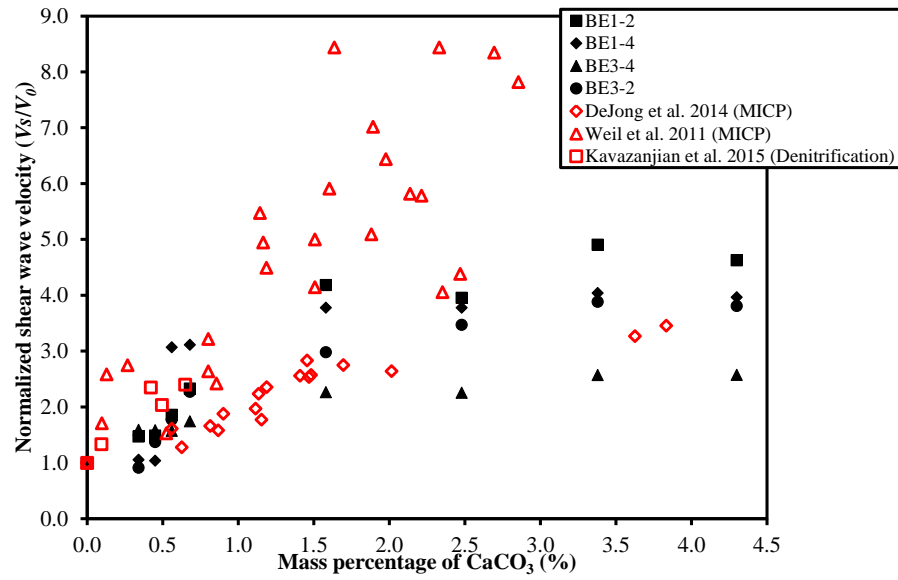
Figure 7. Normalized shear wave velocities of this and previous studies.
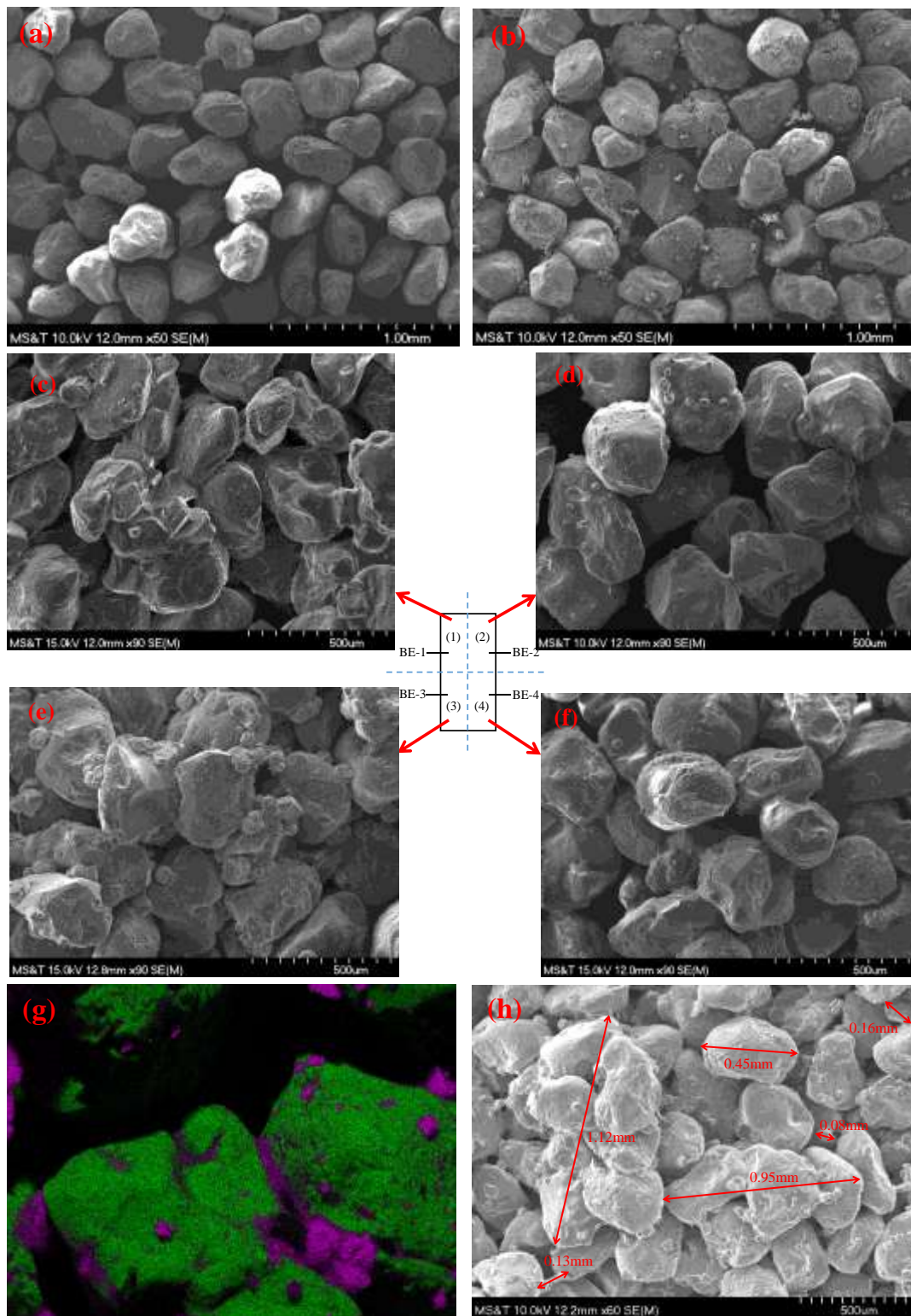
Figure 8. SEM and EDS images of CaCO$_3$ on Ottawa sand. (a) Pure sand, (b) sand and urea enzyme mixture, (c)-(f) cemented sands near BE 1, 2, 3 and 4 respectively, (g) EDS image: Si-green color and Ca-purple color, (h) example of cemented aggregate sizes.
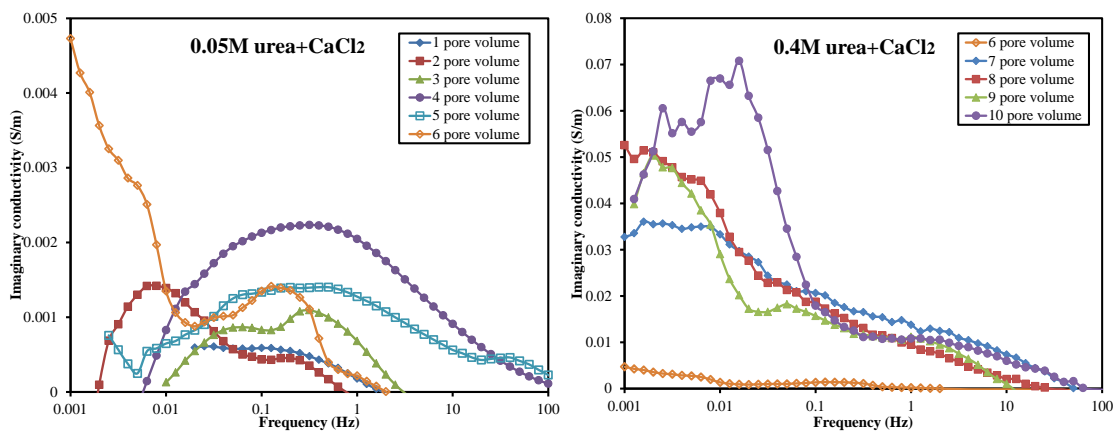
Figure 9. Imaginary conductivities at equilibrium versus frequency curves for each pore volume.
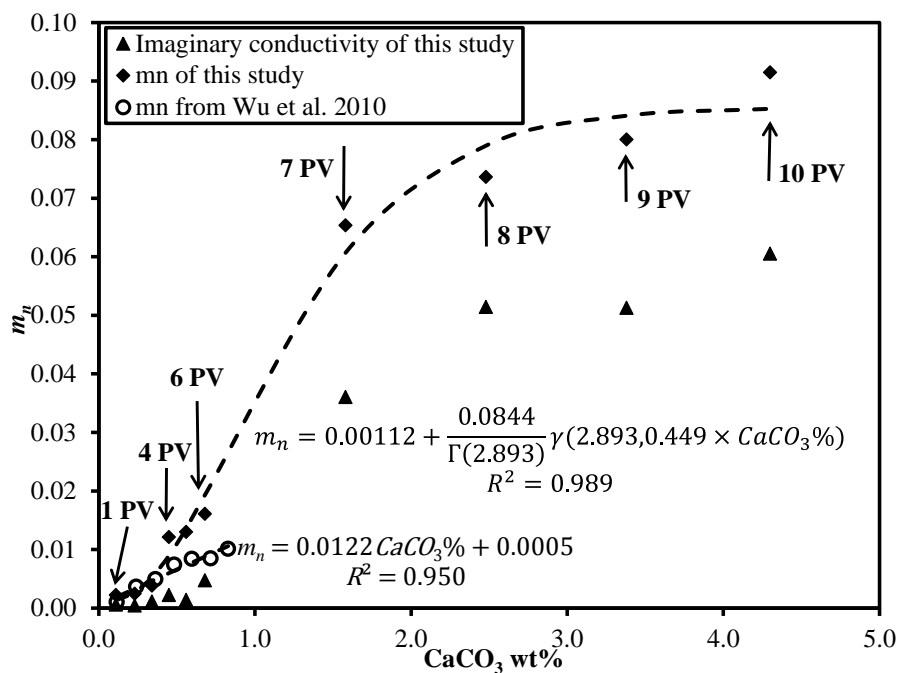
Figure 10. Relationship between m_n and $CaCO_3$ content.
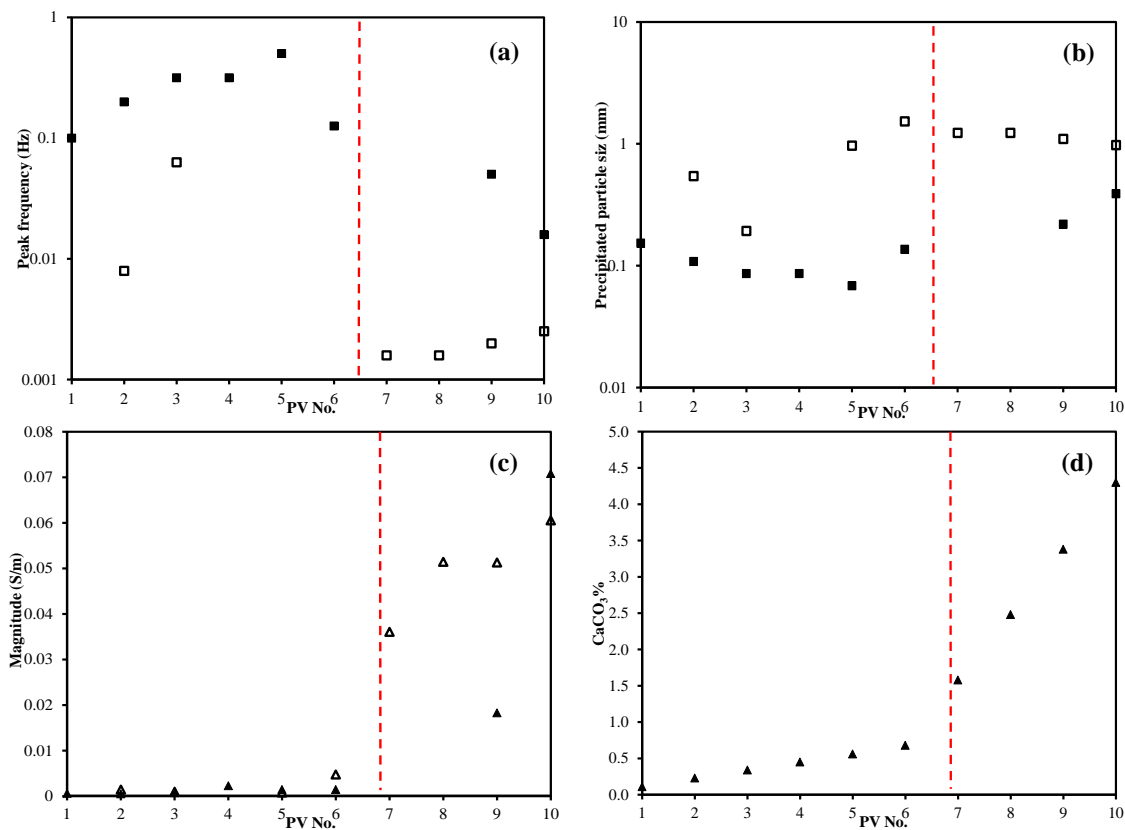
Figure 11. Changing of peak frequency, calculated CaCO$_3$ particle size and magnitude at peak frequencies at equilibrium.

(a)
Surface coating

(b)
Contact cementation

(c)
Pore filling

(d)
Eddy
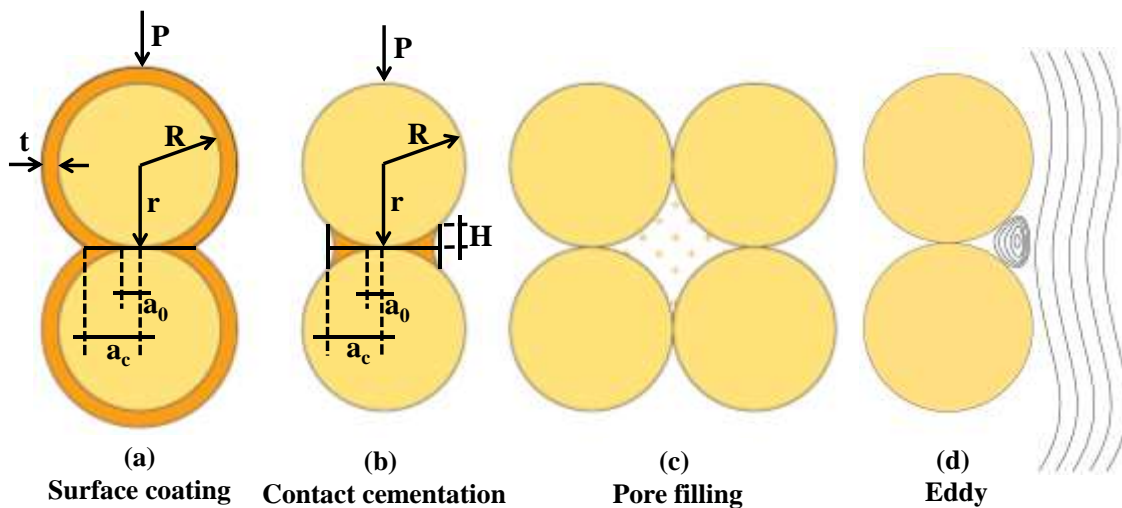
Figure 12. Cartoon showing the possible association pattern of calcite precipitates. Lines in (d) are streamlines.
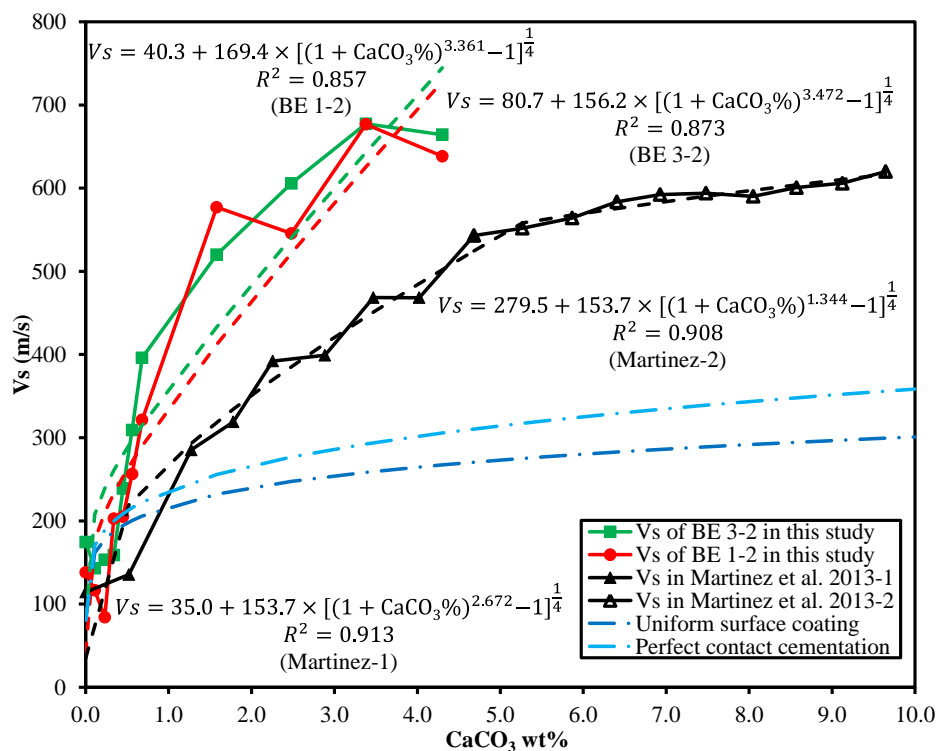
Figure 13. Fitted curves of shear wave velocities for BE 1-2, 3-2 in this study and MICP in Martinez et al. 2013.

Table 1. Theoretical particle size of $CaCO_3$ from SIP test and Eq.8.

PV	Major peak frequencies (Hz)		Calculated particle size (mm)	
1	0.100	-	0.153	-
2	0.200	0.008	0.108	0.543
3	0.316	0.063	0.086	0.193
4	0.316	-	0.086	-
5	0.501	< 0.003	0.068	> 0.965
6	0.126	< 0.001	0.136	> 1.530
7	-	0.002	-	1.230
8	-	0.002	-	1.230
9	0.050	0.002	0.219	1.096
10	0.016	0.003	0.389	0.977

Table 2. Theoretical (from nutrient inflow) and calculated (from DC conductivity of outflow) mass percentage of $CaCO_3$.

No. of pore volume	Theoretical mass%	Calculated mass%
1	0.11	0.11
2	0.23	0.23
3	0.34	0.34
4	0.45	0.45
5	0.56	0.55
6	0.68	0.66
7	1.58	1.24
8	2.48	1.88
9	3.38	2.55
10	4.3	3.17

Table 3. Theoretical and experimental α and β values.

	α	β
Uniform surface coating	170.1	2/3
Ideal contact cementation	153.7	1
BE 1-2 of this study	169.4	3.361
BE 3-2 of this study	156.2	3.472
Martinez et al. 2013-1	153.7	2.672
Martinez et al. 2013-2	153.7	1.344

Table 4. Total $CaCO_3$ generated in actual.

	Mass of dry sand (g)	Mass of $CaCO_3$ (g)	Mass percentage of $CaCO_3$ (%)
1	423.86	25.67	6.06
2	542.63	16.16	2.98
3	474.83	21.21	4.47
4	470.32	19.11	4.06
Total	1911.64	82.15	4.30

REFERENCES

Abdel, A. G. Z., Atekwana, E. A., Slater, L. D., and Atekwana, E. A. (2004). "Effects of microbial processes on electrolytic and interfacial electrical properties of unconsolidated sediments." *Geophysical Research Letters*, 31(12).

Archie, G. E. (1942). "The Electrical Resistivity Log as an Aid in Determining Some Reservoir Characteristics." *Transactions of the AIME*, 146(01), 54-62.

Atekwana, E. A., and Slater, L. D. (2009). "Biogeophysics: A new frontier in Earth science research." *Reviews of Geophysics*, 47(4).

Bate, B., and Zhang, L. M. (2013). "Use of Vacuum for the Stabilization of Dry Sand Slopes." *Journal of Geotechnical and Geoenvironmental Engineering*, 139(1), 143-151.

Börner, F. D., Schopper, J. R., and Weller, A. (1996). "Evaluation of transport and storage properties in the soil and groundwater zone from induced polarization measurements." *Geophysical Prospecting*, 44(4), 583-601.

Breede, K., Kemna, A., Esser, O., Zimmermann, E., Vereecken, H., and Huisman, J. A. (2011). "Joint Measurement Setup for Determining Spectral Induced Polarization and Soil Hydraulic Properties." *Vadose Zone Journal*, 10(2), 716-726.

Briscoe, W. H., and Klein, J. (2007). "Friction and Adhesion Hysteresis between Surfactant Monolayers in Water." *The Journal of Adhesion*, 83(7), 705-722.

Cao, J., Jung, J., Song, X., and Bate, B. (2018). "On the soil water characteristic curves of poorly graded granular materials in aqueous polymer solutions." *Acta Geotechnica*, 13(1), 103-116.

Chaudhary, K., Cardenas, M. B., Deng, W., and Bennett, P. C. (2011). "The role of eddies inside pores in the transition from Darcy to Forchheimer flows." *Geophysical Research Letters*, 38(24).

Choi, S.-G., Wu, S., and Chu, J. (2016). "Biocementation for Sand Using an Eggshell as Calcium Source." *Journal of Geotechnical and Geoenvironmental Engineering*, 142(10), 06016010.

Cole, K. S., and Cole, R. H. (1941). "Dispersion and Absorption in Dielectrics I. Alternating Current Characteristics." *The Journal of Chemical Physics*, 9(4), 341-351.

DeJong, J., Martinez, B., Ginn, T., Hunt, C., Major, D., and Tanyu, B. (2014). "Development of a Scaled Repeated Five-Spot Treatment Model for Examining Microbial Induced Calcite Precipitation Feasibility in Field Applications." *Geotechnical Testing Journal*, 37, 424-435.

DeJong, J. T., Fritzges, M. B., and Nüsslein, K. (2006). "Microbially Induced Cementation to Control Sand Response to Undrained Shear." *Journal of Geotechnical and Geoenvironmental Engineering*, 132(11), 1381-1392.

Delfosse-Ribay, E., Djeran-Maigre, I., Cabrillac, R., and Gouvenot, D. (2004). "Shear modulus and damping ratio of grouted sand." *Soil Dynamics and Earthquake Engineering*, 24(6), 461-471.

Fernandez, A. L., and Santamarina, J. (2001). *Effect of cementation on the small-strain parameters of sand*.

Ferris, F. G., Fyfe, W. S., and Beveridge, T. J. (1987). "Bacteria as nucleation sites for authigenic minerals in a metal-contaminated lake sediment." *Chemical Geology*, 63(3), 225-232.

Hall, J. R., Wishaw, B. F., and Stokes, R. H. (1953). "The Diffusion Coefficients of Calcium Chloride and Ammonium Chloride in Concentrated Aqueous Solutions at 25°." *Journal of the American Chemical Society*, 75(7), 1556-1560.

Hamdan, N., and Kavazanjian, E. (2016). "Enzyme-induced carbonate mineral precipitation for fugitive dust control." *Géotechnique*, 66(7), 546-555.

Islam, M., Chittoori, C. S. B., and Burbank, M. (2018). "Role of Clay Content in Microbial Precipitation of Calcium Carbonate in Swelling Soils." *Transportation Research Board (TRB) Annual Meeting*.

Jiang, N.-J., Soga, K., and Kuo, M. (2017). "Microbially Induced Carbonate Precipitation for Seepage-Induced Internal Erosion Control in Sand–Clay Mixtures." *Journal of Geotechnical and Geoenvironmental Engineering*, 143(3), 04016100.

Kang, X., and Bate, B. (2016). "Shear Wave Velocity and Its Anisotropy of Polymer Modified High-Volume Class-F Fly Ash–Kaolinite Mixtures." *Journal of Geotechnical and Geoenvironmental Engineering*, 142(12), 04016068.

Kang, X., Kang, G., and Bate, B. (2014). "Measurement of Stiffness Anisotropy in Kaolinite Using Bender Element Tests in A Floating Wall Consolidometer." *Geotechnical Testing Journal*, 37, 869-883.

Kavazanjian, E., and Hamdan, N. (2015). "Enzyme Induced Carbonate Precipitation (EICP) Columns for Ground Improvement." *IFCEE 2015*, 2252-2261.

Kavazanjian, E., O'Donnell, S., and Hamdan, N. (2015). "Biogeotechnical mitigation of earthquake-induced soil liquefaction by denitrification: a two-stage process." *6th international conference on earthquake Geotechnical Engineering*Christchurch, New Zealand.

Knight, R. J., and Nur, A. (1987). "Geometrical Effects In The Dielectric Response Of Partially Saturated Sandstones." *Log Analyst*, 28(6), 513-519.

Kruschwitz, S., Binley, A., Lesmes, D., and Elshenawy, A. (2010). "Textural controls on low-frequency electrical spectra of porous media." *GEOPHYSICS*, 75(4), WA113-WA123.

Kruschwitz, S., Prinz, C., and Zimathies, A. (2016). "Study into the correlation of dominant pore throat size and SIP relaxation frequency." *Journal of Applied Geophysics*, 135, 375-386.

Lee, J.-S., and Santamarina, J. C. (2005). "Bender Elements: Performance and Signal Interpretation." *Journal of Geotechnical and Geoenvironmental Engineering*, 131(9), 1063-1070.

Lesmes, D. P., and Frye, K. M. (2001). "Influence of pore fluid chemistry on the complex conductivity and induced polarization responses of Berea sandstone." *Journal of Geophysical Research: Solid Earth*, 106(B3), 4079-4090.

Lin, H., Suleiman, M. T., Brown, D. G., and Kavazanjian, E. (2016). "Mechanical Behavior of Sands Treated by Microbially Induced Carbonate Precipitation." *Journal of Geotechnical and Geoenvironmental Engineering*, 142(2), 04015066.

Maleki, M., Ebrahimi, S., Asadzadeh, F., and Emami Tabrizi, M. (2016). "Performance of microbial-induced carbonate precipitation on wind erosion control of sandy soil." *International Journal of Environmental Science and Technology*, 13(3), 937-944.

Martinez, B., and DeJong, J. (2009). "Bio-Mediated Soil Improvement: Load Transfer Mechanisms at the Micro- and Macro- Scales." *Advances in Ground Improvement*, 2009 US-China workshop on ground improvement technologies, 242-251.

Martinez, B. C., DeJong, J. T., Ginn, T. R., Montoya, B. M., Barkouki, T. H., Hunt, C., Tanyu, B., and Major, D. (2013). "Experimental Optimization of Microbial-Induced Carbonate Precipitation for Soil Improvement." *Journal of Geotechnical and Geoenvironmental Engineering*, 139(4), 587-598.

Montoya, B. M., DeJong, J. T., Boulanger, R. W., Wilson, D. W., Gerhard, R., Ganchenko, A., and Chou, J.-C. (2012). "Liquefaction Mitigation Using Microbial Induced Calcite Precipitation." *GeoCongress 2012*, 1918-1927.

Pelton, W. H., Ward, S. H., Hallof, P. G., Sill, W. R., and Nelson, P. H. (1978). "MINERAL DISCRIMINATION AND REMOVAL OF INDUCTIVE COUPLING WITH MULTIFREQUENCY IP." *GEOPHYSICS*, 43(3), 588-609.

Revil, A. (2012). "Spectral induced polarization of shaly sands: Influence of the electrical double layer." *Water Resources Research*, 48(2).

Revil, A., Koch, K., and Holliger, K. (2012). "Is it the grain size or the characteristic pore size that controls the induced polarization relaxation time of clean sands and sandstones?" *Water Resources Research*, 48(5).

Salifu, E., MacLachlan, E., Iyer, K. R., Knapp, C. W., and Tarantino, A. (2016). "Application of microbially induced calcite precipitation in erosion mitigation and stabilisation of sandy soil foreshore slopes: A preliminary investigation." *Engineering Geology*, 201, 96-105.

Schwarz, G. (1962). "A THEORY OF THE LOW-FREQUENCY DIELECTRIC DISPERSION OF COLLOIDAL PARTICLES IN ELECTROLYTE SOLUTION1,2." *The Journal of Physical Chemistry*, 66(12), 2636-2642.

Scott, J. B. T., and Barker, R. D. (2003). "Determining pore‐throat size in Permo‐Triassic sandstones from low‐frequency electrical spectroscopy." *Geophysical Research Letters*, 30(9).

Slater, L., and Lesmes, D. P. (2002). "Electrical‑hydraulic relationships observed for unconsolidated sediments." *Water Resources Research*, 38(10), 31-31-31-13.

van Paassen, L. A. (2011). "Bio-Mediated Ground Improvement: From Laboratory Experiment to Pilot Applications." *Geo-Frontiers 2011*.

Vinegar, H. J., and Waxman, M. H. (1984). "Induced polarization of shaly sands." *GEOPHYSICS*, 49(8), 1267-1287.

Waxman, M. H., and Smits, L. J. M. (1968). "Electrical Conductivities in Oil-Bearing Shaly Sands." *Transactions of the American Institute of Mining and Metallurgical Engineers*, 243, 107-122.

Weil, M., DeJong, J., Martinez, B., and Mortensen, B. (2012). "Seismic and Resistivity Measurements for Real-Time Monitoring of Microbially Induced Calcite Precipitation in Sand." *Geotechnical Testing Journal*, 35(2), 330-341.

Whiffin, V. S., van Paassen, L. A., and Harkes, M. P. (2007). "Microbial Carbonate Precipitation as a Soil Improvement Technique." *Geomicrobiology Journal*, 24(5), 417-423.

Wu, Y., Hubbard, S., Williams, K. H., and Ajo‑Franklin, J. (2010). "On the complex conductivity signatures of calcite precipitation." *Journal of Geophysical Research: Biogeosciences*, 115(G2).

Wu, Y., Slater, L. D., and Korte, N. (2005). "Effect of Precipitation on Low Frequency Electrical Properties of Zerovalent Iron Columns." *Environmental Science & Technology*, 39(23), 9197-9204.

Zhang, C., Slater, L., Redden, G., Fujita, Y., Johnson, T., and Fox, D. (2012). "Spectral Induced Polarization Signatures of Hydroxide Adsorption and Mineral Precipitation in Porous Media." *Environmental Science & Technology*, 46(8), 4357-4364.

Zhu, J., Cao, J. N., Bate, B., and Khayat, K. (2018). "Determination of mortar setting times using shear wave velocity evolution curves measured by the bender element technique." *Cement and Concrete Research*, 106, 1-11.

II. COMPLEX CONDUCTIVITY AND SHEAR WAVE VELOCITY RESPONSES OF SAND-CALCITE MIXTURE

Junnan Cao[a], Chi Zhang[b], and Bate Bate[c*]

[a] Phd student, Department of Civil, Architectural and Environmental Engineering, Missouri University of Science and Technology, Rolla, MO, USA, jcg83@mst.edu

[b] Assistant Professor, College of Liberal Arts and Sciences – Geology, University of Kansas, chizhang@ku.edu

[c] "100-Talents Program" Professor, Institute of Geotechnical Engineering, College of Civil Engineering and Architecture, Zhejiang University, 866 Yuhangtang Road, Hangzhou, China, batebate@zju.edu.cn, corresponding author

ABSTRACT

Size and distribution of precipitated particles significantly influence the efficiency of ground improvement by introducing fine particles in the original soil matrix mechanically, chemically, or biologically. However, direct measurement of these fine particles poses challenges to the existing non-destructive methods. Recent advancement in low-frequency (0.01 – 100 Hz) complex conductivity showed promising results in obtaining the size and accumulation pattern of fine particles distributed in coarse-grained soils. In this study, low-frequency complex conductivity measurements were conducted to monitor the spectral induced polarization (SIP) responses of Ottawa 50-70 sand mixed with eggshell powder at sieve size between No. 80 and 140. Vertical stresses of 5, 25, 50 and 100 kPa were progressively added to the sample. Shear wave velocity (V_s) was also monitored by bender element technique. Relaxation frequency of imaginary conductivity increased with the increment of vertical stress, which was attributed to crack generation

of eggshell as vertical stress increased. The calculated particle size at 5 kPa from complex conductivity measurement was close to the size of eggshell powder used, suggesting the accuracy of the prediction of SIP method. Shear wave velocity detected increment of stiffness of the mixture as stress increased.

1. INTRODUCTION

Spectral induced polarization (SIP) is a noninvasive geophysical method to investigate the conduction and polarization mechanisms of porous media, with applications of monitoring the process of calcite precipitation (Wu et al., 2011), iron corrosion (Wu et al., 2005), and biofilm formation and mineral precipitation in porous media (Zhang et al. 2012). The imaginary conductivity of SIP can be used as a proxy of the size and the distribution of precipitated particles. Both have major influences over the mechanical properties of geo-materials. In addition, the distribution pattern of the precipitated particles, i.e., suspended in pore fluid (pore-filling) or coated on large grain surfaces (whether or not at grain-contacting points) also play a significant role. SIP, as a promising tool to detect both size and distribution, could yield valuable information of the engineering properties. Successful application of SIP could provide valuable tool for in-situ monitoring of heterogeneous and multiphase evolution processes, such as microbial induced calcite precipitation (MICP) and ground improvement by lime treatment. Bender element, as another non-destructive method, is widely used to measure

the shear wave velocity, which is related to the initial tangent shear modulus. Shear wave velocity could vary significantly with different precipitated particle sizes and distribution patterns, especially in MICP (Weil et al., 2012).

Since both SIP and shear wave velocity are related to the particle size and distribution, the relationship between complex conductivity and shear wave velocity can be investigated. In this study, the low-frequency complex conductivity is applied to monitor the induced polarization responses of Ottawa 50-70 sand-eggshell (100%) mixture. Particle sizes are estimated from imaginary conductivity. And shear wave velocities are detected from bender element at different vertical stresses. The influence of calcite particles on both complex conductivity and shear wave velocity are elucidated.

2. BACKGROUND

2.2. SPECTRAL INDUCED POLARIZATION (SIP)

Low-frequency (typically less than 1 kHz) complex conductivity (σ^*), which is measured through two current electrodes (to generate sinusoid, positioned at both ends of the sample) and two potential electrodes (to receive responding sinusoid, located between the current electrodes), can be generally expressed as

$$\sigma^*(\omega) = \sigma'(\omega) + i\,\sigma''(\omega) \tag{1}$$

where ω is the angular frequency, σ' is the real conductivity, representing the conduction (energy loss) component, and σ'' is the imaginary conductivity, representing the polarization (energy storage) part, $i = \sqrt{-1}$.

For saturated porous media at low frequencies (< 1000 Hz), σ^* can be written as

$$\sigma^* = \sigma_{el} + \sigma^*_{surf}(\omega) = \sigma_{el} + \sigma'_{surf}(\omega) + i\,\sigma''_{surf}(\omega) \tag{2}$$

where σ_{el} is the frequency independent electrolytic conductivity of the interconnected pore space, $\sigma'_{surf}(\omega)$ and $\sigma''_{surf}(\omega)$ are frequency dependent real and imaginary components of the complex surface conductivity σ^*_{surf}, respectively.

Cole-Cole model (Cole and Cole, 1941; Pelton et al., 1978; Wu et al., 2010), as one of the most popular phenomenological models, is typically used in soil to describe the complex conductivity. The mean relaxation time τ (= $2\pi f_{peak}$, f_{peak} is the peak frequency obtained from imaginary conductivity vs. frequency curves) in the model is related to the particle diameter d. The relationship is defined by Schwarz (1962):

$$\tau = \frac{d^2}{8D_s} \tag{3}$$

where D_s is the diffusion coefficient (m^2/s).

2.2. BENDER ELEMENT TESTING SYSTEM

Bender element (BE) is a non-destructive testing (NDT) method typically used in geotechnical engineering to evaluate the shear wave velocity (V_s) of a geomaterial, which is related to the initial tangent shear modulus (G_0) by:

$$G_0 = \rho V_s^2 \tag{4}$$

The BE testing system consisted of five pairs of bender elements, signal generation and data acquisition systems: a function waveform generator (33210A,

Agilent), a filter conditioner (3364, Krohn-Hite), a linear amplifier and an oscilloscope (54622A, Agilent) (Fig. 1).

The method of BE construction is similar to that in Kang et al. (2014). A brief description was given below. The piezoceramic BE plate (Piezo Systems, Inc.) was cut into the dimensions of 12.7mm $\times$ 8.0 mm $\times$ 0.6mm (length $\times$ width $\times$ thickness) before directly connected to a coaxial cable, coated at least three layers of polyurethane as the electrical isolator and waterproofing, and fixed in a nylon spacer (inner diameter $\times$ height = 12.7 mm $\times$ 15.88 mm) by epoxy (Fig. 1a). The parallel type connection was adopted to minimize the electromagnetic coupling (Lee and Santamarina, 2005). The tip of BE was extruded to the top of nylon spacer (inner diameter $\times$ height = 0.95 cm $\times$ 2.22 cm) 5 mm (Fig. 1a). The extruded portion was coated with epoxy for protection and covered with plastic wrap to minimize crosstalk (Zhu et al. 2018).

The tip-to-tip distance (L, m) was selected as the travel distance between sender and receiver BEs. The first arrival time (t_c, s) was determined using the zero-crossing point with the x-axis of the half peak before the first major peak. Therefore, the shear wave velocity (m/s) is

$$V_s = \frac{L}{t_c} \tag{5}$$

3. MATERIALS AND EXPERIMENTAL METHODS

Ottawa 50-70 silica sand (U.S. Silica Holdings Inc., Chicago, IL) and eggshell powder (extracted from fresh eggs from a grocery store) were used in this study. D_{50} of

Ottawa sand is 0.26 mm and $e_{max} = 0.87$, $e_{min} = 0.55$. The total organic carbon (TOC) of eggshell powder is 2.77% (Shimadzu, SSM-5000A).

Both Ottawa 50-70 sand and eggshell were firstly washed with deionized water three times, and then oven-dried (100 °C) for at least 24 hours. Before packing, the inner surface of SIP/BE column was flashed three times with deionized water and 70% alcohol, respectively. Eggshell were grounded into powders using a coffee grinder (Hamilton Beach, model #: 80335) after removing the inner membranes. The particle size of sieved eggshell powder is between 0.18 mm – 0.106 mm. The inner diameter of sample cylinder (Fig. 1) was 10 cm and the total length was 30 cm. Mixture of 1575.4 g sand and 522.1 g eggshell powder was compacted into cylinder. The initial void ratio of pure sand was 1.094. The final height of the mixed sample was 15.85 cm, yielding a void ratio (e) of 0.582 and porosity (n) of 36.8%. After packing the porous media, a solution of 2.5 mM CaCl$_2$ (ACROS ORGANICS, CAS: 10043-52-4) (conductivity = 548 μS/cm) were flushed into the sample from the bottom of the column through a peristaltic pump. The flow rate was kept at 10 ml/min by the pump. After the soil was fully saturated, the fluid flow was stopped and four vertical loads (5, 25, 50 and 100 kPa) were progressively added on the top of the sample via the load frame (Master loader HM-3000, Humboldt MFG. CO., Norridge, IL). Meanwhile, settlements of the sample under each vertical load were measured by a dial gauge (Humboldt MFG. CO., accuracy = 0.0001 inch). It was found that void ratio slightly decreased from 0.582 to 0.579 as vertical stress increased from 5 to 100 kPa.

4. RESULTS AND DISCUSSION

The changing of real and imaginary conductivities with frequencies at 5, 25, 50 and 100 kPa vertical stresses were shown in Fig. 2. It can be observed that (1) real conductivity (σ') varies from 8.4 to 9.8 mS/m in the frequency range of 0.05-100 Hz under all vertical stresses; (2) imaginary conductivity curves of 25 and 50 kPa were similar with each other; (3) two peak frequencies were detected on 25 and 50 kPa curves. They were around 1 and 0.1 Hz, respectively; ; (4) One peak frequency was observed on both 5 ($\approx$ 0.1 Hz) and 100 kPa ($\approx$ 2.5 Hz) curves over the tested frequency range from 0.01 to 100 Hz; (5)Major peak frequency increased with the increment of vertical stress.

Ribeiro et al. (2008) found that the diffusion coefficient (D_s) of CaCl$_2$ solution (0.005-0.1 mol/l) was 1.335×10^{-9} m^2/s at 25 ℃. Their experimental results showed that diffusion coefficient decreased with the increment of CaCl$_2$ concentration. Therefore, substituting $D_s = 1.335 \times 10^{-9}$ m^2/s into Eq. 3, the particle diameters at different vertical stresses for this study could be calculated (Table 1). The obtained value at peak frequency $\approx$ 0.1 Hz was similar to the size of the individual eggshell particle. Major peak frequency increased with the increment of vertical stress. This might due to the crushing of eggshells caused by the stress concentration at particle contacts under vertical loads. More cracks and smaller particle sizes would occur with the increment of vertical stress, which caused the major peak frequency shifting to the right direction (Fig. 2b).Particle size $\geq$ 0.412 mm was detected at 100 kPa (Table 1). This might due to the attachment of eggshell powder on the surface of Ottawa sand (electrostatic attraction) forming relatively larger particles. This conclusion could be substantiated by the increased BE results shown in Fig. 3 (see discussion later).

Outflow fluid conductivities (σ_f) increased from 728.3 to 820.7 µS/cm at day 1 to day 5 and decreased to 798.9 µS/cm at day 7. This had the similar trend with real conductivity (Fig. 2a). The slight increment of σ_f was postulated to be the leaching of the dissolved ions remaining in the eggshell, which is often nutrient-enriched. According to Archie's law (1942), real conductivity (σ') was affected by the fluid conductivity and porosity. But the test results showed that the fluid conductivity was the major influential factor of the real conductivity in this study. In addition, surface conductance played a secondary role in influencing the real conductivity due to the small specific area of Ottawa 50-70 sand and eggshell powder, which located in the range of fine sand.

Fig. 3 presented the values of shear wave velocity at different vertical stresses. V_s increased with the increment of vertical stress. The maximum V_s value was 189.2 m/s. The slope of V_s increment between 50-100 kPa is the largest compared to those at 5-25 kPa and 25-50 kPa.

Robertson et al. (1995) measured the shear wave velocity of in-situ Ottawa sand (C109) (e_{min} = 0.500, e_{max} = 0.820, D_{50} = 0.35 mm) when it consolidated from loose condition to the void ratio locating at the critical state line, K_0 = 0.4. The results at 5, 25, 50 and 100 kPa were selected and also plotted in Fig. 3. Santamarina and Cho (2001) reported that the critical state effective friction angle φ' of Ottawa sand was 34°. Based on the Jaky's equation, K_0 = 1- sin φ', the calculated K_0 value of this study was 0.44, which was similar with the value of Robertson et al. (1995). It can be observed from Fig. 3 that the slope of V_s increment between adjacent vertical loads increased more mildly compared to those of this study. In addition, comparing the V_s values of the two curves, shear wave velocities of this study were larger than those of Robertson et al. at four

vertical stresses. These could probably be attributed to the effects of calcite from eggshell powders used in this study.

5. SUMMARY

Low-frequency complex conductivity was applied to monitor the induced polarization responses of a mixture of Ottawa 50-70 sand and eggshell powder (sieve size 80-140). Vertical stresses were added progressively on top of the soil sample following the sequence of 5, 25, 50 and 100 kPa. Particle sizes were calculated from the results of imaginary conductivities. Shear wave velocity was monitored by bender element technique. The following observations are made:

(1) Real conductivity was primarily influenced by the fluid conductivity;

(2) Estimated particle size from imaginary conductivity at 5 kPa was similar to the size of eggshell powder used in this study;

(3) Peak frequency changing with vertical stress might due to the generation of cracks on eggshells.

(4) Shear wave velocity result probably reflected the effects of calcite from eggshell powders on Ottawa sand;

(5) SIP can detect both size and precipitated particle distribution, and could provide valuable information for in-situ monitoring of heterogeneous and multiphase evolution processes, such as MICP.
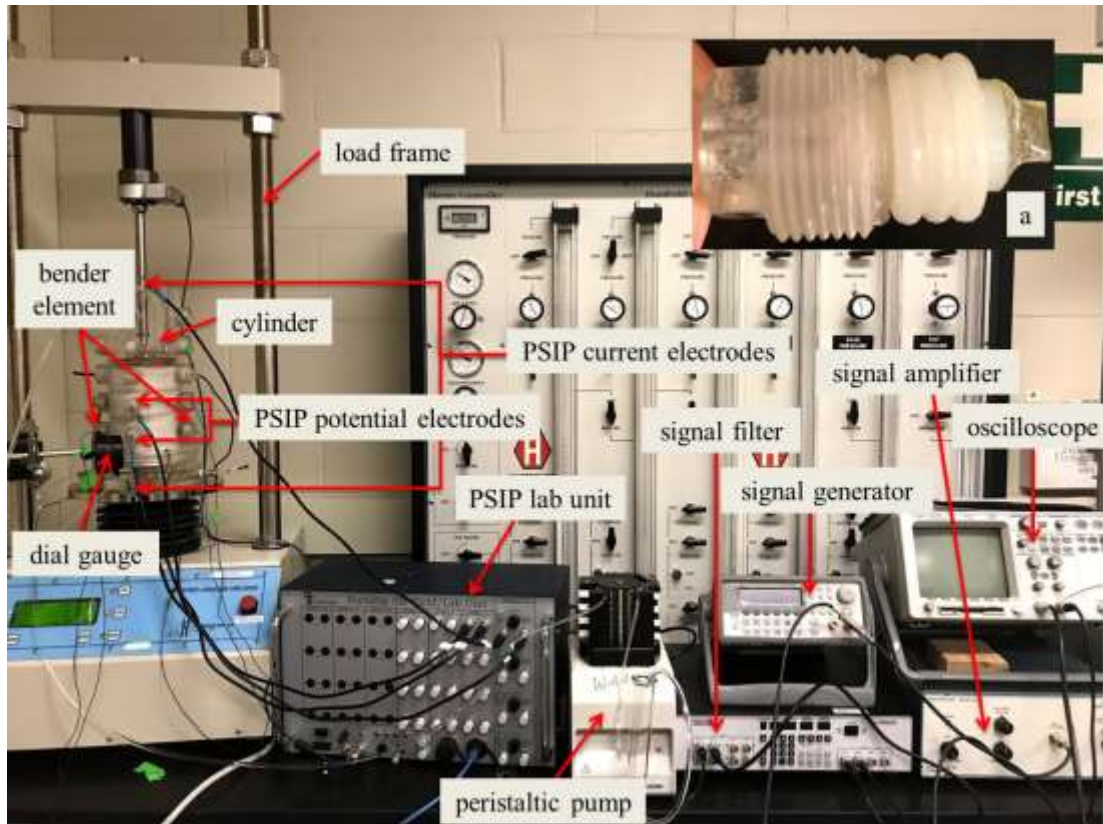
Figure 1. Experimental setup with SIP lab unit and BE testing system; inset: a bender element unit.
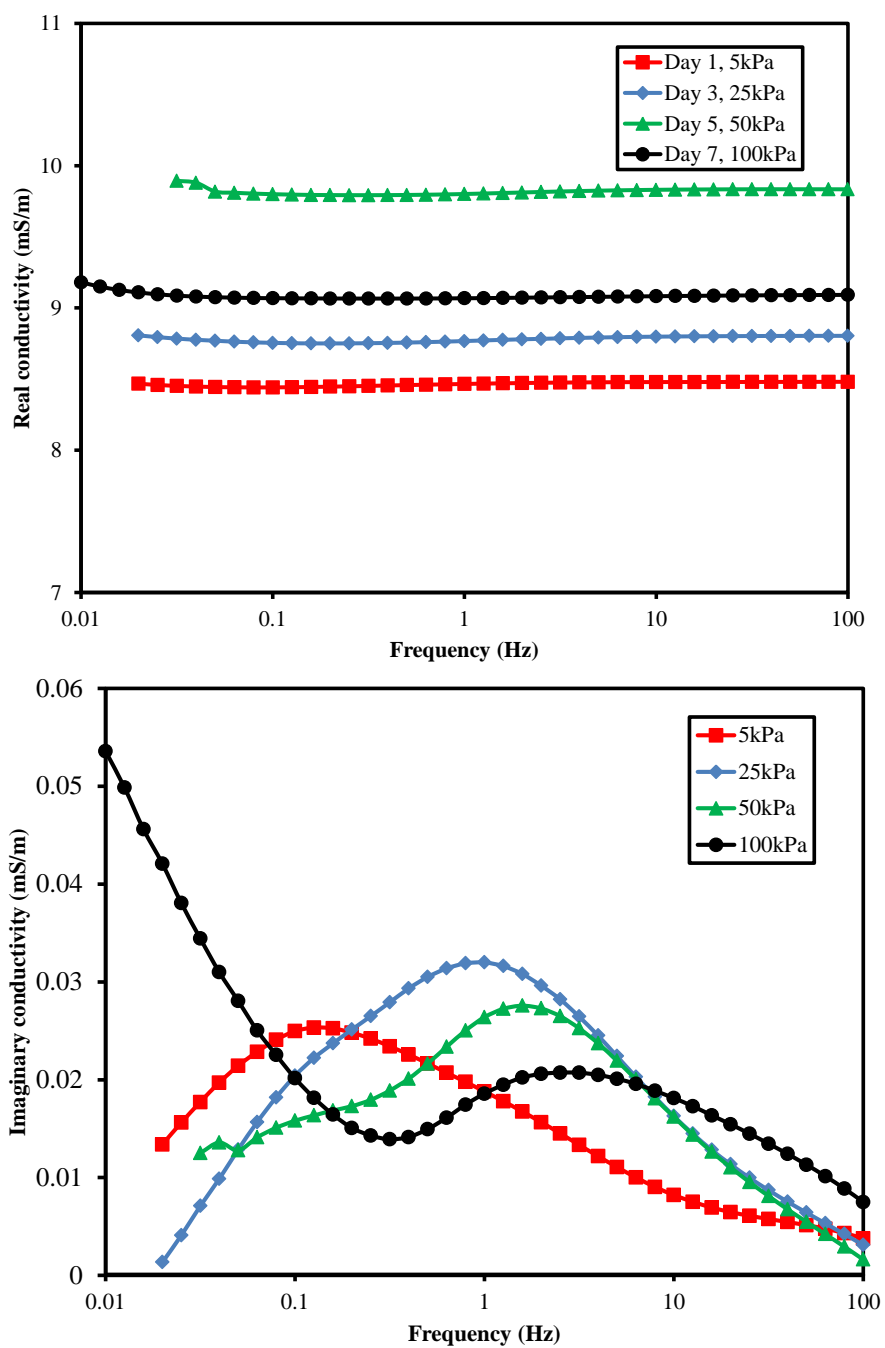
Figure 2. Tested spectral (a) real and (b) imaginary conductivities.
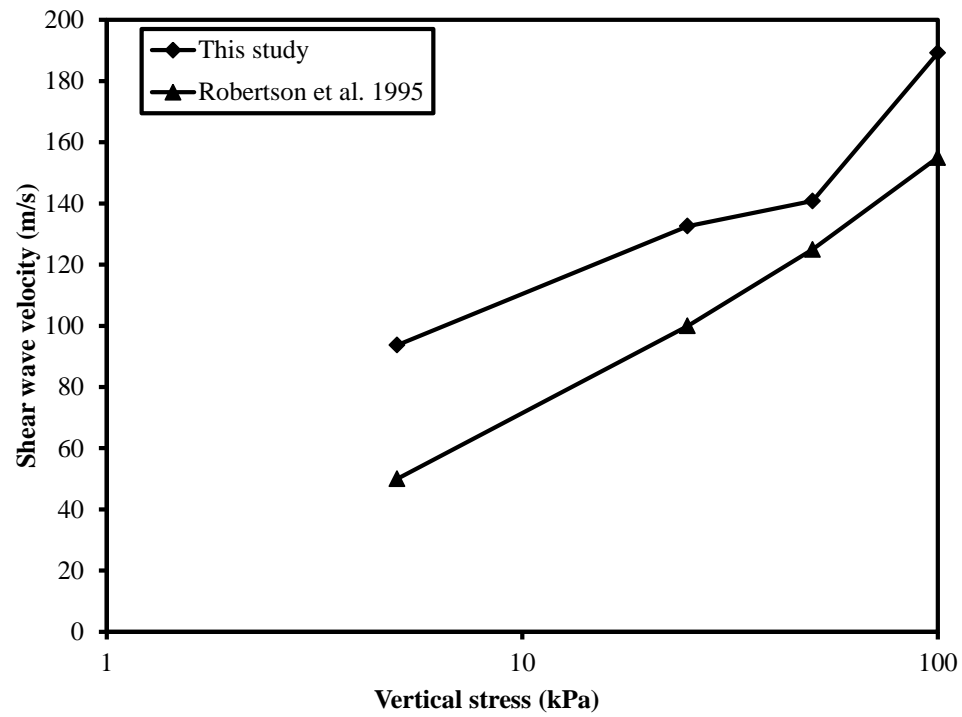
Figure 3. Shear wave velocity versus vertical stress.

Table 1. Estimated mean particle sizes of sand and eggshell powder using Eq. 3.

Vertical stress (kPa)	Time (day)	Peak frequency (Hz)	Relaxation time (s)	Particle size (mm)
5	1	0.126	1.263	0.116
25	3	1	0.159	0.041
		0.1	1.592	0.130
50	5	1.58	0.100	0.033
		0.1	1.592	0.130
100	7	2.512	0.063	0.026
		≤ 0.010	≥ 15.915	≥ 0.412

REFERENCES

Cole, K. S., Cole, R. H. (1941). Dispersion and Absorption in Dielectrics I. Alternating Current Characteristics. J. Chem. Phys. 9 (4): 341 − 351

Kang, X., Kang, G.-C., Bate B. (2014). Measurement of Stiffness Anisotropy in Kaolinite Using Bender Element Tests in A Floating Wall Consolidometer. Geotech. Test. J., 37.

Lee, J.-S., Santamarina, J. C. (2005), Bender Elements: Performance and Signal Interpretation. J. Geotech. Geoenviron. Eng., 131(9): 1063–1070.

Pelton, W. H., Ward, S.H., Hallof, P.G., Sill, W.R., Nelson, P.H. (1978). Mineral discrimination and removal of inductive coupling with multifrequency IP. Geophys., 43: 588-609.

Ribeiro, Ana C.F., Barros, Marisa C.F., Teles, Ana S.N., Valente, Artur J.M., Lobo, Victor M.M., Sobral, Ab Íio J.F.N., Esteso, M.A. (2008). Diffusion coeficients and electrical conductivities for calcium chloride aqueous solutions at 298.15 K and 310.15 K. Electrochim. Acta, 54: 192–196.

Robertson, P. K., Sasitharan, S., Cunning, J. C., Sego, D. C. (1995). Shear-wave velocity to evaluate in-situ state of Ottawa sand. J. Geotech. Eng., 121(3): 262-273.

Santamarina, J. C., Cho, G. C., (2001). Determination of critical state parameters in sandy soils-Simple procedure. Geotech. Test. J., 24(2): 185-192.

Schwarz, G. (1962). A theory of the low-frequency dielectric dispersion of colloidal particles in electrolyte solution1,2. J. Phys. Chem., 66: 2636 −2642.

Weil, M. H., DeJong, J.T., Martinez, B. C., Mortensen, B. M. (2012). Seismic and resistivity measurements for real-time monitoring of microbially induced calcite precipitation in sand. Geotech. Test. J., 35: 330-341.

Wu, Y., Ajo-Franklin, J., Spycher, N., Hubbard, S., Zhang, G., Williams, K., Taylor, J., Fujita, Y., Smith, R. (2011). Geophysical monitoring and reactive transport modeling of ureolytically-driven calcium carbonate precipitation. Geochem. Trans., 12 (1), 7.

Wu, Y., Hubbard, S., Williams, K. H., Ajo-Franklin, J. (2010). On the complex conductivity signatures of calcite precipitation. J. Geophys. Res., 115, G00G04.

Wu, Y., Slater, L. D., Korte, N. (2005). Effect of Precipitation on Low Frequency Electrical Properties of Zerovalent Iron Columns. Environ. Sci. Technol., 39 (23), 9197 −9204.

Zhang, C., Slater, L., Redden, G., Fujita, Y., Johnson, T., Fox, D. (2012). Spectral induced polarization signatures of hydroxide adsorption and mineral precipitation in porous media. Environ. Sci. Technol., 46: 4357 −4364.

Zhu, J., Cao, J.N., Bate, B., Khayat, K.H. (2018). Determination of mortar setting times using shear wave velocity evolution curves measured by the bender element technique. Cem. Concr. Res., 106:1-11.

III. MICROSCOPIC AND PHYSICOCHEMICAL STUDIES OF POLYMER-MODIFIED KAOLINITE SUSPENSIONS

Junnan Cao[1], Xin Kang[2] and Bate Bate[3]

[1]Graduate Research Assistant, Department of Civil, Architectural, and Environmental Engineering, 1401 North Pine Street, Missouri University of Science and Technology, Rolla, MO 65409. Email: jcg83@mst.edu

[2]Associate Professor, College of Civil Engineering, Hunan University, China, P.R.; Formerly, Phd candidate, Department of Civil, Architectural, and Environmental Engineering, Missouri University of Science and Technology, Rolla, MO, United States

[3]"100-Talents Program" Professor, Institute of Geotechnical Engineering, College of Civil Engineering and Architecture, Zhejiang University, 866 Yuhangtang Road, Hangzhou, China 310058. Email: batebate@zju.edu.cn; Formerly, Assistant Professor, Department of Civil, Architectural, and Environmental Engineering, 1401 North Pine Street, Missouri University of Science and Technology, Rolla, MO 65409

ABSTRACT

Sedimentation tests on kaolinite in biopolymers (xanthan gum, chitosan, polyacrylic acid and polyacrylamide) solutions were conducted and recorded with time-lapsed technique up to 35 days. Microscopic particle size, zeta potential, final volume and solid content were measured along the elevation of the graduated cylinder at the end of tests, and settling velocity and intensity calculated. Test results suggested that positive charged edges of kaolinite particles attached to negatively-charged xanthan gum (0.001 and 0.5 g/l) long chain via electrostatic force, exhibiting edge-to-edge (EE) fabric structure, and that charge neutralization was the primary interaction mechanism between kaolinite and either chitosan (0.05 and 5 g/l) or PAA (0.05 and 1 g/l), and that steric

stabilization dominates the interaction between kaolinite and PAM molecules at 0.1 and 0.5 g/l PAM solutions.

KEYWORDS: biopolymers, zeta potential, microscopic particle size, time-lapse.

1. INTRODUCTION

Grain size distribution (GSD) of the aggregates (or flocs) of a fine-grained soil in marine or lacustrine environments has been studied primarily in mesoscale (0.25 μm to 1 mm) due to its relevance to the macroscale mechanical or fluid dynamic behaviors (Zhang et al., 2013). At microscopic (sub-micron) scale, however, GSD and the physicochemical properties of fine-grained soils, which govern the fabrics and characteristics of flocs, are still not well understood. On the other hand, Stoke's law (Eq. 1) predicted the terminal velocity of small particles in a suspension:

$$v = \frac{F_d}{6\pi\mu r} \tag{1}$$

where F_d is the frictional force (unit: N) acting on the interface between fluid and particle, also known as Stokes' drag, μ the dynamic viscosity (unit: Pa), r (m) the radius of the spherical object, and v (m/s) the flow velocity relative to the object. However, the real sedimentation process is complicated by particle colliding (Han and Lawler, 1992; Thomas et al., 1999), Coulombic interactions (Santamarina, 2001), van der Waals interactions (Israelachvili, 2011; Palomino and Santamarina, 2005; Zaman, 2003), and Brownian motions (Han and Lawler, 1992; Zhang et al., 2013), which render significant difficulties in simulating the sedimentation process of fine grain soils. Zeta potential,

which is a good indicator of the inter-particle forces, yields insight into the interaction between the clay particles and the fluid phase (Bate and Burns, 2010; Hunter et al., 1981).

Polymers emerged as new engineering materials in recent decades due to their environmental-friendly nature, minimal carbon footprint, and high efficiency. Polymer modification has been widely used in several disciplines, including chemical enhanced oil recovery (Pefferkorn, 1999; Shah and Schechter, 1977; Sorbie, 1991; Stutzmann and Siffert, 1977), soil erosion control (Lentz et al., 1992; Lentz and Sojka, 2000; Nugent et al., 2010; Yu et al., 2003; Zhang et al., 1998), dewatering of mine tailings (Beier et al., 2013; McFarlane et al., 2005; Mpofu et al. 2003), dredging of sediments (Hunter et al., 2006; Jones et al., 1978; Wang and Chen, 1977), waste water treatment (Cleasby et al., 1989; Letterman and Pero, 1990) and soil stabilizations (Ates 2013; Kang and Bate, 2016; Newman and Tingle 2004). Despite these applications, the interaction mechanisms between polymers and soil particles have not been fully explored. Polymer bridging and charge neutralization are the two major interaction mechanisms (Bergaya et al., 2006; Chaplain et al., 1995; Theng, 1979). Polymer bridging occurs when soil particles are brought together, sometimes forming flocculation, via hydrogen bonding between the end functional groups on the polymer chain and the sites on clay surfaces (Csempesz and Rohrsetzer, 1988; Mpofu et al., 2003; Otsubo, 1994; Zaman, 2003). Charge neutralization, on the other hand, occurs when polymer chain with cationic functional groups adsorbed onto clay mineral surfaces and modified the particle fabrics (Mpofu et al., 2003). Besides, depletion flocculation and stabilization are the less common mechanisms which are generated by dissolving nonionic polymer into the dispersions. The depletion interactions are induced by the unbalanced osmotic force caused by the exclusion of the free non-

adsorbing polymer molecules from the space between the two approaching particles (Feigin and Napper, 1980). The effects of polymers on the clay particles behaviors are complicated, and the acting mechanisms often depend on solid concentration (Lee et al., 1991), cation exchange capacity (Theng, 2012), polymer dosage and molecular weight (Das and Somasundaran, 2003), adsorption density of polymer (Zaman, 2003), types of polymer functional groups (Bergaya et al., 2006) and pH (Kim and Palomino, 2011; Bertolino et al., 2017).

Time-lapse visualization of sedimentation process has been used for years in the study of glaciers (Miller and Crandell, 1959), soil movement and erosions (Hayward and Barton, 1969; Matsuoka, 2014; Shellberg et al., 2013) and earth flow movement (Grandell and Varnes, 1961). Time-lapse technique in monitoring the sedimentation process saves labor and provides turbidity information that linked to final volume, settling rate and maybe even solid content, even though the aqueous turbidity could be directly detected by Analytic Jena Specord S 600 BU machine (Cavallaro et al., 2012).

This study aims at elucidating the fundamental mechanisms on the effects of sodium chloride (NaCl) and four polymers (xanthan gum, chitosan, polyacrylic acid and polyacrylamide) with kaolinite. To achieve this goal, the following tasks will be performed: First, a series of sedimentation tests for kaolinite and polymer mixtures with time-lapsed recording were performed. When final volume was reached, particle size, zeta potential and solid content were measured. Finally, the relationship between the microscopic/physicochemical properties and the macroscopic sedimentation behaviors (final volume, settling velocity and intensity) were proposed.

2. MATERIALS AND METHODOLOGY

Georgia kaolinite (RP-2, properties are shown in table 1) was homoionized with sodium cations before use. The homoionization process is similar to that in Bate and Burns (2010), and a brief description was given below. 2 kg of kaolinite was added to 14 liter of 2.0 mol/l NaCl solution. The resulting suspension was mechanically stirred for 15 min and allowed to stand for at least 24 hours for gravity separation. The supernatant was then siphoned off, and the solids were rinsed with de-ionized water to remove any loosely bound cations. This process was repeated until the electrical conductivity of the supernatant was below 350 μS/cm.

Traditional method of oven-drying a slurry and mechanical grounding to obtain the solid powder will break kaolinite plates (Zbik and Smart, 2005), and therefore was not adopted in this study. Instead, after Na-homoionization, the slurry was manually stirred for 5 minutes to obtain a uniform suspension, which was siphoned into graduated cylinders for the sedimentation tests. In order to obtain consistent solid content, suspension volume calibration tests were performed. It was found out that 85 ml of uniform suspension contained consistently 10 ± 0.1 g of solids. Therefore, 85 ml of uniform suspension was extracted for each 100 ml graduated cylinder, and approximately 15 ml of solutions with prescribed chemical concentrations was added to reach the full volume of 100 ml. The resulting chemical concentrations of different chemicals (NaCl, Xanthan gum, Chitosan, polyacrylic acid or polyacrylamide) in 100 ml kaolinite slurries were summarized in Table 2. The molecular structures of xanthan gum (Pfaltz&Bauer, CAS#: 11138-66-2), chitosan (Alfa Aesar, CAS#: 9012-76-4. 85% deacetylated), polyacrylic acid (PAA) (Polysciences, Inc., Lot#: 541449) and polyacrylamide (PAM)

(Acros Organics, CAS#: 62649-23-4) used in this study were shown in Fig. 1. Molecular weights of above polymers are given in Table 3.

A 360° rotational sedimentation panel (Fig. 2) was developed in this study to simultaneously measure slurries in up to 28 graduated cylinders. Graduated cylinders were locked onto the shelves of the panel. After slowly rotating the sedimentation panel for 5 minutes to ensure uniform slurries, the panel was locked, graduated cylinders stood upright, and the sedimentation process started. Time-lapse photos were taken for all the tested graduated cylinders with high resolution digital camera (Canon EOS 5d Mark II, Canon, Japan). The time intervals are as follows: 1 min interval in the first 1 hr, 30 min interval in the following 19 hr, 2 hr interval in the following 11 days, 4 hr interval in the following 8 days, and then 24 hr interval for another 15 days (total of 35 days). No further changes were observed in all the graduated cylinders after 35 days. The interface between supernatant and suspension, and that between suspension and sediment ("mud line") as a function of time were read (accuracy about 0.5 ml) from the time-lapse photos. Then the mud line vs. time readings were plotted, and the initial linear portion of the curve was used to determine the initial settling rate α. The final volume of the sediment was taken from the last time-lapse photo at time of 35 days.

After the final volume was reached, approximate 0.5 ml slurry were extracted by transfer pipettes (Fisherbrand, graduated 3 ml , Cat No. 13-711-9AM, Fisher scientific) and pipettor (D64362, Fisherbrand, 200-1000 µl) at selected elevations of the graduated cylinder and transferred into 2.5 ml macro disposable cuvettes (759071D, BRAND GMBH+CO KG, Fisher scientific) for zeta potential or grain size distribution measurement. The elevation selection for grain size distribution is as follows. 1-2

elevations in supernatant were selected, with one elevation near the top. 3-4 elevations were taken from the suspension, with one elevation slightly above the "mud line" if perceived. 2-3 elevations were chosen from the sediment, with one elevation at the bottom. The preliminary results in this study indicated that zeta potential did not vary significantly with elevation. Therefore, the elevation selection for zeta potential was reduced to one elevation at each of the three locations: supernatant, suspension, and sediment. Average results were calculated for further discussion. Care was taken to minimize the disturbance by low extraction flowrate.

Zeta potential was measured with Zetasizer Nano ZS90 zeta potential analyzer (Malvern Instruments, UK) and folded capillary cell (DTS 1061, Malvern Instruments, UK). High-accuracy pipette (D64362, Fisherbrand, 200-1000 μl) was used to transfer 500 μl samples into the folded capillary cell. Two cycles were used to take zeta potential values, and average values were reported. Repeat tests were performed until the last 3 readings were within +/- 10 mV. Before each measurement the folded capillary cell was first rinsed with ethanol (Fisher Scientific) then with deionized water 3 times to prevent cross-contamination. The test temperature was set at 23.5 ^{o}C. The Zetasizer was calibrated prior to measurement by using the standard calibrating solution (Duke 3520A, Hi-Q Nano sensor calibrant). Some samples in the middle section and all samples in the bottom section exceeded the solid content measurement limit of ZetaSizer. Therefore these samples were diluted 100 times in 2.5 ml macro disposable cuvette with deionized water with the exception of NaCl-kaolinite mixture, where NaCl solution of the original concentration was used for dilution. This is because sodium was not as strongly adsorbed

on the kaolinite surface as the other 4 polymers used in this study (Bate and Burns, 2010;

Mopfu et al., 2003).

The grain size distribution of kaolinite particles were measured by dynamic light scattering technique with Malvern Zetasizer Nano ZS90 and 10 mm lightpath, 1.5 ml capacity semimicro style polystyrene cuvettes (Cat No. 14-955-127, Fisherbrand, Fisher scientific). All NaCl/polymer-kaolinite mixtures were preconditioned to 25 ^{o}C before testing. High accuracy pipette (D64362, Fisherbrand, 200-1000 μl) was used to transfer 500 μl samples into 2.5 ml macro disposable cuvettes. Similar to the zeta potential test, high solid concentrations can exceed the measurement limit of ZetaSizer. So samples from suspensions and sediments were diluted 10 times (20 μl mixture: 200 μl deionized water/NaCl solutions) before the particle size distribution measurement. 20 μl mixture was transferred by using high accuracy pipette (5 μl, Eppendorf Research) with the range from 10 μl to 100 μl. Dilution was performed in 1.5 ml disposable plastic cuvettes with deionized water for polymer-kaolinite mixtures, or with NaCl original concentration solutions for NaCl-kaolinite mixtures. It was observed that clusters of kaolinite aggregates taken from the sediments and some suspensions would settle to the bottom of the cuvettes during dilution, which would not be detected by Zetasizer. In order to avoid this problem, the cuvette was gently rotated immediately before the test to agitate the kaolinite clusters into the entire aqueous space. Care was taken not to destroy the cluster structure. Some samples were re-tested after a few minutes to confirm/improve the results. At least one repeat test with a fresh sample was performed at each elevation. Cumulative density function of lognormal distribution model was selected to fit the particle size

distribution curves of kaolinite. The mean values and standard deviations of kaolinite particle size were taken into account and calculated for the later discussion.

The solid content profile along the elevations was measured after the final volume was reached. The supernatant was first siphoned out with a pipet at 10 - 20 ml intervals, followed by the suspension and sediment. Care was taken not to disturb the suspension and the sediment by extracting from the surface and by low extraction flowrate. The volume intervals were separated at the interface (mud line) between the suspension and the sediment. Each volume interval was moved to a small beaker (25 ml), which was then weighed (Ohaus EX224, Fisher Scientific), oven-dried (104 ^{o}C), and weighed again for the water content measurement. Then the solid content at each volume interval was reported in terms of the solid weight percentage: weight of solid/total weight. It was noted that some solid particles were attached to the side of the graduated cylinder. However, over 90% of the solid particles were extracted into the beaker as oven-dried solid mass indicate, which warranted the representativeness of the results.

The intensities of kaolinite particles in each polymer along the elevation were plotted by using Matlab. Firstly, the rgb2gray function was taken to convert the true color image to the grayscale intensity image. After choosing the coordinates of the elevation of each cylinder using the getpts function, the intensity data on the grayscale image along each elevation can then be directly read and plotted by the plot function.

3. RESULTS

The final volumes of kaolinite in NaCl, xanthan gum, chitosan, PAA and PAM solutions were shown in Fig. 3. The zeta potential curves of kaolinite in different

concentrations of NaCl/polymer solutions are plotted in Fig. 4. The profiles of the mean

particle size and solid contents of kaolinite along the elevations in the five solutions were

presented in Figs. 5 and 6, respectively. And Fig. 7 demonstrated the intensity curves of

kaolinite along the elevations as time progressed in 0.15 mol/l NaCl and 0.05 g/l PAA

solutions. The intensity curves in 0.003 mol/l NaCl, 0.001 and 0.5 g/l xanthan gum, 1 g/l

PAA, 0.1 and 0.5 g/l PAM and 0.05 and 5g/l chitosan solutions were very similar with

the curve in 0.05 g/l PAA solution. The sedimentation trends of kaolinite particles in

different concentrations of NaCl and polymers solutions were exhibited in Fig. 8 and the

settling velocities, α (ml/min) of kaolinite in NaCl and PAA solutions were calculated

and plotted in Fig. 9. From these figures, the following observations can be made:

3.1. NaCl

(1) The final volume and mean particle size of kaolinite increased with the

increment of NaCl concentration (Figs. 3 and 5a). (2) The solid contents decreased as the

concentration of NaCl increased, especially under the elevation of 15 ml (Fig. 6a). (3) A

clear boundary was found on 0.15 mol/l NaCl intensity curve as time went on (Fig. 7a).

This agreed with the final volume result (41.5 ml) shown in Fig. 3. (4) The settling

velocity decreased with the increment of NaCl concentration (Fig. 9).

3.2. XANTHAN GUM

(1) The final volume and profiles of both the particle size and solid content for

kaolinite in 0.001 g/l xanthan gum solution (Figs. 5b and 6b) were very close to those for

kaolinite in 0.003 mol/l NaCl solution (both at around 15 ml) (Figs. 3, 5a and 6a). This

suggests that the xanthan gum dosage of 0.001 g/l (electrical conductivity = 2.441 us/cm)

is probably insignificant to change the fabric structures of kaolinite particles (fresh washed kaolinite suspension: electrical conductivity= 328.7 us/cm). (2) The final volume of kaolinite in 0.5 g/l xanthan gum solution (21.5 ml) was higher than that in 0.001 g/l solution (15 ml) (Fig. 3). (3) Under the mud line, the kaolinite particle sizes were larger in 0.5 g/l solution than those in 0.001 g/l solution at the same elevation (Fig. 5b).

3.3. CHITOSAN

(1) The mean size of kaolinite particles ranged from 100 to 600 nm along the elevation in both chitosan solutions, and (2) the particle size was influenced slightly by the two chitosan concentrations, except for those at the elevation of 18 ml in 5 g/l solution, where the maximum particle size is around 900 nm (Fig. 5c). (3) The mud lines of final volume of kaolinite were around 14 ml in 0.05 g/l and 20 ml in 5 g/l chitosan solutions (Fig. 3).

3.4. PAA

(1) Profiles of both the mean particle size and solid content of kaolinite did not vary too much in all different concentrations of PAA solutions, and (2) most of the kaolinite particles were smaller than 600 nm, but few particles are larger than 900nm in 0.05 and 1 g/l solutions (Figs. 5d and 6d). (3) The final volume increased with the increment of PAA concentration (Table 4). (4) The settling velocity decreased as the PAA concentration increased (Fig. 9).

3.5. PAM

(1) Both the profiles of the mean particle size and solid content for kaolinite along the elevation in 0.1 and 0.5 g/l polyacrylamide (PAM) solutions were similar to each

other, if the standard deviations of the particle size were taken into consideration (Figs. 5e and 6e). (2) All the particle sizes detected were smaller than 900 nm in both PAM solutions. (3) The final volume of kaolinite in 0.1 g/l solution was around 20 ml, which was close to that in 0.5 g/l solution at around 21 ml (Fig. 3). (4) The sedimentation volumes shown on sedimentation trends (Fig. 8c) decreased firstly and then increased until the values became stable in both PAM solutions.

4. DISCUSSION

4.1. NaCl

Based on the fabric map developed by Palomino and Santamarina (2005), kaolinite particles were primarily deflocculated and dispersed in low concentration of NaCl solution (< 0.1-0.15 mol/l) at pH = 5-7.2. With the increment of NaCl concentration, most of them formed edge to face (EF) fabric structures due to the decrement of electronic double layer thickness and the repulsive force. Further increasing the concentration of NaCl, until it reached the threshold concentration ($\approx$ 0.1-0.15 mol/l), kaolinite particles converged into edge to edge (EE) fabric structure. This conclusion agreed with the observations made in this study. Kaolinite particles were mainly dispersed in 0.003 mol/l NaCl solution. Thus, mainly small particles (< 500 nm) were detected. EF and EE fabrics were formed in 0.015 and 0.15 mol/l solutions respectively. Therefore, large particles (> 900 nm) were measured, especially those with the size larger than 1500nm in 0.15 mol/l NaCl solution. Due to the formation of fabric structures, final volumes in 0.015 (30 ml) and 0.15 mol/l (41 ml) solutions are larger than that in 0.003 mol/l solution (15 ml).

4.2. XANTHAN GUM

The dissociation of carboxyl functional groups (-COOH) along the xanthan gum polymeric chain (pKa value of 3.1, Oprea et al., 2013) releases protons in aqueous solution (Fig. 1a): $R\text{-COOH} \rightarrow R\text{–COO}^- + H^+$ (Dontsova and Bigham, 2005). This reaction has two effects on kaolinite suspensions in xanthan gum solutions: (1) the negative charges from $–COO^-$ caused the zeta potential of the solution to become more negative and the values dropped from -38.7 down to -45.2 mV with the increment of xanthan gum concentration from 0.001 to 0.5 g/l (Fig. 4). In addition, those negative charges repulsed the faces of kaolinite particles which were also negative charged in pH $\approx$ 4-7 solutions (Palomino and Santamarina, 2005). Therefore, the solutions were dominated by the steric repulsive force, which hindered the bridging effects between kaolinite particles and xanthan gum polymers. The final volume increased (Fig. 3, 21.5 ml > 15 ml) and the solid content slightly decreased (Fig. 6b) in 0.5 g/l xanthan gum solution due to the higher repulsive force compared to those in 0.001 g/l solution (Cavallaro et al., 2013). The particle size should not increase with the increment of xanthan gum concentrations from 0.001 to 0.5 g/l, which disagreed with the test results shown in Fig. 5b. However, this could be explained by the H^+ effect which was discussed as follows. (2) The released H^+ reduced the pH of the suspension, which likely renders more positive charges to the edges of kaolinite particles (Palomino and Santamarina, 2005; Zhang et al., 2013). Those positive charges attracted the negative charged xanthan gum molecule via electrostatic force. Thus, it was postulated that kaolinite particles attached to the long xanthan gum polymer chain exhibited a pattern similar to edge to edge (EE) fabric structure, resulting in the large particles (> 900nm) in 0.5 g/l xanthan

gum solution under the mud line of 21.5 ml (Fig. 5b). Above postulation was validated by the SEM image (Fig. 6b) where the EE fabric structure was observed.

4.3. CHITOSAN

The primary interactive mechanisms between chitosan and kaolinite are charge neutralization and interparticle bridging effect (Li et al., 2013). Firstly, the amine functional groups ($-NH_2$) along the chitosan chain (Fig. 1b) (85% deacetylated) attract protons from water molecule in aqueous solution, which makes the chitosan chain positively charged. The positive chitosan chains are attracted to the negative faces of kaolinite particles by electrostatic force at pH = 7.59-8.49, which slightly increases the net surface charge of kaolinite (less negative). Zeta potential, an indicator of net surface charge of a solid, of kaolinite suspensions increases mildly (from -41 to -40 mV) with the increment of chitosan concentration (from 0.05 to 5 g/l) (Fig. 4). This is probably due to the small dosage of chitosan used in this study (mass ratio of kaolinite and 5 g/l chitosan = 21:1). The analogous profiles of kaolinite particle sizes along the elevation in chitosan and 0.003 mol/l NaCl solutions suggests that the interactive mechanism between chitosan and kaolinite is probably the same with NaCl and kaolinite. In NaCl solution, it is charge neutralization. Secondly, most of chitosan chains adsorb onto kaolinite particle faces in patches (Fig. 10a) at the tested concentrations in this study due to the high charge density of kaolinite (CEC = 7.9 meq/100 g, Hazen Research Inc.) and short distances of deacetylated sites on chitosan chain (Bergaya et al., 2006; Li et al., 2013; Theng, 2012). Under these concentrations, the interparticle polymer bridging effects (Fig. 10b) play a secondary role to the electrostatic force (Chen and Wu, 2003; Li et al., 2013; Theng, 2012). Therefore, most of small particles (< 600 nm) were measured in both chitosan

solutions (Fig. 5c). It is postulated that large particles (800nm-900nm) detected in 5 g/l solution are possibly due to the interparticle bridging effect. And the bridging effect probably also caused a higher final volume (Fig. 3) and slightly smaller solid contents (Fig. 6c) in 5 g/l solution compared to those in 0.05 g/l solution (20 ml > 14 ml). Overall, the sedimentation results suggest that charge neutralization dominates the interaction between kaolinite and chitosan solutions.

4.4. PAA

The primary interactive mechanisms between PAA polymer and kaolinite particle are charge neutralization and bridging effect: (1) PAA is negative charged in aqueous solution due to the dissociation of carboxyl functional groups (-COOH) along the polymer chain (Fig. 1c, pKa = 4.5). The octahedral alumina side of kaolinite face is positive charged at pH ≈ 4 (Palomino and Santamarina, 2005). Therefore, negative PAA polymers mainly adsorb on the positive alumina side of kaolinite face and edge by charge neutralization in acidic solution (Pan et al., 2001; Santhiya et al., 1999; Zaman et al., 2002). This adsorption renders more negative surface charges, as confirmed by the zeta potential decrement from -39.1 to -46.5 mV with the increment of PAA concentration from 0.05 to 1 g/l (Fig. 4). (2) PAA polymers can interact with kaolinite particles via hydrogen bonding between the hydroxylated alumina side of kaolinite face and carboxyl groups of PAA polymer (Santhiya et al., 1999) or interparticle bridging effect due to the partially adsorption of PAA polymers on the alumina side of kaolinite face (Das and Somasundaran, 2003; Pan et al., 2001).

The distinct bridging effect based on previous study (Das and Somasundaran, 2003) occurred in the solution with small PAA concentration (< 0.001 g/l) and large

molecular weight ($\geq 2.5 \times 10^5$ g/mol). The bridging effect is weakened with the increment of PAA concentration, even though the molecular weight is larger than 2.5×10^5 g/mol. This is probably because of the high repulsive forces from charge neutralization between kaolinite particles (Das and Somasundaran, 2001). When the PAA concentration is larger than ~ 0.01 g/l, as is the case in this study, the PAA polymer chain primarily crowds in a coiled form on alumina side of kaolinite surface (Fig. 10c) in acidic condition (Das and Somasundaran, 2001; Theng, 1979; Tjipangandjara and Somasundaran, 1992). This coiled form hinders the bridging effect between PAA and kaolinite, leaving charge neutralization to be the dominant mechanism. Therefore, small particles (< 600 nm) were mostly detected in both PAA solutions (Fig. 5d). It should be pointed out that few kaolinite particles could still flocculate because of limited bridging effect as few large particles ($\geq$900 nm) were measured in both PAA solutions (Fig. 5d). The kaolinite particles tend to disperse in the PAA solution with high concentration (low settling velocity, Fig. 9) due to the increment of repulsive force, which is mostly generated by the adsorption of PAA polymers on the kaolinite surface (Fig. 10c). Thus, the final volume in 1 g/l PAA solution (75 ml) is larger than that in 0.5 g/l solution (25 ml) (Table. 2), whereas the solid content, in turn, is smaller in 1 g/l solution because of the reduction of density of solids. And also the settling velocity decreased with the increment of PAA concentrations. It is also noticed that solid contents increase slightly along the elevation in each PAA solution (Fig. 6d). This is attributed to gravity force and the subsequent consolidation of kaolinite particles (Gibson et al., 1981; Pu et al., 2013).

4.5. PAM

The high carboxyl content PAM used in this study has two functional groups: carboxyl and amide (Fig. 1d). Carboxyl groups (-COOH) hydrolyze into negative carboxylic ions ($-COO^-$) and positive hydrogen ions (H^+). The former gives negative charges to the polymer chain, while the latter generates acidic condition to the aqueous solution. When pH < 7.2, the edges of kaolinite particles become positively charged (Palomino and Santamarina, 2005), and attract the negatively charged PAM chains through electrostatic interaction. Meanwhile, the faces of kaolinite particles are still negatively charged and repel the PAM chains. On the other hand, another functional group on the chain, the amide functional group ($-CONH_2$) can be adsorbed on both the silanol and aluminol -OH groups on both the faces and edges of kaolinite particles by hydrogen bonding (Mpofu et al., 2003; Nabzar et al., 1986; Pefferkorn et al., 1984). Because of the poorly hydrated silica face and because of that hydrogen ions are relative tightly held on the aluminate faces, the amide groups are primarily hydrogen bonded to the broken edges of kaolinite platelets, which are composed of exposed silica and alumina (Nabzar et al., 1986 and 1988). Therefore, it can be inferred that high carboxyl content PAM polymer chain mainly adsorbs to the edge of kaolinite particles to form a fabric structure similar to edge to edge (EE) (Fig. 10d) by charge neutralization between carboxyl group and the edge of kaolinite particle and hydrogen bonding between the carbonyl of amide group and the free silanol at the edge of kaolinite particle.

This adsorption via charge neutralization increases with the increment of PAM concentration, but by bridging effects would be reduced (Mpofu et al., 2003). It is because of the overwhelming repulsive force produced by the negative PAM polymer

chains which are adsorbed onto two different edges of particle (Fig. 10e). The whole solution becomes steric stabilization. Nabzer et al. (1988) found that 0.95×10^{-3} g/l PAM is the threshold for 2 wt% kaolinite particles changing from EE bridging to steric stabilization, which is equivalent to ≈ 0.05 g/l PAM in this study. Hence, in 0.1 and 0.5 g/l PAM solutions, the interaction mechanism between PAM molecule and kaolinite particles is probably steric stabilization. This may be the reason that most particles detected in both solutions are under 900 nm (Fig. 5e). Due to the same interaction mechanism, the final volumes (~ 20 ml in 0.1g/l and ~ 21 ml in 0.5 g/l, Fig.3) and solid contents curves (Fig. 6e) are also similar in both PAM solutions.

5. CONCLUSIONS

This study examined the interaction mechanisms between polymer and kaolinite particles. Sedimentation tests on kaolinite in NaCl and biopolymers (xanthan gum, chitosan, polyacrylic acid and polyacrylamide) solutions were conducted and recorded with time-lapsed technique up to 35 days. A comprehensive set of data, including particle size, zeta potential and solid content along the elevation of the graduated cylinders, final volume and settling velocity were obtained. Major observations are summarized as follows:

(1) Coulombic interaction dominates the behavior of kaolinite-NaCl suspensions by compressing the electrical double layer surrounding both the faces and edges of kaolinite particles, and forming either edge-to-face (EF) kaolinite fabric in 0.015 mol/l NaCl solution or edge-to-edge (EE) kaolinite fabric in 0.15 mol/l NaCl solution, both of

which result in larger particle size (> 900 nm) and higher final volumes than a lower NaCl concentration (0.005 mol/l) does.

(2) Steric repulsive force between –COO$^-$ on xanthan gum chain and the negatively-charged sites on kaolinite face hinders the bridging effect between xanthan gum and kaolinite particles in 0.001 and 0.5 g/l xanthan gum solutions. On the other hand, protons released from the –COOH functional groups of xanthan gum chains accumulated on the kaolinite edges, which enhanced the attractions between positively-charged kaolinite edges and negatively-charged chain and exhibited layered structures with edge-to-edge connections between particles. As a result, large kaolinite particles (> 900nm) were presented in 0.5 g/l xanthan gum solution.

(3) The primary interactive mechanism between kaolinite and chitosan is charge neutralization. Most positively-charged chitosan chains adsorbed onto kaolinite faces in patches at 0.05 and 5 g/l solutions, leaving the interparticle bridging effect as a secondary mechanism. As a result, most small particles (< 600 nm) were presented in 0.05 and 5 g/l chitosan solutions. Some large particles (800nm-900nm) were also detected in 5 g/l solution, which is possibly due to the bridging effect between chitosan chains and kaolinite particles. This bridging effect is also believed to cause a higher final volume (20 ml vs. 14 ml) and slightly smaller solid contents in 5 g/l solution than in 0.05 g/l solution.

(4) Small kaolinite particles (< 600 nm) were primarily detected in PAA solutions, which is postulated to be due to the adsorption of the coiled form of positively-charged PAA chains on the alumina side of kaolinite faces. This coiled form hinders the bridging effect between PAA chains and kaolinite particles, promotes the interparticle repulsion, and leaves charge neutralization to be the dominant interaction mechanism. As PAA

concentration increased, charge neutralization and the subsequent interparticle repulsive forces lead to increment of final volumes, decrement of solid contents in sediment region, and decrement of settling velocity.

(5) In both 0.1 and 0.5 g/l PAM solutions, the interactive mechanism between PAM molecule and kaolinite particles is considered to be steric stabilization in the literature. Because of the interparticle repulsive force produced by the negative PAM chains adsorbed on adjacent kaolinite edges, the particle size is small (< 600 nm). Steric stabilization is short ranged, as a result, no large aggregates were formed, the final volume is low (20 ml in 0.1 g/l and 21 ml in 0.5 g/l solutions), and the solid content is high in the sediment region.

ACKNOWLEDGEMENTS
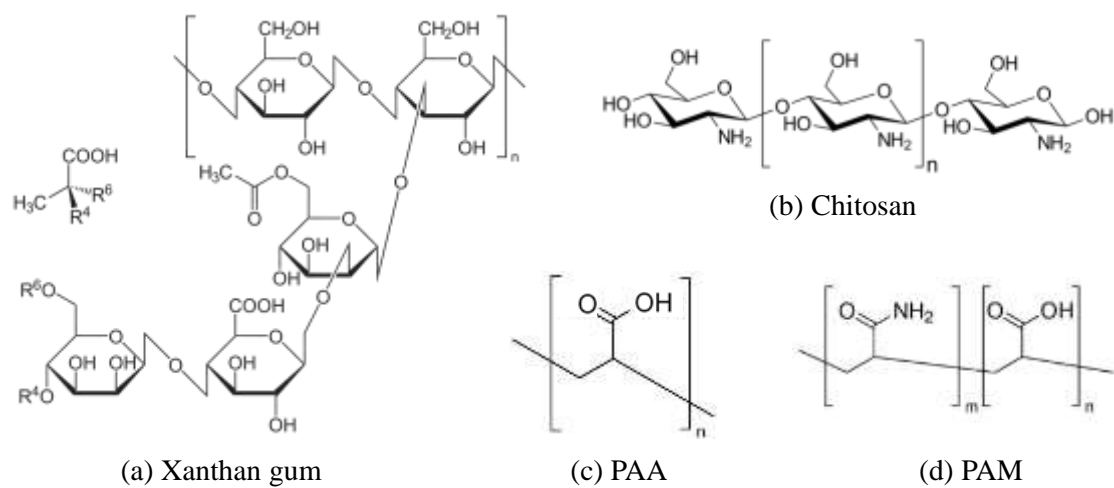
Figure 1. Molecular structures of biopolymers.

Figure 2. Sedimentation panel.
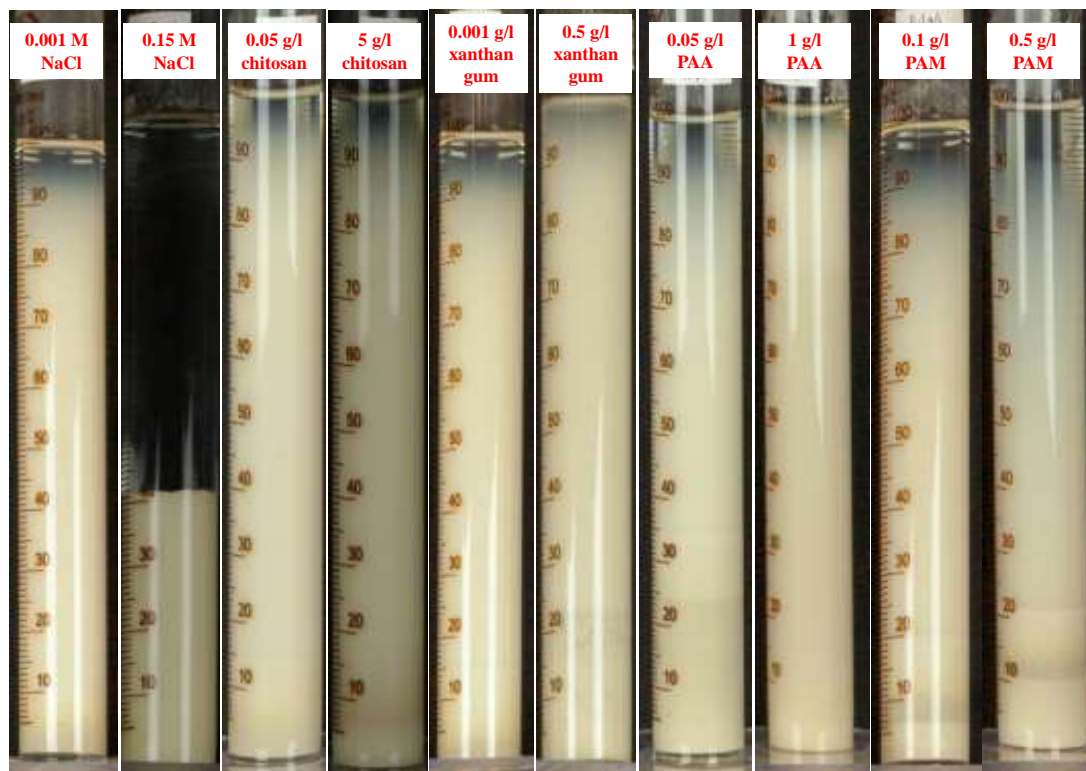
Figure 3. Final volumes of kaolinite in NaCl and polymers solutions.
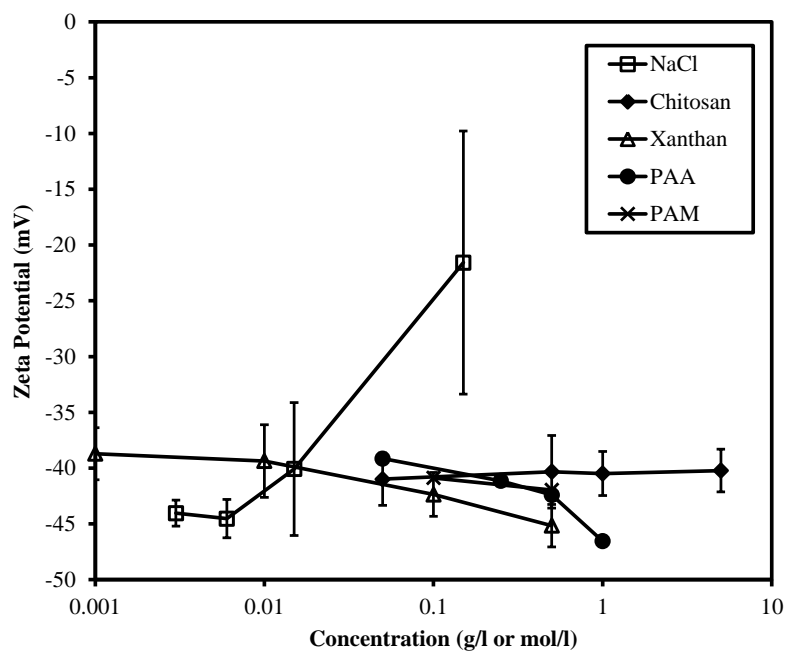
Figure 4. Zeta potential curves in NaCl/polymers solutions.
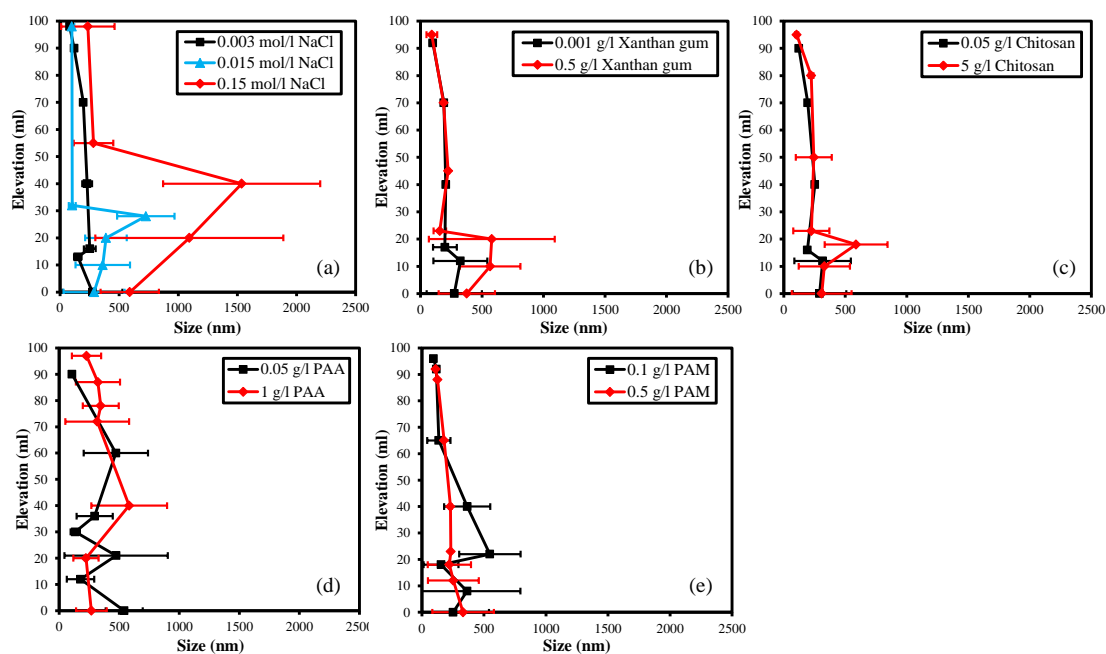
Figure 5. The profiles of the mean particle size of kaolinite along the elevation in different concentrations of NaCl and polymers solutions.
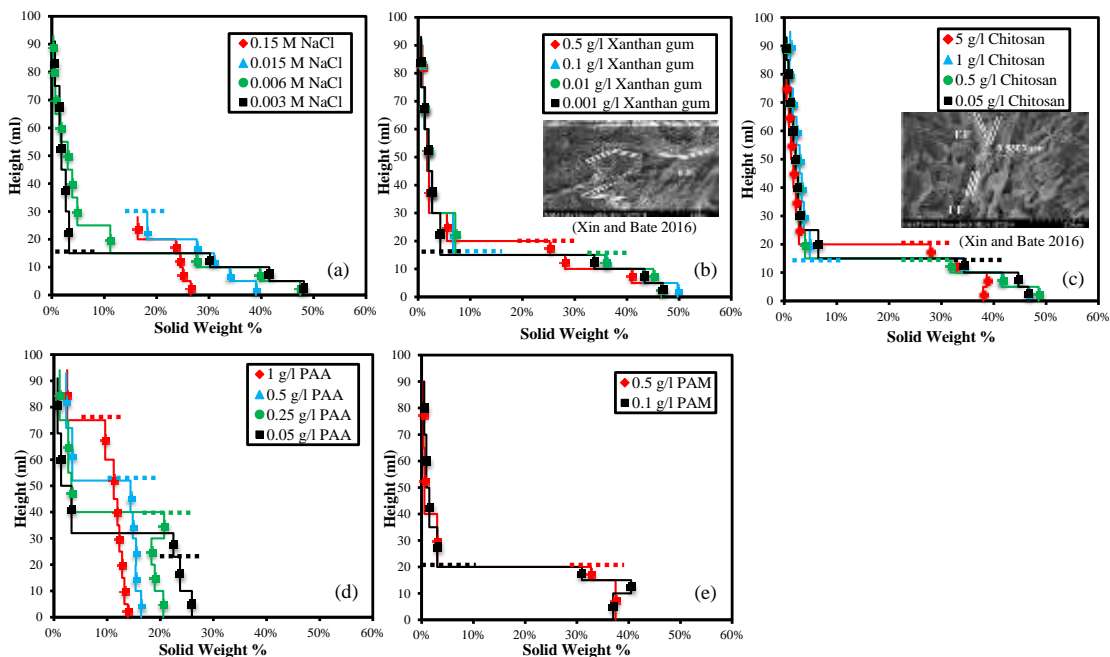
Figure 6. The profiles of solid contents of kaolinite along the elevation in different concentrations of NaCl and polymers solutions. (Dashed lines represent the mud lines between the sediments and suspensions).
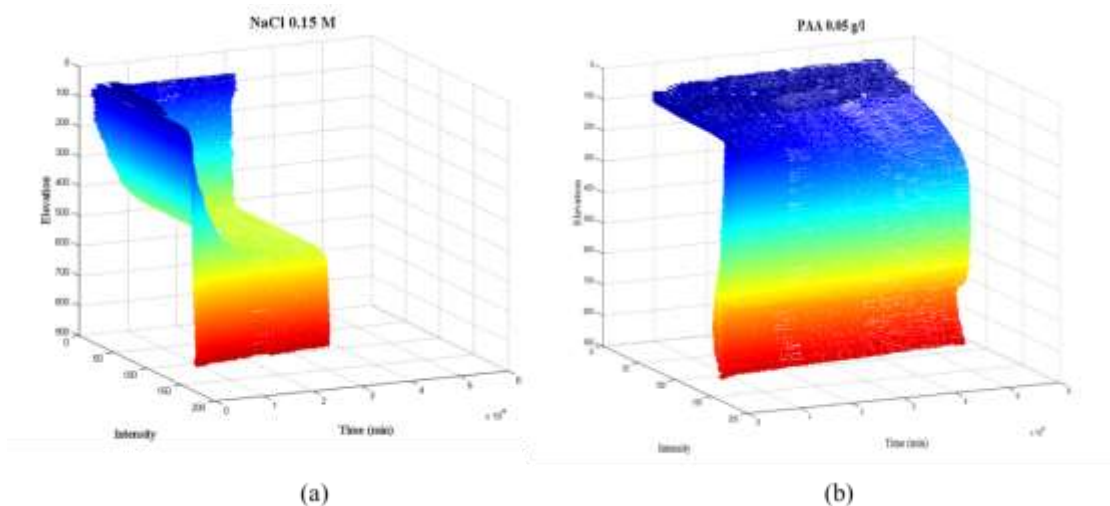
Figure 7. The intensity curves of kaolinite along the elevation as time progressed in 0.15 M NaCl and 0.05 g/l PAA solutions.
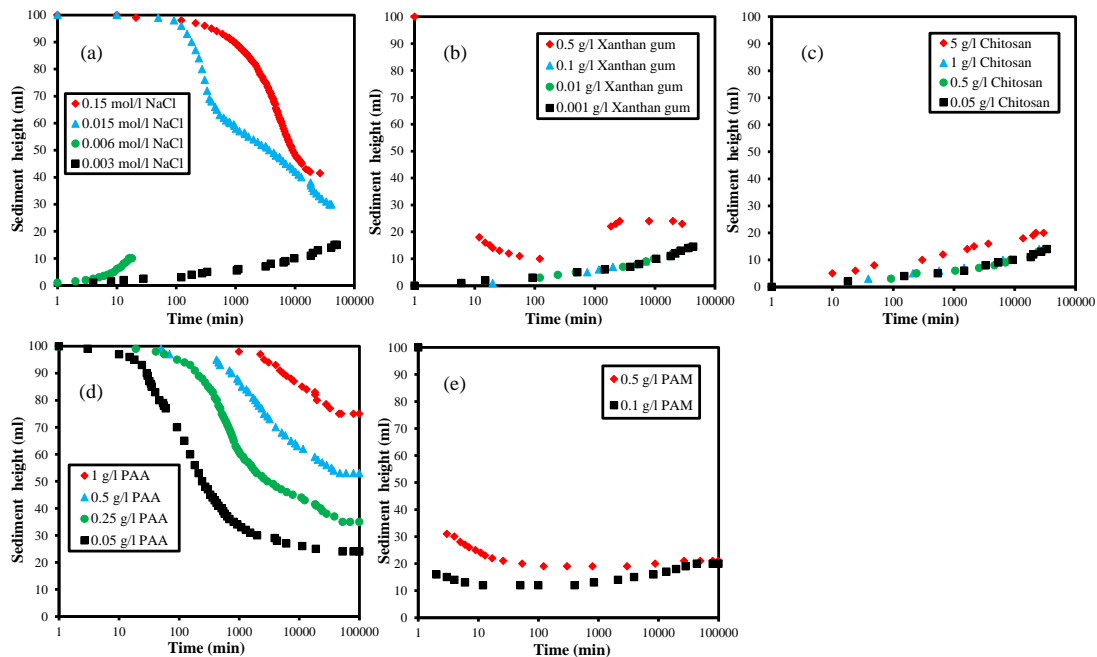
Figure 8. The sedimentation trends of kaolinite particles.
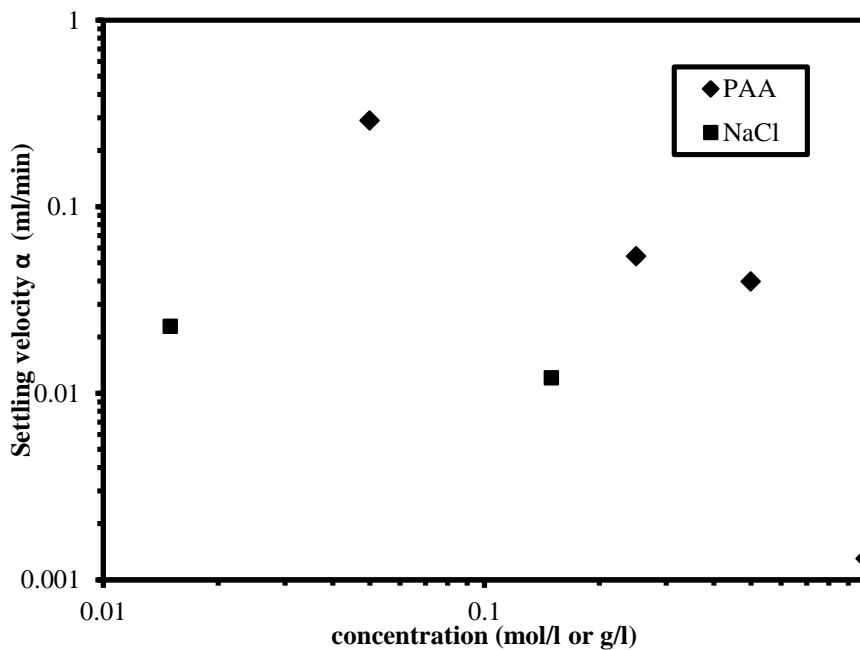
Figure 9. Settling velocities of kaolinite in different concentrations of NaCl and PAA solutions.
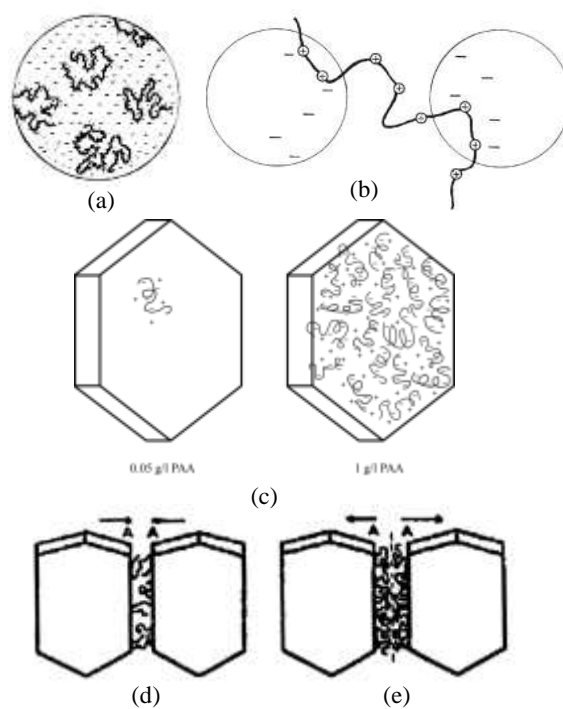
Figure 10. The schemata of interactive mode of kaolinite particles with (a) (b) chitosan (Bergaya et al., 2006), (c) PAA (this study) and (d) (e) PAM (Nabzar et al., 1988).

Table 1. Properties of Georgia kaolinite used in this study.

Source	Active Minerals International, Hunt Valley, MD, USA
Trade name	ACTI-MIN RP-2
Color	Cream[a]
Specific gravity	2.60[a]
d_{50}	0.36 μm[a]
Chemical composition	SiO_2 45.60%, Al_2O_3 38.40%, Fe_2O_3 0.88%, TiO_2 1.69%, CaO 0.05%, MgO 0.02%, K_2O 0.15%, Na_2O 0.21%, LOI 13.70%[a]
Cation exchange capacity (CEC)	CEC = 7.9 meq/100 g[b]
Isoelectric point (IEP)	Face pH ≈ 4, edge pH ≈ 7.2[c]
Point of zero charge (PZC)	4.6[d]

[a]From ACTI-MIN RP-2 data sheet, Active Minerals International (2007).
[b]From Hazen Research Inc.
[c]From Palomino and Santamarina (2005).
[d]From Stumm (1992).

Table 2. Chemical concentrations in kaolinite slurries.

Chemical Name	NaCl (mol/l)	Xanthan gum (g/l)	Chitosan (g/l)	PAA (g/l)	PAM (g/l)
	0.003	0.001	0.05	0.05	0.1
	0.006	0.01	0.5	0.5	0.5
Concentration	0.015	0.1	1	0.25	-
	0.15	0.5	5	1	-

Table 3. Molecular weight (M.W.) of polymers used in this study.

Polymer Name	Xanthan gum	Chitosan	PAA	PAM
M.W. (g/mol)	0.9×10^5-1.6×10^5	1×10^5-3×10^5	$\sim 1 \times 10^6$	$\sim 2 \times 10^5$

Table 4. Final volumes of kaolinite in PAA solutions.

PAA concentration (g/l)	0.05	0.25	0.5	1
Final volume (ml)	25 and 34	36	53	75

REFERENCES

Active Minerals International, 2007, Data Sheet for ACTI-MIN RP-2 Kaolin Clay. Hunt Valley, MD.

Ates, A., 2013. The effect of polymer-cement stabilization on the unconfined compressive strength of liquefiable soils. Int. J. Polym. Sci..

Bate, B., Burns, S.E., 2010. Effect of total organic carbon content and structure on the electrokinetic behavior of organoclay suspensions. J. Colloid Interface Sci.. 343, 58-64.

Beier, N., Wilson, W., Dunmola, A., Sego, D., 2013. Impact of flocculation-based dewatering on the shear strength of oil sands fine tailings. Can. Geotech. J.. 50, 1001-1007.

Bergaya, F., Theng, B.K.G., Lagaly, G., 2006. Handbook of Clay Science. Elsevier, Developments in Clay Science, Volume 1, pp. 192-200 (chapter 5).

Bertolino, V., Cavallaro, G., Lazzara, G., Milioto, S., Parisi, F., 2017. Biopolymer-targeted adsorption onto halloysite nanotubes in aqueous media. Langmuir, 33 (13), 3317-3323.

Cavallaro, G., Lazzara, G., Milioto, S., 2012. Exploiting the colloidal stability and solubilization ability of clay nanotubes/ionic surfactant hybrid nanomaterials. J. Phys. Chem. C 2012, 116 (41), 21932-21938.

Cavallaro, G., Lazzara, G., Milioto, S., Palmisano, G., Parisi, F., 2013. Halloysite nanotube with fluorinated lumen: Non-foaming nanocontainer for storage and controlled release of oxygen in aqueous media. J. Colloid Interface Sci.. 417 (2014), 66-71.

Chaplain, V., Janex, M.L., Lafuma, F., Graillat, C., Audebert, R., 1995. Coupling between polymer adsorption and colloidal particle aggregation. Colloid polym. Sci.. 273, 984-993.

Chen, L., Chen, D., Wu, C., 2003. A new approach for the flocculation mechanism of chitosan. J. Polym. Environ.. 11, 87-92.

Cleasby, J.L., Baumann, E.R., Dharmarajah, A.H., Sindt, G.L., 1989. Design and operation guidelines for optimization of the high-rate filtration process: plant survey results. AWWA Res. Found. Rept., Bolton and Menk, Inc., Denver, Colorado.

Crandell, D.R., Varnes, D.J., 1961. Movement of the slumgullion earthflow near Lake City, Colorado, in Short papers in the geologic and hydrologic sciences: U.S. Geological Survey Professional Paper. 424, 136-139.

Csempesz, F., Rohrsetzer, S., 1988. The effects of polymer bridging on the flocculation kinetics of colloidal dispersions. Colloids Surf.. 31, 215-230.

Das, K.K., Somasundaran, P., 2001. Ultra-low dosage flocculation of alumina using polyacrylic acid. Colloids Surf. A: Physicochem. Eng. Asp.. 182, 25-33.

Das, K.K., Somasundaran, P., 2003. Flocculation-dispersion characteristics of alumina using a wide molecular weight range of polyacrylic acids. Colloids Surf. A: Physicochem. Eng. Asp.. 223, 17-25.

Dontsova, K.M., Bigham, J.M., 2005. Anionic polysaccharide sorption by clay minerals. Soil Sci. Soc. Am. J.. 69, 1026-1035.

Feigin, R.I., Napper, D.H., 1980. Depletion stabilization and depletion flocculation. J. Colloid Interface Sci.. 75, 525-541.

Gibson, R.E., Schiffman, R.L., Cargill, K.W., 1981. The theory of one-dimensional consolidation of saturated clays. II. Finite nonlinear consolidation of thick homogeneous layers. Can. Geotech. J..18, 280-293.

Han, M., Lawler, D.F., 1992. The (relative) insignificance of G in flocculation. J. AWWA. 84, 79-91.

Hayward, J.A., Barton, J.H., 1969. Erosion by frost-heaving: a time-lapse photographic record. Soil and Water. 6, 3-5.

Hunter, D.W., 2006. The positive impact of polymers on sediment treatment and handling. Proceedings of the Western Dredging Association Twenty-sixth Technical Conference.

Hunter, R.J., Ottewill, R.H., Rowell, R.L. (Eds.), 1981. Zeta Potential in Colloid Science. Academic Press, London.

Israelachvili, J.N. (Ed.), 2011. Intermolecular and Surface Forces (third edition). Elsevier, Amsterdam.

Jones, R.H., Williams, R.R., Moore, T.K., 1978. Development and application of design and operation procedures for coagulation of dredged material slurry and containment area effluent (Technical Report -U.S. Army Engineer Waterways Experiment Station). Vicksburg, MS.

Kang, X., Bate, B., 2016. Shear Wave Velocity and Its Anisotropy of Polymer Modified High Volume Class F Fly Ash-Kaolinite Mixtures. J. Geotech. Geoenviron. Eng.. 142. 04016068.

Kim, S., Palomino, A.M., 2009. Polyacrylamide-treated kaolin: A fabric study. Appl. Clay Sci.. 45, 270-279.

Lee, L.T., Rahbari, R., Lecourtier, J., Chauveteau, G., 1991. Adsorption of polyacrylamides on the different faces of kaolinites. J. Colloid Interface Sci.. 147, 351–357.

Lentz, R.D., Shainberg, I., Sojka, R.E., Carter, D.L., 1992. Preventing irrigation furrow erosion with small application of polymers. Soil Sci. Soc. Am. J.. 56, 1926-1932.

Lentz, R.D., Sojka, R.E., 2000. Applying polymers to irrigation water: Evaluating strategies for furrow erosion control. Trans. ASAE. 43, 1561-1568.

Letterman, R.D., Pero, R.W., 1990. Contaminants in polyelectrolytes used in water treatment. J. AWWA. 82, 87-97.

Li, J., Jiao, S., Zhong, L., Pan, J., Ma, Q., 2013. Optimizing coagulation and flocculation process for kaolinite suspension with chitosan. Colloids Surf. A: Physicochem. Eng. Asp.. 428, 100-110.

Matsuoka, N., 2014. Combining time-lapse photography and multisensory data logging to monitor slope dynamics in the southern Japanese Alps. Japan Geoscience Union meeting 2014.

McFarlane, A., Bremmell, K., Addai-Mensah, J., 2006. Improved dewatering behavior of clay minerals dispersions via interfacial chemistry and particle interactions optimization. J. Colloid Interface Sci.. 293, 116-127.

Miller, R.D., Crandell, D.R., 1959. Time-lapse motion picture technique applied to the study of geologic processes. Sci. AAAS. 130, 795-796.

Mpofu, P., Mensah, A.J., Ralston, J., 2003. Investigation of the effect of polymer structure type on flocculation rheology and dewatering behavior of kaolinite dispersions. Int. J. Miner. Process.. 71, 247-268.

Nabzar, L., Carroy, A., Pefferkorn, E., 1986. Formation and properties of the kaolinite-polyacrylamide complex in aqueous media. Soil Sci.. 141, 113-119.

Nabzar, L., Pefferkorn, E., Varoqui, R., 1988. Stability of polymer-clay suspensions. The polyacrylamide-sodium kaolinite system. Colloids Surf.. 30, 345-353.

Newman, K., Tingle, J., 2004. Emulsion polymers for soil stabilization. U. S. Army Engineer Research and Development Center, 2004 FAA worldwide airport technology transfer conference, New Jersey, USA.

Nugent, R.A., Zhang, G., Gambrell, R.P.,2010. The effects of exopolymers on the erosional resistance of cohesive sediments. ICSE. 162-171.

Oprea, A., Nistor, M., Profire, L., Popa, M.I., Lupusoru, C.E., Vasile, C., 2013. Evaluation of the controlled release ability of theophylline from xanthan/chondroitin sulfate hydrogels. JBNB. 4, 123-131.

Otsubo, Y., 1994. Effect of surfactant adsorption on the polymer bridging and rheological properties of suspensions. Langmuir. 10, 1018-1022.

Palomino, A.M., Santamarina, J.C., 2005. Fabric map for kaolinite: effects of pH and ionic concentration on behavior. Clays Clay Miner.. 53, 211-223.

Pan, Z., Campbell, A., Somasundaran, P., 2001. Polyacrylic acid adsorption and conformation in concentrated alumina suspensions. Colloids Surf. A: Physicochem. Eng. Asp.. 191, 71-78.

Pefferkorn, E., 1999. Polyacrylamide at solid/liquid interfaces. J. Colloid Interface Sci.. 216, 197-220.

Pefferkorn, E., Nabzar, L., Carroy, A., 1985. Adsorption of polyacrylamide to Na kaolinite: correlation between clay structure and surface properties. J. Colloid Interface Sci.. 106, 94-103.

Pu, H., Fox, P.J., Liu, Y., 2013. Model for large strain consolidation under constant rate of strain. Int. J. Number. Anal. Met.. 37, 1574–1590.

Santamarina , J.C., Klein, K.A., Fam, M.A. (Eds.), 2001. Soils and Waves. John Wiley and Sons Ltd, New York, pp. 67-71.

Santhiya, D., Subramanian, S., Natarajan, K.A., Malghan, S.G., 1999. Surface chemical studies on the competitive adsorption of poly(acrylic acid) and poly(vinyl alcohol) onto alumina. J. Colloid Interface Sci.. 216, 143-153.

Shah, D.O., Schechter, R.S. (Eds.), 1977. Improved oil recovery by surfactant and polymer flooding. Academic Press, San Diego.

Shellberg, J. G., Brooks, A.P., Rose, C.W., 2013. Sediment production and yield from an alluvial gully in northern Queensland, Australia. Earth Surf. Process. Landforms. 38, 1765-1778.

Sorbie, K.S. (Ed.), 1991. Polymer-Improved Oil Recovery. CRC Press, Boca Taton, FL.

Stumm, W. (1992), Chemistry of the solid-water interface : processes at the mineral-water and particle-water interface in natural systems, Wiley, New York.

Stutzmann, T., Siffert, B., 1977. Contribution to the adsorption mechanism of acetamide and polyacrylamide onto clays. Clays Clay Miner.. 25, 392-406.

Theng, B.K.G. (Ed.), 1979. Formation and properties of clay polymer complexes. Elsevier, Amsterda, New York.

Theng, B.K.G. (Ed.), 2012. Formation and Properties of Clay-Polymer Complexes (second edition). Elsevier Science, Volume 4.

Thomas, D.N., Judd, S.J., Fawcett, N., 1999. Flocculation modelling: a review. Water Res.. 33, 1579-1592.

Tjipangandjara, K.F., Somasundaran, P., 1992. Effects of the conformation of polyacrylic acid on the dispersion-flocculation of alumina and kaolinite fines. Adv. Powder technol.. 3, 119-127.

Wang, C., Chen, K.Y., 1977. Laboratory study of chemical coagulation as a means of treatment for dredged material (Technical Report - U.S. Army Engineer Waterways Experiment Station). Vicksburg, MS.

Yu, J., Lei, T., Shainberg, I., Mamedov. A.I., Levy, G.J., 2003. Infiltration and erosion in soils treated with dry PAM and gypsum. Soil Sci. Soc. Am. J.. 67, 630-636.

Zaman, A., 2003. Effects of polymer bridging and electrostatics on the rheological behavior of aqueous colloidal dispersions. Part. Part. Syst. Charact.. 20, 342-350.

Zaman, A.A., Tsuchiya, R., Moudgil, B.M., 2002. Adsorption of a low-molecular-weight polyacrylic acid on silica, alumina, and kaolin. J. Colloid Interface Sci.. 256, 73-78.

Zbik, M., Smart, R.S.C., 2005. Influence of dry grinding on talc and kaolinite morphology: inhibition of nano-bubble formation and improved dispersion. Miner. Eng.. 18, 969-976.

Zhang, X.C., Miller, W.P., Nearing, M.A., Norton, L.D., 1998. Effects of surface treatment on surface sealing, runoff, and interrill erosion. Trans. ASAE. 41, 989-994.

Zhang, G., Yin, H., Lei, Z., Reed, A.H., Furukawa, Y., 2013. Effects of exopolymers on particle size distributions of suspended cohesive sediments. J. Geophys. Res.: Oceans. 118, 3473-3489.

IV. ON THE SOIL WATER CHARACTERISTIC CURVES OF POORLY-GRADED GRANULAR MATERIALS IN AQUEOUS POLYMER SOLUTIONS

Junnan Cao[1], Jung, Jongwon[2], Song, Xiaoyu[3] and Bate Bate[4]

[1]Graduate Research Assistant, Department of Civil, Architectural, and Environmental Engineering, 1401 North Pine Street, Missouri University of Science and Technology, Rolla, MO 65409. Email: jcg83@mst.edu

[2]Assistant Professor, Department of Civil and Environmental Engineering, Louisiana State University. Email: jjung@lsu.edu

[3]Assistant Professor, Department of Civil and Coastal Engineering, University of Florida. Email: xiaoyu.song@essie.ufl.edu

[4]Research Professor, Institute of Geotechnical Engineering, College of Civil Engineering and Architecture, Zhejiang University, 866 Yuhangtang Road, Hangzhou, China 310058. Email: batebate@zju.edu.cn; Formerly, Assistant Professor, Department of Civil, Architectural, and Environmental Engineering, 1401 North Pine Street, Missouri University of Science and Technology, Rolla, MO 65409

ABSTRACT

Tempe cell with a self-developed horizontal hanging column attachment was used to measure the soil water characteristic curves (SWCCs) of granular materials initially saturated with either water or polymer solutions. For SWCCs of six poorly-graded granular materials with d50 ranging from 0.04 mm to 0.7 mm in water, it was found that (1) as grain size decreases, air entry value (AEV) increases, and matric suction (ψ) for the funicular and pendular regimes increases, and that (2) steep desaturation curves over narrow ψ range in the funicular regime were observed. Air entry values obtained from the fitting parameter $1/\alpha$ in van Genuchten SWCC equation fall in the boundaries calculated from the pore throat sizes in both simple cubic and face-centered cubic packings. A

toroidal meniscus water model, which incorporates the measured surface tension and contact angle values between aqueous solutions and solid surfaces, was proposed for the SWCC in pendular regime and was compared to well-received numerical methods. This toroid model successfully depicts SWCC of poorly-graded granular materials in water. However, SWCCs predicted by this toroid model underestimate the degree of saturation in the pendular regime for Ottawa 20-30 sands in polymer solutions. Herschel-Bulkey fluid, which is a type of non-Newtonian fluids, is postulated to increase the ψ needed to drain the polymer solution due to the nonzero shear stress intercept. In addition, it is also postulated by scanning electron microscopy and optical confocal imaging results that the rough surfaces of Ottawa 20-30 sand, which have many micron-sized "kinks", together with the possible chemical attractions, helps retain the polymer solutions on the solid surfaces, or water film.

KEYWORDS: soil-water characteristic curves, polymer solutions, sand, toroid model, meniscus, poorly-graded.

1. INTRODUCTION

Polymeric solutions retention and transporting in porous media are commonly seen phenomena found in many engineering fields, such as ground improvement (Cabalar and Canakci 2005; Kang and Bate 2016; Martin et al. 1996), soil contaminant containment barriers (Di Emidio et al. 2015; Javadi et al. 2017; Scalia et al. 2014; Zhao et al. 2017), bioremediation of geomaterials (Ivanov and Chu 2008; Yeom et al. 2010), and chemically enhanced oil recovery (EOR) (Cao et al. 2016; Jung et al. 2016; Mollaei et al.

2011). Most of current work on polymer modified geomaterials focused on evaluating their swelling/shrinkage, large strain strength, small strain stiffness, hydraulic conductivity and erosion resistance properties in either saturated or compacted condition. Only a few studies controlled the unsaturation conditions, such as matric suction (Cao et al. 2016; Jung and Jang 2016; Puppala et al. 2006). In the field condition, however, soils are not always saturated due to seasonal groundwater level change, precipitation, and evaporation, or in the applications like soil vapor sparging, CO_2 sequestration, shale gas production, imbibition, contaminant transport and petroleum leakage onto soil particle surface, and projects involving methane hydrate (Dai et al. 2012; Espinoza and Santamarina 2010). Due to the variability of polymeric solutions, the viscosity, surface tension and the contact angle between liquid and porous media varies. This will lead to highly variable flow behaviors and liquid retention capability of the hosting porous media. Once desaturation occurs, the mechanical properties of geomaterials could change drastically (Bate and Zhang 2013; Fredlund et al. 2012; Lu 2016; Lu et al. 2009; Lu et al. 2007; Mitarai and Nori 2006).

On the other hand, granular materials have been widely used in a variety of engineering applications, such as liquefaction resistance enhancement in sandy materials by biomediation (Montoya et al. 2013) due to the compatibility between the pore throat size and the bacteria size (Mitchell and Santamarina 2005), proppants (ceramic beads or sands) to prop open the geophysical formation for the injection of polymers and surfactants in chemical EOR, and the granular materials for state-of-the-art porous pavement materials. Therefore, the characterization of geomaterials under unsaturated condition is warranted.

Soil-water characteristic curve (SWCC) exhibits the relationship between matric suction (y) and volumetric water content of a soil (Fredlund and Rahardjo 1993; Lu and Likos 2004), where matric suction is the difference between air pressure (u_a) and water pressure (u_w), or $y = u_a - u_w$. It is worth noting that osmotic suction, another component of total suction, relates to the chemical properties of bulk solution and is usually negligible for diluted bulk solutions and coarse-grained geomaterials. Other soil properties, such as hydraulic conductivity and shear strength can be estimated from SWCC (Fredlund et al. 1978; Fredlund et al. 1994; Lu et al. 2009). SWCC of water adsorption or desorption (wetting or drying) has been documented previously. However, SWCC of geomaterials in polymer solutions was rarely studied (Jung and Jang 2016; Zhao 2014). Many SWCC equations were proposed as summarized in Leong and Rahardjo (1997) and Ba-Te (2004). Particularly, van Genuchten SWCC equation (1980) is expressed as

$$S = S_r + (\frac{1}{1+(ay)^n})^m \tag{1}$$

where S is degree of saturation, subscription "r" means residual, a relates to the inverse of the air entry value (AEV = $1/\alpha$); n relates to the pore size distribution of the soil, with poorly-graded soils yield high n values; m relates to the asymmetry of the model.

A typical SWCC consists of four states or regimes, namely saturation, capillary, funicular and pendular (Fig. 1) (Mitarai and Nori 2006). A saturated soil (saturation regime) transits into capillarity regime when the matric suction increases from zero, where only little water was expelled due to water meniscus deformation at the soil surface (Fig. 1). When matric suction exceeds the air entry value (AEV, a matric suction

value corresponding to the beginning of air entering the pore spaces), soil reaches the funicular regime where the major water desaturation occurs. Surpassing the residual matric suction (ψ_r) or snap-off suction (Likos and Jaafar 2013; Or and Tuller 1999; Tokunaga et al. 2013), pendular regime is reached where water phase resides primarily in the toroidal meniscus and on the solid surface (Fig. 1). Besides, at extreme high matric suction (approaching 1000 MPa), only surface attached water (thickness on the order of a few nanometers) exists (Likos and Jaafar 2013). AEV and ψ_r can be determined graphically are shown in Fig. 1.

Toroid model, which assuming the water resides in a toroid ring near the contacts between particles in the pendular regime (Fig. 2b), is the basic model used in many studies (Likos and Jaafar 2013; Molenkamp and Nazemi 2003; Scheel et al. 2008). The geometrical configuration of the toroid ring depends on the surface tension (T_s) and contact angle (β) as dictated by Laplace equation:

$$y = \frac{2 \times T_s \times \cos b}{\Gamma \times g \times r}$$

(2)

where ρ, g and r are density of the pore fluid, gravity constant and pore throat radius, respectively. Surface tension and contact angle of the bulk fluid are influenced by the solute. Therefore, toroidal water content should be different for poorly-graded granular materials in different polymer solutions.

Most laboratory techniques of measuring SWCC of a soil are based on high air entry ceramic disk with applied matric suction ranges of 0 - 1500 kPa, such as Tempe cell (0 - 100 kPa), pressure plate (0 - 1500 kPa), Fredlund SWCC cell (0 - 1500 MPa), Wille pressure plate cell and Barcelona cell (Fredlund et al. 2012). In a conventional ceramic

disk-based SWCC device, SWCC measurement of coarse-grained materials is limited by their low air entry value (usually < 1 kPa) and by the accuracy of the pressure regulators as satisfactory matric suction reading usually starts from 5 kPa (Fredlund et al. 2012). Hanging column, in which the water level is lowered below the base of the soil sample to apply low water pressure, is used for creating accurate low matric suction values (< 5 kPa) (Fredlund et al. 2012; ASTM D6836). A simplified hanging column setup was also used by Li et al. (2009).

This study aims at three objectives: (1) Develop a hanging column attachment to use in conjunction with Tempe cell to investigate the soil-water characteristic curve of poorly graded sands that were initially immersed with different polymer solutions. (2) Derive a toroidal meniscus water equation, which incorporates the measured surface tension and contact angle between aqueous solution and solid surface, to model SWCC in pendular regime. (3) Identify other forms of water retention mechanisms with scanning electron microscopy and optical confocal images.

2. MATERIALS

Ottawa 20-30 and 50-70 sands (US Silica, Frederick, MD, USA) were used as received. Their specific gravity of both sands is 2.65. Ottawa 20-30 sand is composed of 99.8% SiO_2, 0.06% Al_2O_3, 0.020% Fe_2O_3, 0.01% TiO_2, other trace amount ($< 0.01\%$) of metal oxides, and 0.1% loss on ignition (US Silica datasheet). Ottawa 50-70 sand is composed of 99.7% SiO_2, 0.06% Al_2O_3, 0.020% Fe_2O_3, 0.01% TiO_2, other trace amount ($< 0.01\%$) of metal oxides, and 0.1% loss on ignition (US Silica datasheet). Their grain

size distribution curves were shown in Fig. 3. The d_{50} values for Ottawa 20-30 and 50-70 sands are 0.7 mm and 0.23 mm, respectively.

Polyethylene oxide (PEO), polyacrylamine (PAM), polyacrylic acid (PAA), xanthan gum and chitosan (Fisher Scientific) were used as received. Polymer solutions were made by dissolving the prescribed mass of polymer powders into a 1000 ml volumetric flask (Table 1), and then the mixtures were mechanically stirred (Isotemp Stirring Hotplate 4 ×4 in. model, Fisher Scientific). Some polymers with high molecular weight, such as PAM and xanthan gum, took at least 24 hours and ultrasonic bath (Branson Ultrasonic Cleaner, Model 8800, Branson Ultrasonics Corp., Danbury, CT) to completely dissolve.

3. EXPERIMENTAL METHODS

The surface tension of polymer solutions was measured by a dynamic surface tensiometer (SensaDyne QC6000, SensaDyne Instrument Division, Mesa, AZ, USA). Sessile drop method with a Rame-hart goniometer and an optical system was used to capture the contact angle of a high purity polymer drop on a quartz slide surface. A quartz slide (containing 99.8% SiO_2) (Fisher Scientific), containing almost identical mineral composition as that of both sands used in this study, was used.

Scanning electron microscopy (SEM) test was carried out for Ottawa 20-30 sand by the SEM S-4700 (Hitachi). Sand particles were coated with gold powder using a sputter-coater (Hitachi E-1030) before testing. The surface roughness of Ottawa 20-30 sand was measured with an optical confocal microscope (KH-8700, Hirox-USA, inc.,

Hackensack, NJ) and a middle range (50x-400x) objective lens. Three-dimensional confocal images were reconstructed by KH-8700 3DViewer software.

Tempe cell (Soilmoisture, Santa Barbara, CA, USA) with ceramic disk (130 kPa air entry pressure) was used with a self-developed hanging horizontal column attachment to measure the soil water characteristic curve of sands (Fig. 4). Loose sand specimens for SWCC tests were prepared in a stainless steel ring (2.5 inch $\times$ 0.5 inch, inner diameter $\times$ height) by air pluviation method with identical free fall height (about 2 cm), pouring speed (hand scoop) and funnel opening (Bate and Zhang 2013) to maintain the same initial void ratios. Polymer solutions were added slowly from the top of the specimen until Tempe cell was filled up to the top of the specimen. Residual solution on top of the specimen was blotted with lint-free tissues.

The steps of matric suctions during desaturation are as follows: 0.05, 0.1, 1, 2, 4, 6.89, 12, 25, 50, and 100 kPa. The outflow volume reading from the horizontal tube over time was monitored to identify the cessation of the outflow under each matric suction step. Small matric suction ($\pm$ 4 kPa) was applied by lowering the elevation of a horizontal tube below the bottom of the sand specimen (Fig. 4). When the applied matric suction exceeds 5 kPa, air pressure (u_a) was applied through the air regulator to the top of the specimen while maintaining the water pressure below the ceramic disk atmospheric ($u_w = 0$).

The height change of the specimen was at most 0.5 mm (2.5% by volume) during the tests. This height change was similar to those in the SWCC tests done on similar sands (Gitirana and Fredlund 2004; Lins et al. 2009; Pham 2005), which were deemed negligible to influence total specimen volume. Therefore the total volume was considered

constant during all SWCC tests in this study. It is noted, however, that in rigorous numerical study the SWCC also depends on soil deformation (strain) and temperature (Borja et al. 2013; Song 2017; Song and Borja 2014; Song and Borja 2014; Song et al. 2017; Song et al. 2017). On the other hand, the evaporation of water through the open end of the horizontal tube was calibrated by taking readings of the horizontal tube every 2-3 hours, up to 20 hours. Given the limited temperature variations (22 - 24 ℃) in the laboratory, the evaporation rate was assumed to be constant, and was measured and corrected.

4. RESULTS

Surface tension, contact angle, and viscosity values of different polymer solutions were shown in Table 1 and Fig. 5, respectively. The contact angle ranges from 21.3 ° to 41.3 °, and surface tension from 61.8 to 80.5 dyne/cm, respectively. Noticeable differences were observed when comparing with water (contact angle of 38.1 °, surface tension of 73.1 dyne/cm).

The majority of the particles of both Ottawa 20-30 and 50-70 sands is round or sub-round as revealed by SEM images (Figs. 6a and 6c). Small "kinks," i.e. the micron-sized dents or defects on the sand surfaces, were observed for Ottawa 20-30 sand by high magnification SEM images (Fig. 6c). Such kinks on Ottawa 20-30 sand were also observed from the 3D reconstructed confocal image (Fig. 7a) or the meshed contour of the 3D image (Fig. 7b). Polymers, such as xanthan gum, were found to adhere to the surface of Ottawa 20-30 sand (Fig. 6d).

SWCCs for Ottawa 20-30 and 50-70 sands in water are shown in Fig. 8. The corresponding fitting parameters with van Genuchten model were listed in Table 2. SWCCs for Ottawa 20-30 sand in polymer solutions are shown in Figs. 9 and 10. These measured SWCC results will be compared with other poorly-graded granular materials, and discussed in details in Discussion.

5. DISCUSSION

5.1. SWCC OF GRANULAR MATERIALS IN WATER

The grain size distribution curves and the drying soil-water characteristic curves of Ottawa 20-30 and 50-70 sands were compared with those of other uniformly sized (poorly-graded) glass beads, including 0.25-0.60 mm glass bead (d_{50} = 0.6 mm) used in Manahiloh and Meehan (2015), 0.25-0.30 mm (d_{50} = 0.25 mm), 0.075-0.090 mm (d_{50} = 0.09 mm), and 0.032-0.045 mm (d_{50} = 0.04 mm) glass beads used in Jaafar and Likos (2011) (Figs. 3 and 8). Three independently fitted parameters, namely α (inverse of air entry value), n and m, in van Genuchten SWCC equation for all six granular materials were tabulated in Table 2. It was observed that: (1) as grain size (characterized by d_{50}) decreases, air entry value (AEV) increases, and matric suction for the funicular and pendular regimes increases; (2) all six SWCCs have steep desaturation curves over narrow ψ range in the funicular regime, i.e., AEV and the matric suction at the start of pendular regime are very close, (< 5 kPa). The air entry value for simple particle packings, such as simple cubic (SC) and face-centered cubic (FCC) packing, can be calculated by the inner circle diameter (d_{in}) along adjacent particles in a same plane (referred to as the pore throat size in some articles) by Laplace equation:

$$AEV = \frac{2T_s \cos \beta}{\left(\frac{d_{in}}{2}\right)}$$

(3)

The upper and lower bounds of the AEV predicted by Eq. 3 encompass those from   parameters with van Genuchten equation (Table 2), suggesting the agreement between the two AEV estimation approaches. The AEV calculated by this method is also termed "snap-off" pressure (Likos and Jaafar 2013; Or and Tuller 1999). It should be noted, however, that the AEV obtained using above method is only estimation, as the contact angle (β) between water or aqueous solution is assumed to be zero. Physically, if β is nonzero, the pore throat size (d_{in}) becomes smaller, and AEV higher. This difference is often neglected in practice for simplicity. On the other hand, water volume in pendular regime has two major components, namely meniscus water and water film (Or and Tuller 1999). Meniscus water referred to the water adjacent to particle contacts, and can be calculated by toroidal model; water film can be induced by surface condensation, chemical interactions (Or and Tuller 1999), or surface roughness (Molenkamp and Nazemi 2003). For coarse-grained materials in water, water meniscus usually is the major contributor; for fine-grained materials or for materials in polymer solutions, however, water film could also play a major role. In the subsequent sections, toroid model will first be proposed and evaluated, followed by discussions on the importance of water film and its possible inducing mechanisms.

5.2. TOROIDAL MENISCUS WATER MODEL

Only meniscus water is considered in this toroid model. The following assumptions were made: (1) all particles are spheres of identical diameter; (2) simple

cubic (SC) packing and face-centered cubic (FCC) packing, the theoretical loosest and densest packing states, are assumed to correspond to the upper and lower bounds of all the measured SWCCs; (3) toroid water exists only at particle contacts. Although this is true for both SC and FCC packings, toroid water could also exist in-between two particles with a small gap (Lian et al. 1993) in practice. The geometry of meniscus water at a contact between two particles is shown in Fig. 2a.

(1) Calculation of the fill angle (g)

The free body diagram with respect to the meniscus is drawn in Fig. 2b, and the equilibrium equation in the radial direction is

$$T\cos(\beta+\gamma)2\pi R\sin\gamma\times2 = (u_a - u_w)2\pi R\sin\gamma\cdot Z\times2 \tag{4}$$

where $Z = R(1 - \cos g)$. The radius of toroidal meniscus R' can be related to Z (Fig. 2a) as

$$R' = \frac{Z}{\sin(90^o - b - g)} = \frac{R(1 - \cos g)}{\cos(b + g)} \tag{5}$$

Insert Eq. 5 into Eq. 4 yields

$$\cos(b + g) = \frac{(u_a - u_w)R(1 - \cos g)}{T} \tag{6}$$

Rearranging yields

$$\cos g\left[\frac{(u_a - u_w)R}{T} + \cos b\right] - \sin g\sin b = \frac{(u_a - u_w)R}{T} \tag{7}$$

Consider a triangle in Fig. 2c, Eq. 7 becomes

$$\cos(g + a) = \frac{(u_a - u_w)R}{T}\frac{1}{\sqrt{\left[\frac{(u_a - u_w)R}{T} + \cos b\right]^2 + (\sin b)^2}} \tag{8}$$

where

$$a = \tan^{-1}\left[\dfrac{\sin b}{\dfrac{(u_a - u_w)R}{T} + \cos b}\right] \tag{9}$$

Solve for g yields

$$g = \cos^{-1}\left[\dfrac{(u_a - u_w)R}{T\sqrt{\left[\dfrac{(u_a - u_w)R}{T} + \cos b\right]^2 + (\sin b)^2}}\right] - a \tag{10}$$

From the physical meaning of fill angle (g) we have $0 < g \leq 45^o$ for simple cubic

packing, and $0 < g \leq 30^o$ for face-centered packing. Thus, a unique solution can be

obtained from Eq. 10.

(2) Calculation of the toroidal fluid volume

The volume of the toroidal fluid at a contact point, V_{toroid} (Fig. 2b) can be

calculated by

$$V_{toroid} = 2\left(V_{cylinder} - V_{cap} - V_{air}\right) \tag{11}$$

where $V_{cylinder}$ is the volume of all the shaded areas; V_{cap} and V_{air} are shown in Fig. 2b. Eq.

11 can be re-written as

$$V_{toroid} = 2\left\{2\rho R \sin g \times Z - \dfrac{p}{6}Z\left[3(R\sin g)^2 + Z^2\right] - V_{air}\right\} \tag{12}$$

The only unknown, V_{air}, in Eq. 12 can be calculated by integrating its shaded area as

follows. The differential form of a unit V_{air} volume is

$$dV_{air} = r \times dq \times dr \times dz \tag{13}$$

and the integration form of Eq. 13 is

$$V_{air} = \int_0^{2\pi} \int_0^z \int_{r_1}^{r_2} r \times dq \times dr \times dz \tag{14}$$

The geometry in Figs. 2a and 2d yields $a = R\sin g + R'\cos\left(90^\circ - g - b\right), z = \sqrt{R'^2 - \left(a - r\right)^2}$,

$r_1 = a - R'$, and $r_2 = R\sin g$, then $dz = \dfrac{1}{2}\dfrac{1}{\sqrt{R'^2 - \left(a - r\right)^2}}\left[2\left(a - r\right)\right]dr$. Considering the upper

and lower limits of the three coordinate variables: $0 \le q \le 2\pi$, $r_1 \le r \le r_2$, and

$0 \le z \le \sqrt{R'^2 - \left(a - r\right)^2}$, Eq. 14 becomes

$$V_{air} = 2\pi \int_{r_1}^{r_2} r\sqrt{R'^2 - \left(r - a\right)^2}\, dr \tag{15}$$

Rearranging Eq. 15 yields

$$V_{air} = \frac{2\pi}{3} \int_{r_1}^{r_2} 3\left(r - a\right)\sqrt{R'^2 - \left(r - a\right)^2}\, dr + 2\pi a \int_{r_1}^{r_2} \sqrt{R'^2 - \left(r - a\right)^2}\, dr \tag{16}$$

In Eq. 16, the first component can be integrated directly, while the second component can be solved using trigonometry function as shown in Fig. 2e. Let $\left(r - a\right) = R'\sin\left(t\right)$, and consider the boundaries $\left(r_1 - a\right) \le \left(r - a\right) \le \left(r_2 - a\right)$ and $-\dfrac{\pi}{2} \le t \le -\left(g + b\right)$, we have

$$V_{air} = -\frac{2\pi}{3}\left[R'^2 - \left(r_2 - a\right)^2\right]^{\frac{3}{2}} + 2\pi a R'^2 \frac{1}{2}\int_{-\frac{\pi}{2}}^{-\left(g+b\right)}\left(1 + \cos 2t\right) dt \tag{17}$$

then

$$V_{air} = -\frac{2\pi}{3}\left[R'^2 - \left(r_2 - a\right)^2\right]^{\frac{3}{2}} + \pi a R'^2\left[\sin^{-1}\left(\frac{r_2 - a}{R'}\right) + \frac{\pi}{2} + \frac{\left(r_2 - a\right)}{R'^2}\sqrt{R'^2 - \left(r_2 - a\right)^2}\right] \tag{18}$$

or

$$V_{air} = -\frac{2\rho}{3}\left[R(1-\cos g)\right]^{\frac{3}{2}} + \rho a\left[\frac{R(1-\cos g)}{\cos(b+g)}\right]^2\left[\frac{\rho}{2} - (b+g) - \sin(b+g)\cos(b+g)\right] \quad (19)$$

Substituting Eq. 18 or Eq. 19 into Eq. 12 gives the toroidal fluid volume (V_{toroid}) of a spherical particle contact under a given matric suction (or fill angle).

To test the validity of above toroid model, two numerical methods proposed in Lian et al. (1993) and Lu and Likos (2004), both of which are well-received (Lechman and Lu 2008; Lechman et al. 2006; Molenkamp and Nazemi 2003), were used with the same contact angles measured in this study as references. The decreasing trends by the toroid model in this study are similar and the magnitudes of water content are on the same order as the two numerical methods in the literature. The numerical methods by both Lian et al. (1993) and Lu and Likos (2004) give similar water content values, which are lower than the toroid model in this study does. This is postulated to due to the fact that surface tension along radial direction, which was not depicted in a two-dimensional model (as in this study, Fig. 2) but considered in the methods in Lian et al. (1993) and Lu and Likos (2004), also contributed to the reduction of water content. Nevertheless, the calculated upper and lower bounds of the SWCCs by the toroid model in this study encompass the measured ones very well for all six uniformly-sized particulate materials with large range of particle sizes (d_{50} from 0.04 to 0.7 mm) (Fig. 11). This suggests that meniscus water (toroidal water) is the major contributing factor for granular particles initially submerged in water. However, as the particle size decreases (d_{50} from 0.7mm to 0.04mm), the meniscus prediction yields less water at higher suction (> 50 kPa). This observation suggests water film, not captured by the meniscus model, gradually plays an important role at finer granular materials.

5.3. SWCC WITH POLYMER

The predicted degree of saturation at matric suction higher than 2-6 kPa by toroidal model was lower than the measured values for Ottawa 20-30 sand initially saturated in PAA, xanthan and PEO solutions (Figs. 9 and 10). This suggests that in addition to the meniscus water predicted by the toroid model, aqueous solution in other forms, e.g. water film, induced by other mechanisms was present.

(1) Herschel-Bulkley fluid: minimal shear resistance

PAA solution shows the behavior of Herschel-Bulkley fluid, a non-Newtonian fluid, (Fig. 5a) with the best-fitted viscosity equation as:

$$\tau = 0.144 + 0.155 \left(\frac{dv}{dz} \right)^{0.855} \tag{20}$$

where τ is the shear stress, dv/dz the velocity gradient normal to the flow direction (z), and 0.144 kPa the minimal shear resistance to mobilize the fluid. In order to initiate the flow of PAA solution in the pendular regime (desaturation), pressure difference (ψ) should be sufficient to generate the maximum shear stress (at the solid-liquid interface) that overcomes the minimal shear resistance of PAA solution (0.144 kPa). This ψ requirement could be very high for PAA solutions residing in spaces with small pore throat size, as the degree of saturation remains at 0.1 even though ψ reaches 100 kPa (Fig. 10a). As a result, higher degree of saturation (more liquid) was observed in pendular regime for SWCC of sand in a PAA solution than in water (Fig. 10a).

(2) Water retention due to surface roughness

Although not a Herschel-Bulkley fluid, xanthan gum solution exhibits shear-thinning behavior as expressed in Eq. 21:

$$\tau = 0.147\left(\frac{dv}{dz}\right)^{0.667} \qquad (21)$$

An even higher residual degree of saturation was observed than that of the SWCC curve in PAA solution (Fig. 10). SEM and optical confocal imaging investigations on the surface roughness of the Ottawa 20-30 sand revealed that the sand surfaces contains small kinks (Figs. 6b & 7b), which might trap xanthan fluids, and therefore retain a portion of aqueous solution on the particle surface, or, water film.

Apart from above mechanisms, the thickness of surface water film depends on van der Waals force between the solid surface and fluid (Cho and Santamarina 2001). Xanthan gum solution is sticky and is widely used as food thickening agent. The chemical interaction, possibly van der Waals force, between the polymer solutions and sand surfaces might also contribute to the water retention (Gee and Healy 1990; Götze and Sonntag 1988). The SEM image also revealed that xanthan gum stuck at the sand surfaces (Fig. 6d). Above observations lead to the postulation that due to the adhesiveness (possibly originated from van der Waals force), higher matric suction is needed to desaturate the xanthan gum in Ottawa 20-30 sand. Similarly, PEO also showed residual degree of saturation, which might also be due to the adhesion to the rough sand surfaces.

PAM and chitosan solutions have similar surface tension, contact angle and viscosity as water. But both showed high degree of saturation than water at matric suction less than 25 kPa. The adhesion (due to van der Waals interaction and rough surface) might contribute to the water retention. At matric suction of 50 kPa, the majority of both solutions were desaturated, indicating the weak effects of the adhesion of chitosan and

PAM solutions. High degree of saturation at similar matric suction range (0-50 kPa) was also reported for F-75 sand (d_{50} = 0.3 mm) in PAM solutions by Jung and Jang (2016).

To sum up, beside surface tension and contact angle, which are the two major parameters for SWCC of water saturated uniformly-sized particulate media, viscosity, the kinks on the rough surface, and the apparent adhesive force could also play an important role in SWCC of polymer solution saturated uniformly-sized particulate media.

6. CONCLUSIONS

In this study, Tempe cell with self-developed horizontal hanging column attachment was used to determine the soil water characteristic curves of uniformly sized sands initially saturated with water and polymer solutions. Air entry values predicted by the pore throat size are similar to those from α parameters with van Genuchten equation. A toroidal meniscus water model, incorporating the measured surface tension and contact angle values, was proposed to calculate the volume of water in pendular regime and was compared to well-received numerical methods. The calculated upper and lower bounds by this toroidal water model encompassed all six measured SWCCs of uniformly-sized granular materials with a wide d_{50} range (0.7 - 0.04 mm) in water, which suggests meniscus water is dominant in this case.

For the case of water in pendular regime at SWCCs of poorly graded Ottawa 20-30 sand initially saturated with polymer solutions, the proposed toroidal model predicted lower water contents than the measured ones. Other form of aqueous solution, such as water film surrounding the particle surfaces, could be present. Through viscosity measurement, SEM, and optical confocal imaging investigations, it was concluded that

Herschel-Bulkley fluid, surface roughness, and the possible chemical interactions (such as van der Waals interaction between the polymer solution and solid surface) could contribute to retention of aqueous solution.

ACKNOWLEDGEMENTS

Figure 1. A typical soil water characteristic curve for a granular material (revised from Fredlund and Rahardjo 1993). Three regimes of water content shown: capillary state, funicular state and pendular state (inset: modified from Fredlund et al. 2012).
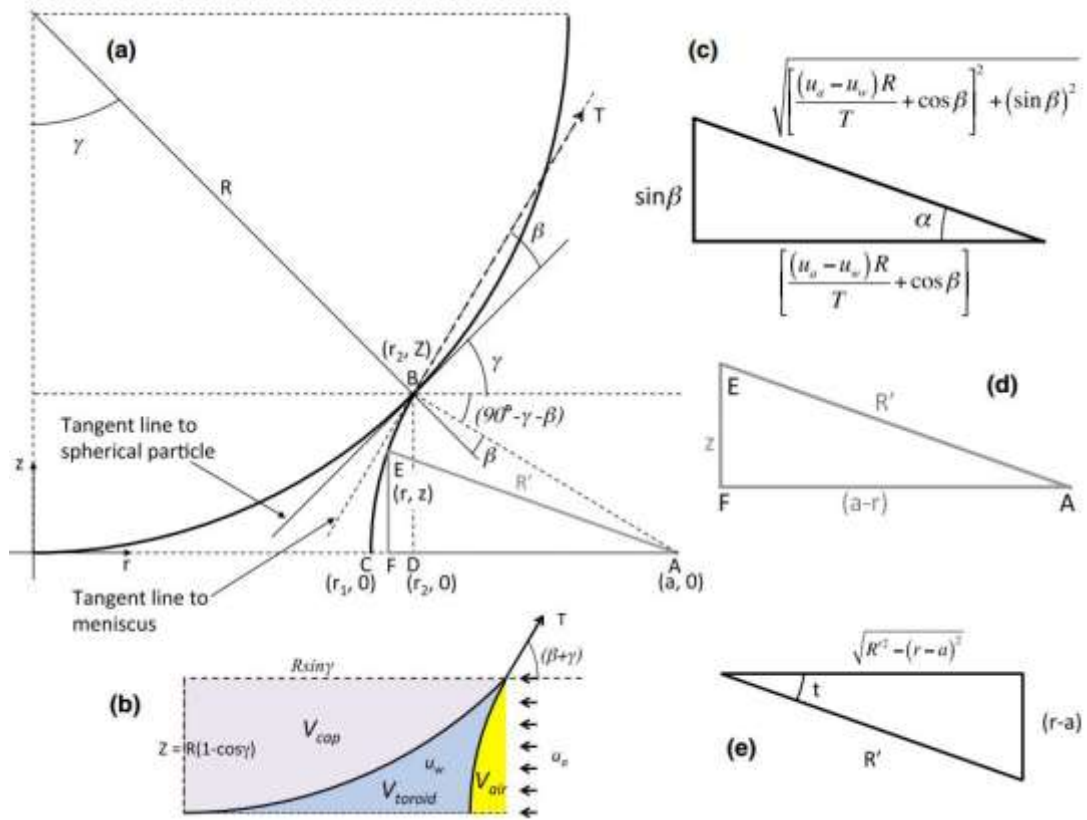
Figure 2. (a) Geometry of toroidal fluid near a sphere contact, (b) free body diagram w.r.t. meniscus, and (c), (d), (e) triangles used for integration.

Figure 3. Grain size distributions of Ottawa 20-30 and 50-70 sands, and four uniformly sized glass beads.
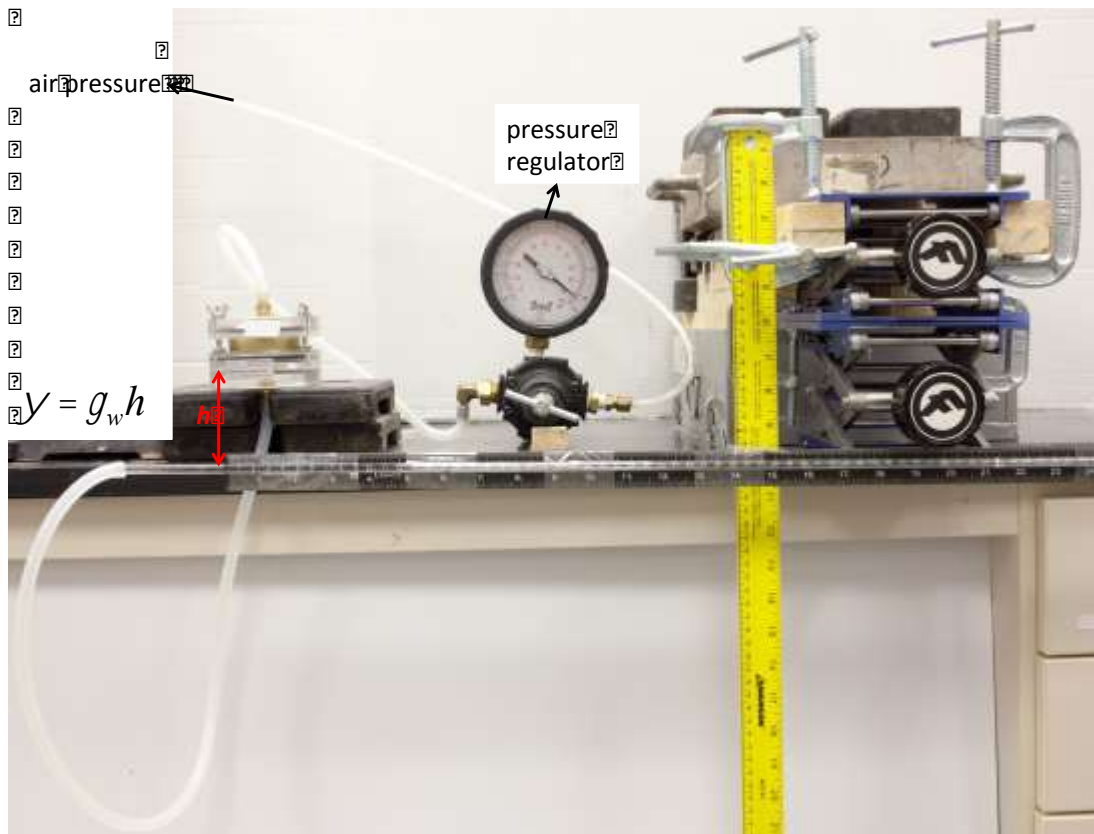
Figure 4. Schematic setup of low suction device for SWCC measurement.
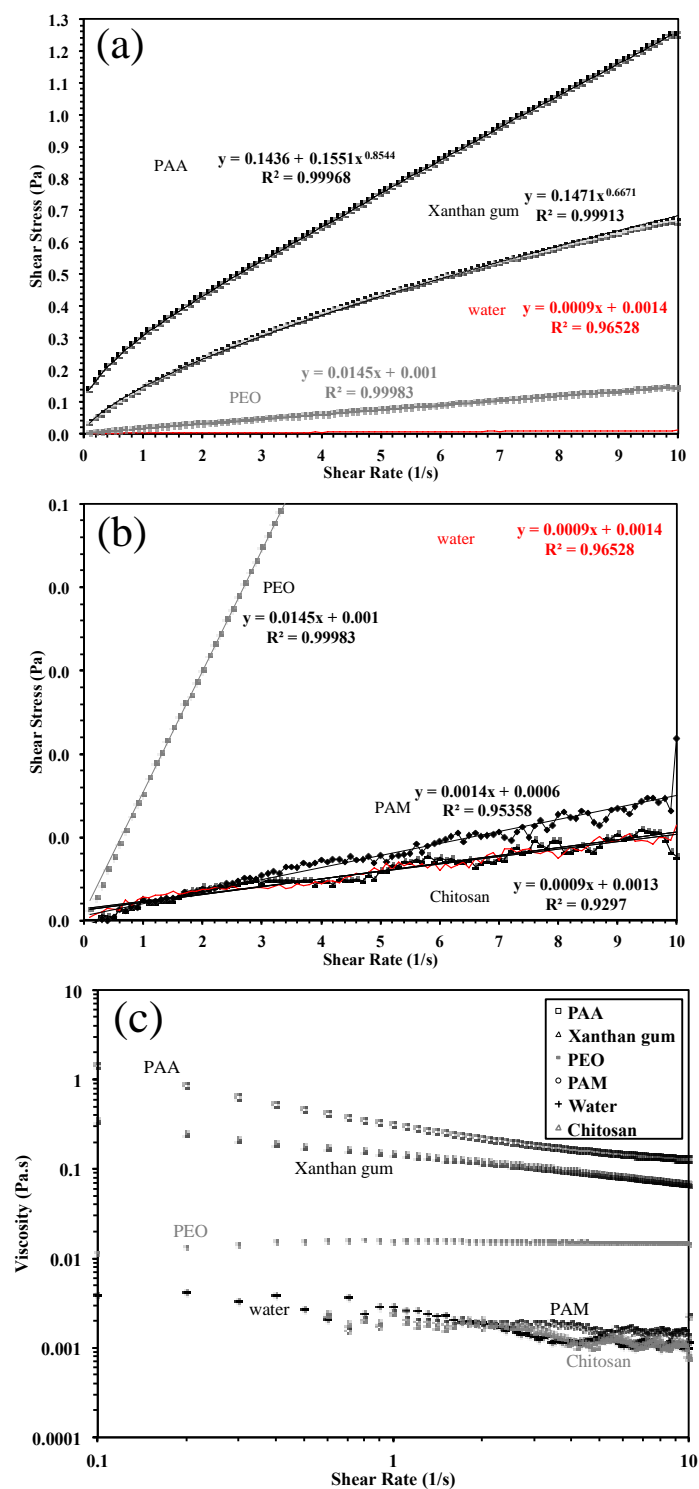
Figure 5. (a) and (b) shear stress versus shear rate curves, (c) viscosity versus shear rate curves.
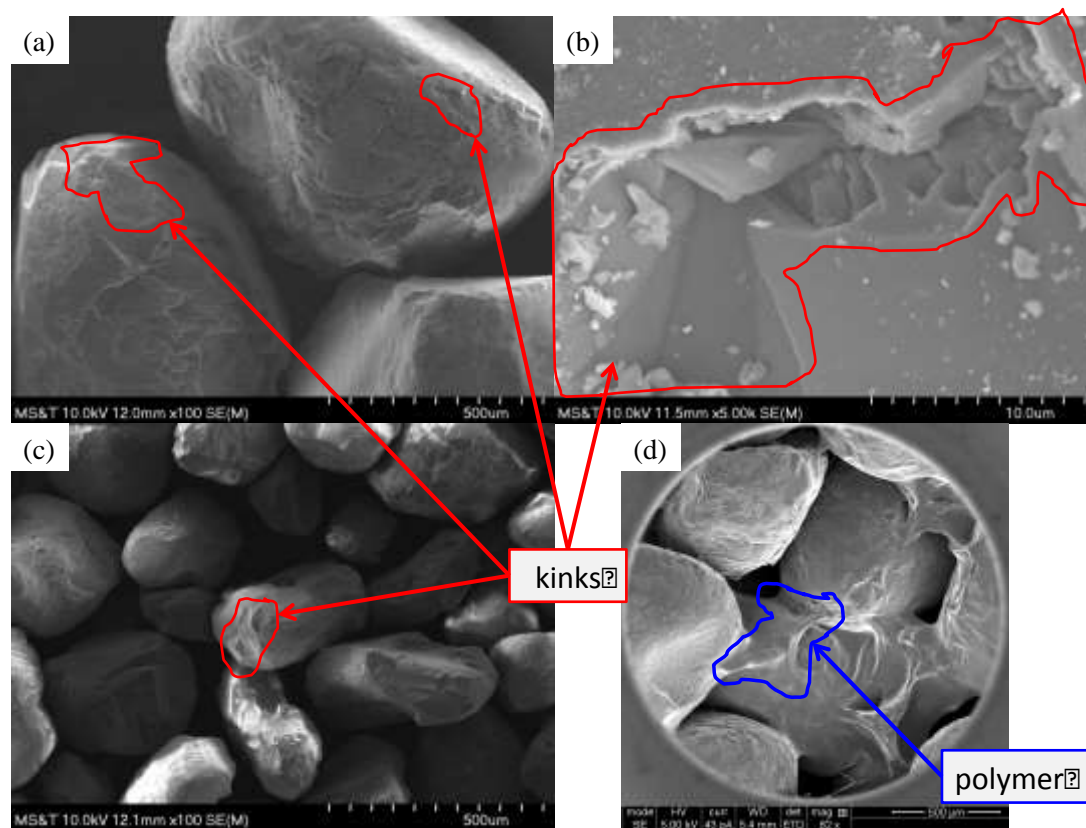
Figure 6. SEM images of (a) and (b) Ottawa 20-30 sand, (c) Ottawa 50-70 sand, and (d) Ottawa 20-30 sand in xanthan gum.
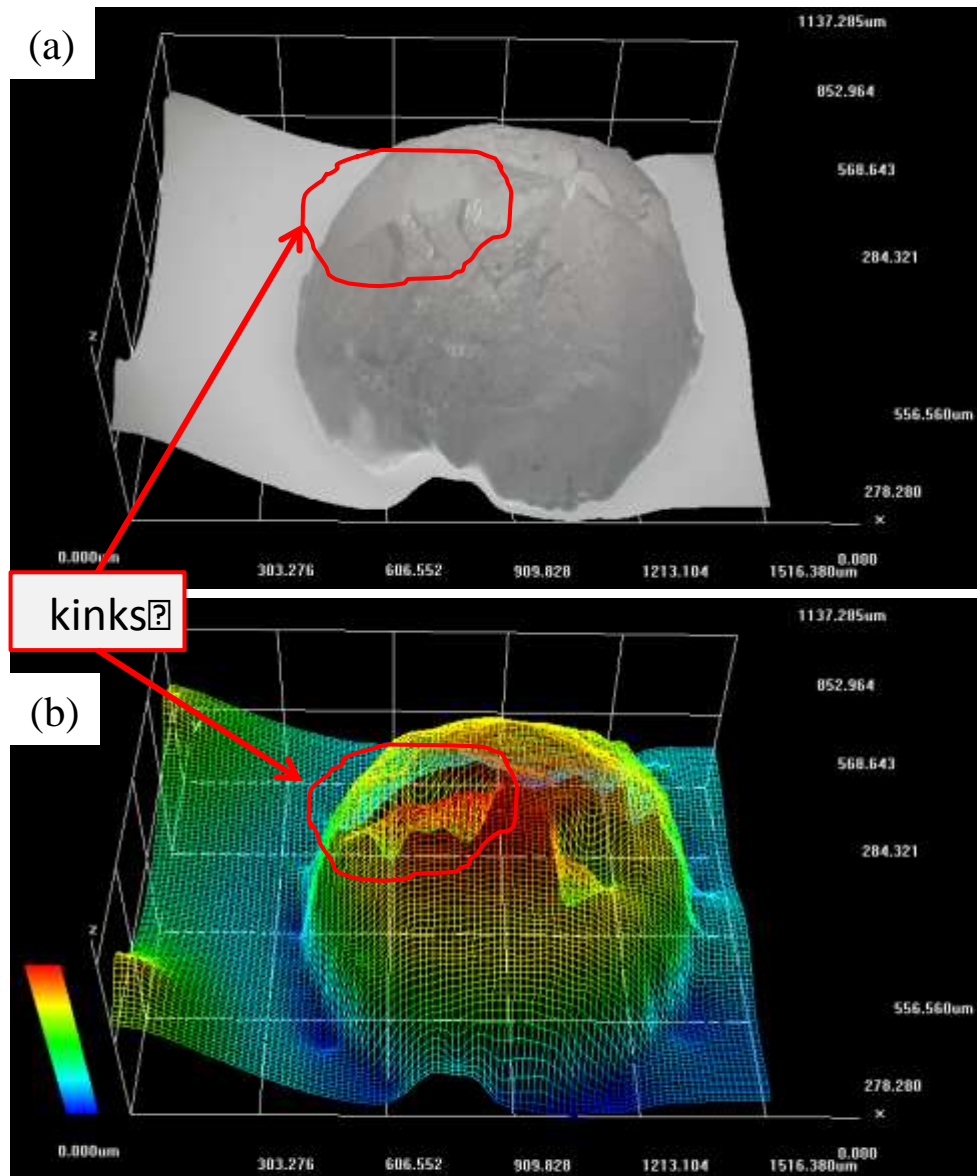
Figure 7. Optical confocal images of an Ottawa 20-30 sand particle: (a) 3D reconstructed image, and (b) meshed contour of the 3D images from the same viewpoint as in (a).
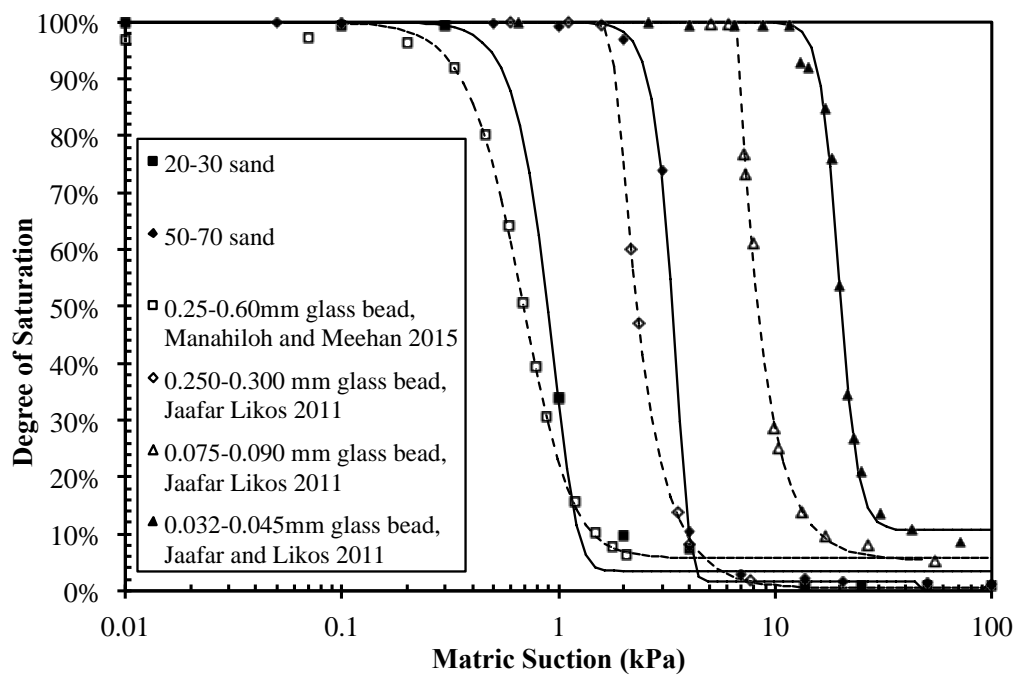
Figure 8. Soil water characteristic curves of uniformly sized particulate media.
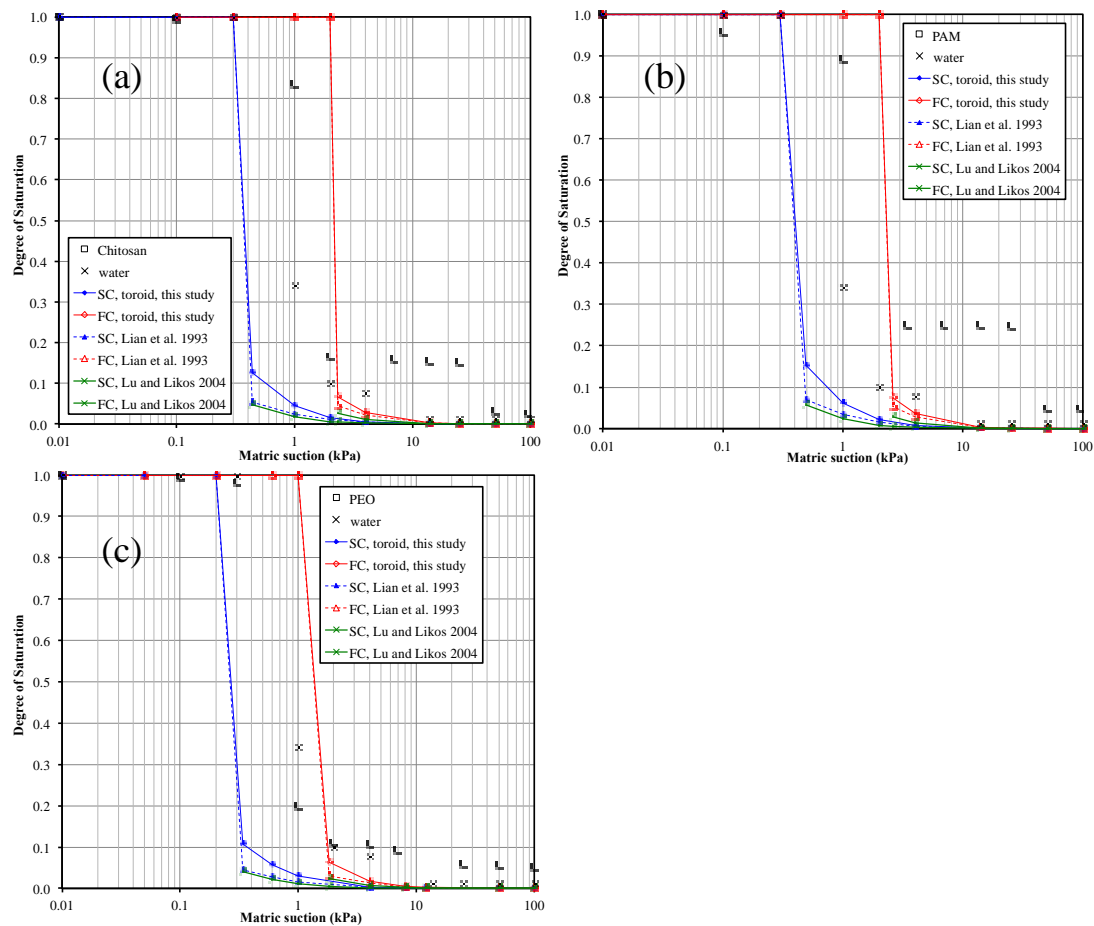
Figure 9. Soil water characteristic curves for Ottawa sand saturated with (a) chitosan, (b) PAM, and (c) PEO solutions.
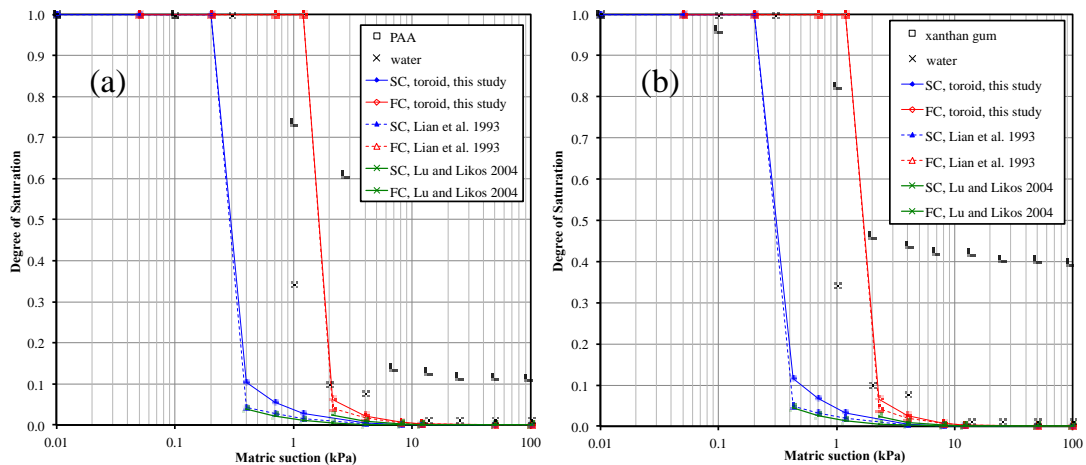
Figure 10. Soil water characteristic curves for Ottawa sand saturated with (a) PAA and (b) xanthan gum solutions.
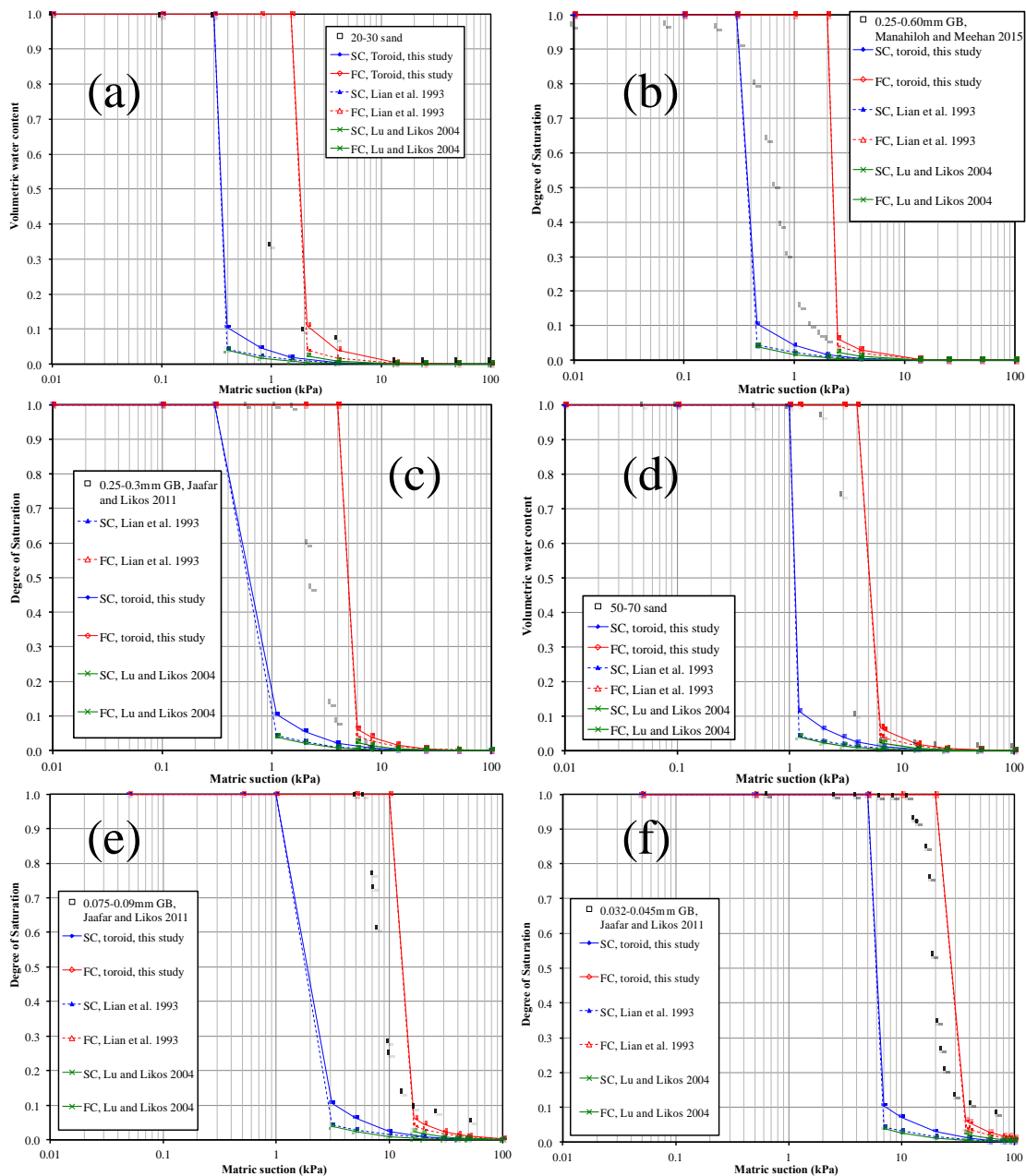
Figure 11. The calculated soil water characteristic curves of different uniformly sized particulate media with simple cubic and face-centered packing.

Table 1. Measured surface tension and contact angle values of different polymer solutions.

aqueous solution	concentration (g/L)	surface tension (dyne/cm)	contact angle (degree)
Deionized water	0	73.1	38.1
PEO	10	61.8	37.2
Chitosan	2	74.0	31.7
PAA	2	74.1	38.6
PAM	2	76.1	21.3
Xanthan gum	2	76.0	34.8

Table 2. D_{50} and SWCC fitting parameters of six different uniformly sized particulate media.

solution	particle	d_{50} (mm)	van Genuchten equation fitting parameters					air entry value (kPa)			reference
								by Eq. 2			
			a (kPa^{-1})	m	n	S_{sat}	S_r	simple cubic	face-centered cubic	$1/a$	
water	20-30 sand	0.7	0.659	7.674	4.363	1	0.034	0.4	2.1	1.5	this study
	50-70 sand	0.23	0.165	48.655	7.154	1	0.018	1.2	6.5	6.1	
	0.25-0.60mm glass bead	0.6	1.305	1.401	3.262	1	0.058	0.5	2.5	0.8	Manahiloh and Meehan 2015
	0.25-0.30mm glass bead	0.25	0.543	0.151	20.691	1	0.005	1.1	5.9	1.8	Jaafar and Likos 2011
	0.075-0.090mm glass bead	0.09	0.149	0.010	341.632	1	0.054	3.1	16.5	6.7	
	0.032-0.045mm glass bead	0.04	0.051	0.946	10.195	1	0.106	6.9	37.2	19.7	

REFERENCES

Ba-Te (2004). "Flow of Air-phase in Soils and Its Application in Emergent Stabilization of Soil Slopes." M. Phil., Hong Kong University of Science and Technology.

Bate, B., and Zhang, L. M. (2013). "Use of Vacuum for the Stabilization of Dry Sand Slopes." *Journal of Geotechnical and Geoenvironmental Engineering*, 139(1), 143-151.

Borja, R. I., Song, X., and Wu, W. (2013). "Critical state plasticity. Part VII: Triggering a shear band in variably saturated porous media." *Computer Methods in Applied Mechanics and Engineering*, 261, 66-82.

Cabalar, A. F., and Canakci, H. (2005). "Ground improvement by bacteria." *Proc, 3rd Biot Conference on Poromechanics*A.A. Balkema, 707-712.

Cao, S. C., Bate, B., Hu, J. W., and Jung, J. (2016). "Engineering Behavior and Characteristics of Water-Soluble Polymers: Implication on Soil Remediation and Enhanced Oil Recovery." *Sustainability*, 8(3), 205.

Cho, G. C., and Santamarina, J. C. (2001). "Unsaturated Particulate Materials—Particle-Level Studies." *Journal of Geotechnical & Geoenvironmental Engineering*, 127(1), 84-96.

Dai, S., Santamarina, J. C., Waite, W. F., and Kneafsey, T. J. (2012). "Hydrate morphology: Physical properties of sands with patchy hydrate saturation." *Journal of Geophysical Research*, 117(B11), B11205.

Di Emidio, G., Mazzieri, F., Verastegui-Flores, R. D., Van Impe, W., and Bezuijen, A. (2015). "Polymer-treated bentonite clay for chemical-resistant geosynthetic clay liners." *Geosynthetics International*, 22(1), 125-137.

Espinoza, D. N., and Santamarina, J. C. (2010). "Water‐CO2‐mineral systems: Interfacial tension, contact angle, and diffusion—Implications to CO2 geological storage." *Water Resources Research*, 46(W07537).

Fredlund, D. G., Morgenstern, N. R., and Widger, A. (1978). "Shear strength of unsaturated soils." *Canadian Geotechnical Journal*, 15, 313-321.

Fredlund, D. G., and Rahardjo, H. (1993). *Soil Mechanics for Unsaturated Soils*, John Wiley & Sons.

Fredlund, D. G., Rahardjo, H., and Fredlund, M. D. (2012). *Unsaturated Soil Mechanics in Engineering Practice*, John Wiley & Sons.

Fredlund, D. G., Xing, A., and Huang, S. (1994). "Predicting the permeability function for unsaturated soils using the soil-water characteristic curve." *Canadian Geotechnical Journal*, 31, 533-546.

Gee, M. L., and Healy, T. W. (1990). "Hydrophobicity effects in the condensation of water films on quartz." *Journal of Colloid & Interface Science*, 140(2), 450-465.

Gitirana, G. d. F. N., and Fredlund, D. G. (2004). "Soil-Water Characteristic Curve Equation with Independent Properties." *Journal of Geotechnical and Geoenvironmental Engineering*, 130(2), 209-212.

Götze, T., and Sonntag, H. (1988). "Forces between quartz surfaces bearing adsorbed macromolecules in good solvents." *Colloids & Surfaces*, 31(88), 181-201.

Ivanov, V., and Chu, J. (2008). "Applications of microorganisms to geotechnical engineering for bioclogging and biocementation of soil in situ." *Reviews in Environmental Science and Bio/Technology*, 7(2), 139-153.

Jaafar, R., and Likos, W. J. (2011). "Estimating Water Retention Characteristics of Sands from Grain Size Distribution using Idealized Packing Conditions." *Geotechnical Testing Journal*, 34(5), 1-14.

Javadi, S., Ghavami, M., Zhao, Q., and Bate, B. (2017). "Advection and retardation of non-polar contaminants in compacted clay barrier material with organoclay amendment." *Applied Clay Science*, 142, 30-39.

Jung, J., and Jang, J. (2016). "Soil–water characteristic curve of sediments containing a polyacrylamide solution." *Géotechnique Letters*, 6(1), 89-94.

Jung, J., Jang, J., and Ahn, J. (2016). "Characterization of a Polyacrylamide Solution Used for Remediation of Petroleum Contaminated Soils." *Materials*, 9(1), 16.

Kang, X., and Bate, B. (2016). "Shear Wave Velocity and Its Anisotropy of Polymer Modified High-Volume Class-F Fly Ash–Kaolinite Mixtures." *Journal of Geotechnical and Geoenvironmental Engineering*, 10.1061/(ASCE)GT.1943-5606.0001562

Lechman, J., and Lu, N. (2008). "Capillary Force and Water Retention between Two Uneven-Sized Particles." *Journal of Engineering Mechanics*, 134(5), 374-384.

Lechman, J., Lu, N., and Wu, D. (2006). "Hysteresis of Matric Suction and Capillary Stress in Monodisperse Disk-Shaped Particles." *Journal of Engineering Mechanics*, 132(5), 565-577.

Leong, E. C., and Rahardjo, H. (1997). "Review of Water Characteristic Curve Functions." *Geotechnical and Geo-Environmental Engineering*, 123, 1106-1117.

Li, X., Zhang, L. M., and Li, J. H. (2009). "Development of a Modified Axis Translation Technique for Measuring SWCCs for Gravel Soils at Very Low Suctions." *Geotechnical Testing Journal*, 32(6), 478-488.

Lian, G., Thornton, C., and Adams, M. J. (1993). "A Theoretical Study of the Liquid Bridge Forces between Two Rigid Spherical Bodies." *Journal of Colloid & Interface Science*, 161(1), 138-147.

Likos, W. J., and Jaafar, R. (2013). "Pore-Scale Model for Water Retention and Fluid Partitioning of Partially Saturated Granular Soil." *Journal of Geotechnical and Geoenvironmental Engineering*, 139(5), 724-737.

Lins, Y., Schanz, T., and Fredlund, D. G. (2009). "Modified Pressure Plate Apparatus and Column Testing Device for Measuring SWCC of Sand." *Geotechnical Testing Journal*, 32(5), 450-464.

Lu, N. (2016). "Generalized Soil Water Retention Equation for Adsorption and Capillarity." *Journal of Geotechnical and Geoenvironmental Engineering*, 142(10).

Lu, N., Kim, T.-H., Sture, S., and Likos, W. J. (2009). "Tensile Strength of Unsaturated Sand." *Journal of Engineering Mechanics*, 135(12), 1410-1419.

Lu, N., and Likos, W. J. (2004). *Unsaturated Soil Mechanics*, John Wiley & Sons.

Lu, N., Wu, B., and Tan, C. P. (2007). "Tensile Strength Characteristics of Unsaturated Sands." *Journal of Geotechnical and Geoenvironmental Engineering*, 133(2), 144-154.

Manahiloh, K. N., and Meehan, C. L. (2015). "Evolution of Interphase Contact Angle in Partially Saturated Granular Soils Using Digital Analysis of X-Ray Computed Tomography Images." *Geotechnical Special Publication*, 2092-2101.

Martin, G. R., Yen, T. F., and Karimi, S. (1996). "Application of biopolymer technology in silty soil matrices to form impervious barriers." *Proc., 7th Australia-New Zealand Geomechanics Conference*Adelaide, Australia.

Mitarai, N., and Nori, F. (2006). "Wet granular materials." *Advances in Physics*, 55(1-2), 1-45.

Mitchell, J. K., and Santamarina, J. C. (2005). "Biological Considerations in Geotechnical Engineering." *Journal of Geotechnical and Geoenvironmental Engineering*, 131(10), 1222-1233.

Molenkamp, F., and Nazemi, A. H. (2003). "Interactions between two rough spheres, water bridge and water vapor." *Géotechnique*, 53(2), 255-264.

Mollaei, A., Lake, L. W., and Delshad, M. (2011). "Application and variance based sensitivity analysis of surfactant–polymer flooding using modified chemical flood predictive model." *Journal of Petroleum Science and Engineering*, 79(1–2), 25-36.

Montoya, B. M., DeJong, J. T., and Boulanger, R. W. (2013). "Dynamic response of liquefiable sand improved by microbial-induced calcite precipitation." *Géotechnique*, 63(4), 302-312.

Or, D., and Tuller, M. (1999). "Liquid retention and interfacial area in variably saturated porous media: Upscaling from single-pore to sample-scale model." *Water Resources Research*, 35(12), 3591-3605.

Pham, H. Q. (2005). "A volume-mass constitutive model for unsaturated soils." PhD, University of Saskatchewan.

Puppala, A. J., Punthutaecha, K., and Vanapalli, S. K. (2006). "Soil-Water Characteristic Curves of Stabilized Expansive Soils." *Journal of Geotechnical and Geoenvironmental Engineering*, 132(6), 736-751.

Scalia, J., Benson, C. H., Bohnhoff, G. L., Edil, T. B., and Shackelford, C. D. (2014). "Long-term hydraulic conductivity of a bentonite-polymer composite permeated with aggressive inorganic solutions." *Journal of Geotechnical and Geoenvironmental Engineering*, 140(3).

Scheel, M., Seemann, R., Brinkmann, M., Di Michiel, M., Sheppard, A., Breidenbach, B., and Herminghaus, S. (2008). "Morphological clues to wet granular pile stability." *Nature materials*, 7(3), 189-193.

Song, X. (2017). "Transient bifurcation condition of partially saturated porous media at finite strain." *International Journal for Numerical and Analytical Methods in Geomechanics*, 41, 135–156. doi: 110.1002/nag.2552.

Song, X., and Borja, R. I. (2014). "Finite Deformation and Fluid Flow in Unsaturated Soils with Random Heterogeneity." *Vadose Zone Journal*, 13(5).

Song, X., and Borja, R. I. (2014). "Mathematical framework for unsaturated flow in the finite deformation range." *International Journal for Numerical Methods in Engineering*, 14(9), 658-682.

Song, X., Wang, K., and Ye, M. (2017). "Localized failure in unsaturated soils under non-isothermal conditions." *Acta Geotechnica*, DOI:10.1007/s11440-017-0534-4.

Song, X., Ye, M., and Wang, K. (2017). "Strain localization in a solid-water-air system with random heterogeneity via stabilized mixed finite elements." *International Journal for Numerical Methods in Engineering*, DOI:10.1002/nme.5590.

Tokunaga, T. K., Wan, J., Jung, J.-W., Kim, T. W., Kim, Y., and Dong, W. (2013). "Capillary pressure and saturation relations for supercritical CO2 and brine in sand: High-pressure Pc(Sw) controller/meter measurements and capillary scaling predictions." *Water Resources Research*, 49, 1-14.

van Genuchten, M. T. (1980). "A Closed Form Equation for Predicting the Hydraulic Conductivity of Unsaturated Soils." *Soil Science Society of America Journal*, 44, 892-898.

Yeom, S. H., Daugulis, A. J., and Lee, S. H. (2010). "Bioremediation of phenol-contaminated water and soil using magnetic polymer beads." *Process Biochemistry*, 45(9), 1582-1586.

Zhao, Q., Choo, H., Bhatt, A., Burns, S. E., and Bate, B. (2017). "Review of the fundamental geochemical and physical behaviors of organoclays in barrier applications." *Applied Clay Science*, 142, 2-20.

Zhao, X. (2014). "Measurements and transient multistep outflow simulation of soil-water characteristic curve for soils modified with biopolymers." Master of Science, Missouri University of Science and Technology.

V. MEASURING RETARDATION FACTORS OF [133]CESIUM AND [88]STRONTIUM CATIONS USING COLUMN TEST

Junnan Cao[1], Bate Bate[2], Abdelmalek Bouazza[3] and Wen Deng[4]

[1]Graduate Research Assistant, Department of Civil, Architectural, and Environmental Engineering, Missouri University of Science and Technology, United States

[2] "100-Talents Program" Professor, Institute of Geotechnical Engineering, College of Civil Engineering and Architecture, Zhejiang University

[3]Professor, Department of Civil Engineering, 23 College Walk, Monash University, Melbourne, Vic. 3800, Australia

[4]Assistant Professor, Department of Civil, Architectural, and Environmental Engineering, Missouri University of Science and Technology, United States

ABSTRACT

A flow-through column test setup was developed to measure the breakthrough curves of [133]cesium (Cs) and [88]strontium (Sr) cations in a natural silty sand. The retardation factors of Sr and Cs cations were found to be 3.561 and 27.369, respectively. These values are slightly lower than the range given by USEPA under similar but broader range of fines content and pH. This slight difference is attributed to the lower fines content of the soil, high input concentrations of both Cs and Sr, and the competing monovalent and divalent cations in the influent with high ionic strength. Although not significant in this study, particle migration was observed. The column setup developed in this study eliminates the uncertainties from partial saturation and fluctuating pressure difference across the sample column as typically encountered in a traditional flow-

through column test setup, and is recommended to use for future breakthrough curve

measurements.

KEYWORDS: flow-through column test, cesium, strontium, breakthrough curve,

retardation factor, distribution coefficient.

1. INTRODUCTION

Transport of inorganic radioactive matter in soils, such as earthen barriers and the

likes involves advection, diffusion, dispersion, adsorption, ion exchange and degradation.

Retardation factor, R_d, denotes the ability of a porous medium (e.g. soil) to delay

contaminants propagation (USEPA 1999), it is defined as follows:

$$R_d = \frac{v_p}{v_c} \tag{1}$$

where R_d is the retardation factor, v_p is the pore water velocity and v_c is the contaminant

velocity. Another commonly used coefficient describing contaminant distribution

between solids and pore fluid is the partition coefficient (or distribution coefficient) K_d

(ml/g). K_d can be quantified using Equation 2:

$$R_d = 1 + \frac{K_d \rho_b}{n} \tag{2}$$

where ρ_b represents the bulk density (g/ml) and n the total porosity. Factors influencing

K_d and R_d values include mineralogical composition of the soil, grain size distribution,

pore fluid speciation, pH, degree of saturation, hydraulic gradient (flow rate) and organic

content (USEPA 1999). Therefore, both K_d and R_d values are specific to the field

conditions (Shackelford 1995; Shackelford and Redmond 1995; Zeng 2015).

Batch and flow-through column test are the two most commonly used methods to measure retardation factors (USEPA 1999). Batch test often identifies soil properties when contaminants are thoroughly mixed with soils, or are at equilibrium in adsorption and ion exchange with soils; whereas column test simulates contaminant transport process under hydraulic and mechanical conditions similar to those in the field, and mimics the process of contaminant persistence in soil column in terms of breakthrough curve (BTC). Therefore, column test is residence time dependent (Reddy and Al-Hamdan 2013; Reddy et al. 2011).

A well-detailed procedure for column test is provided by USEPA (1999). However, a major disadvantage of the USEPA method is its inability to guarantee sample saturation (van Genuchten and Wierenga 1986). Hydraulic conductivity (k) of a porous medium, which the flow rate is proportional to, is highly dependent on the degree of saturation, as several orders of magnitude reduction in k could occur when the degree of saturation decreases by only 20% (Fredlund et al. 2012). Backpressure (ASTM D5084-16a), or pressurizing soil sample with additional pore water pressure, is the primary technique used to increase the degree of saturation of a soil sample. Redmond and Shackelford (1994) used backpressure and a constant flow rate column setup by automated syringe control. Javadi et al. (2017) used backpressure and falling head column setup with fluctuating hydraulic gradient. To date, backpressure has not been used under constant hydraulic gradient testing setup. Another disadvantage of the USEPA method is the side leakage-prone rigid wall design, a problem especially pronounced for coarse-grained materials, such as gravel and sand. A flexible wall triaxial cell sample can avoid the potential preferential flow channel along the side of a sample column, or side-

leakage, due to the compression of rubber membrane against the sample column by the chamber pressure (Redmond and Shackelford 1994; Javadi et al. 2017; Reddy 2011, 2013).

Radioactive matters often degrade over time spans of over 10,000 years, which is beyond the time scale of a regular laboratory testing. Even geotechnical centrifuge tests, which can simulate long-term advection of a contaminant transport by scaling law (Taylor 2005; Zeng 2015), cannot fully simulate other transporting processes such as cation exchange, diffusion, adsorption and attenuation (for radioactive matters). Alternatively, numerical simulation must be used to predict the transport of radioactive matters in nuclear engineering, and the precision of the input parameters, such as retardation factors, are of paramount importance.

The objective of this study is to propose a new flow-through column test setup to provide more accurate retardation factors, and verify its functionality by performing breakthrough tests with stable form Cs-135 and Sr-88 cations. Calculated retardation factors (R_d) or partition coefficients (K_d) from this study are compared with previous studies and USEPA suggested values. Reasons for the different R_d/K_d are analyzed and thereby elucidating the advantages of the flow-through column setup designed in this study. The limitation of the designed setup relating to the particle migration is also investigated.

2. MATERIALS AND METHODOLOGY

Soil samples were taken from a proposed nuclear power plant site, 0.6 m below ground surface. To preserve the soil structure and porosity, sampling tubes (diameter =

86.4 mm, height = 340 mm, thickness = 2.43 mm) were directly pushed into the ground (ASTM D4220), extracted, sealed with hot wax on both ends, and shipped with foam-padded containers to the geotechnical laboratory at Missouri University of Science and Technology (Rolla, MO, USA) by air. The water content, density, coefficient of uniformity (C_u), coefficient of curvature (C_c) and cation exchange capacity (Hazen Research, Inc.) of the soil are 0.70%, 1880 kg/m^3, 21.80, 0.18 and 4.99 meq/100g, respectively. The soil is composed of 60% calcite, 16% quartz, 11% gypsum, 11% cordierite, and 2% gobbinsite. The grain size distribution curve is shown in Fig. 1 with other soils from previous studies for comparative purposes (to be discussed later in the paper). The soil is classified as poorly graded sand with silt and gravel (SP-SM) (ASTM D2487-11).

A synthetic groundwater solution (GWS) with an electrical conductivity of 1.131 S/m and pH of 4.24, was prepared in the laboratory to best approximate the in situ groundwater condition. The chemical composition of GWS is shown in Table 1. Non-radioactive form Cs-133 ions (from CsCl powder) and Sr-88 ions (from $Sr(NO_3)_2$ powder) were added simultaneously in the GWS at 0.25 g/10L (25 ppm) and 1 g/10L (100 ppm), respectively.

To preserve the in situ porosity, soil structure, and subsequently the hydraulic conductivity of the field soil samples, freeze-thaw method was used for mounting the soil sample in the triaxial cell. The methodology can be summarized as follow: First, the sample tube was gradually submerged in GWS for 2 days (Fig. 2a). Second, the plastic tube was placed in a freezer at -4 ℃ for 3 days to freeze the sample. Third, the frozen sample was extruded (Fig. 2b). The volume change of the soil sample after being frozen

was measured to be less than 1% of the original volume. Finally, the frozen sample was quickly trimmed into a cylinder (86.4 mm $\times$ 164.0 mm, diameter $\times$ height), wrapped with a rubber membrane, and mounted in the triaxial cell. Then a confining pressure, i.e., chamber pressure minus sample backpressure, of 34.5 kPa was applied (Fig. 3). To enclose the non-standard sized sample (86 mm in diameter), a slightly larger membrane (102 mm in diameter) was used. Due to the confining pressure, leakage through the side wrinkles was unlikely and was not observed. After thawing for 2 days, the sample was subjected to a backpressure of 310 kPa, and a Skempton's B value of 98.8% was achieved indicating that full saturation has been reached (ASTM D5084-16a; Reddy 2011, 2013, Javadi et al. 2017; Redmond and Shackelford 1994; Shackelford and Redmond 1995). The backpressure was maintained throughout testing. The sample was long enough to avoid possible effects of diffusion and dispersivity as reported for short columns by Li et al. (2009).

Pressure equal to the sample backpressure was applied in the pressure tank, inflow and outflow tanks (Figs. 3) to maintain sample backpressure. Double cell overflow setup inside the inflow tank (Fig. 3) fixed the elevation of the influent water level. A peristaltic pump transferred GWS stored in the pressure tank to the overflow cell to maintain the water level at the rim of the overflow cell (Fig. 3). The elevation of the outflow port was also glued to the chamber sidewall. By changing elevation of the outflow tank, a constant pressure difference across the sample (i.e., hydraulic gradient) was achieved. Additional pressure could be applied to the pressure tank and inflow tank to create larger hydraulic gradients if needed (Fig. 3).

Aqueous samples were taken from the effluent via a three-way valve (Fig. 3). The solution samples were diluted 1000 times with 1% trace metal grade HNO_3 for inductively coupled plasma mass spectrometry (ICP-MS) (NexION 350D ICP-MS, PerkinElmer) analysis, where [133]Cs and [88]Sr were monitored for quantification in standard mode. High-purity Cesium and Strontium standard were used to calibrate the instrument: Yttrium (Y) and Terbium (Tb) were used as internal standard for Sr and Cs analysis, respectively. The instrument detection limit (IDL) was 0.1μg/L for Cs and Sr. Quality control (QC) included: instrument calibration, QC blank, reagent blank, QC standard, sample duplication, and sample spike.

3. RESULTS

The breakthrough curves (BTCs) of strontium ([88]Sr) and cesium ([133]Cs) as well as two fitting curves with functional equations were presented in Fig. 4. It was observed that: (1) Initial concentration of [133]Cs and [88]Sr effluents were 0 and 6.815 ppm, respectively; (2) Significant fluctuation was detected on [88]Sr BTC; (3) Both [133]Cs and [88]Sr breakthrough curves reached plateau values. Dimensions of soil sample and hydraulic parameters were exhibited in Table 2. Since pore water velocity (v_p) only related to hydraulic conductivity, hydraulic gradient and porosity (the equation is v_p = seepage velocity/porosity = ki/n), v_p values were same for both [88]Sr and [133]Cs. Initial and final concentrations, and t_{50} (time when the effluent concentration reaches 50% of the difference between initial and final concentrations) were determined by fitting curves. Contaminant velocities (v_c) thereby could be calculated with the equation of $v_c = H/t_{50}$, where H was the height of soil sample (Table 2). Calculated v_p and v_c values with retardation factors and partition coefficients of

[88]Sr and [133]Cs were tabulated in Table 3. Table 4 showed comparison of K_d values from this study with USEPA and previous studies. Other information including soil types, CEC and background solutions were also summarized in this table.

4. TRANSPORT OF Cs-133

The measured K_d for cesium is 4.986 mL/g, which is lower than the 10 - 3500 mL/g range given by USEPA (1999) for soils with clay content (sub-2 μm portion) < 4 wt.% and pH < 5. Cesium ions adsorb strongly on mineral surface primarily through cation exchange, with minimal impacts from pH, humic acid or chelating agents (Ames and Rai 1978). The affinity of monovalent cations in the influent follows lyotic series: $Cs^+ > K^+ > Na^+$ (Sposito 1989). Inui et al. (2017) performed the batch test on a decomposed granite soil by mixing Cs^+ with Na^+, K^+ and Ca^{2+} respectively (Table 4). They reported that lower K_d values for Cs adsorption were achieved at high concentration of K^+, and postulated that K^+ lessened Cs adsorption. Therefore K^+ (29.99 mg/L) was deemed to be the primary competitor to Cs^+ (25 mg/L) besides other divalent cations (Ca^{2+}, Mg^{2+}), and contributed to a lower K_d value recorded in this study. It was also reported that Cs adsorption was strongly sensitive to the ionic strength of the pore fluid (Liu et al. 2004; McKinley et al. 2004; Papelis 2001; Zachara et al. 2002). Furthermore, the extremely low (< 0.35 wt.%) clay content (sub-2 μm fraction) of this study also led to low K_d values. Flury et al.(2004) used Hanford sediments (95.2% 50-2000 μm, 3.8% 2-50 μm and 1% < 2 μm particles) to perform both batch and column tests to measure K_d for Cesium. K_d decreased from 32 to 3 mL/g as the NaCl concentration increased from 0.1 to 1 mol/L (2300-23000 mg/L, Table 4). The K_d value (4.986 mL/g) in this study agreed

well with that reported in Flury et al. (2004) as the fine portions (< about 40% passing) of the grain size distribution curves for both soils (Fig. 1) were similar and both soils were exposed to similar ionic strength (electrical conductivity of 1.131 S/m). In addition, the competition of Cs^+ and Na^+ could also result in the lower K_d value, considering the high concentration of Na^+ in the synthetic GWS. Reynolds et al. (1982) evaluated K_d of Sr and Cs using a uniform saturated sand ($d_{50} = 0.13$ mm) with similar background compositions of this study (Table 4). The results of K_d from batch test was 77 ± 2 mL/g for Cs, which was higher than the K_d value in this study (4.986 mL/g) despite of the similar grain size distribution at the sub-40% passing range (i.e., the fine portion, which dominated the solid-liquid interface interaction) between the two studies (Fig. 1). This difference is primarily because a batch test allows thorough mixing between Cs and soils, and therefore yields higher K_d values than a column test does.

5. TRANSPORT OF Sr-88

K_d for Strontium was 0.484 mL/g, which was within the same order of magnitude as the range given by USEPA (USEPA 1999), 1-40 ml/g, under similar but broader range of testing conditions, i.e., clay content (sub-2 μm portion) < 4 wt.% and pH < 5 (USEPA 1999). Smaller K_d for strontium was probably due to the competition from divalent cations, i.e., Ca^{2+} (651.72 mg/L) and Mg^{2+} (470.76 mg/L), in GWS for adsorption sites through cation exchange reaction. Another contributor to low K_d values is the very low clay content (< 0.35%). Porro et al. (2000) performed a column test on saturated crushed basalt sample, and determined that K_d for strontium to be 2.60-3.66 mL/g. The particle size of the crushed basalt ranged from 0.25 to 2 mm, similar to the soil used in this study

(Fig. 1). Reynolds et al. (1982) evaluated K_d for Sr of a saturated uniform sand (d_{50} = 0.13 mm). The results of K_d from batch test were 15 $\pm$ 0.6 mL/g for Sr. The higher K_d values were postulated to be due to the more residence time by thorough mixing in batch test. Compositions of background solutions used in above mentioned studies were similar with those in this study (Table 4).

6. CONCENTRATION FLUCTUATION AND NON-ZERO INITIAL EFFLUENT CONCENTRATION

Although being reported as ubiquitous in the environment with concentration in soils ranging from 0.3 - 25 mg/kg (Lindsay 1979), stable cesium concentration originally in the soil sample tested in this study was equal to zero as suggested by the initial effluent concentration (Fig. 4). On the contrary, the initial concentration of strontium effluent was 6.815 ppm (Fig. 4), which suggested that strontium existed in the original soil sample before the breakthrough test. This observation agrees with the fact that strontium is the 15th most abundant element on earth (Turekian and Wedepohl 1961), and that the strontium concentration in ocean water is 8 mg/L (Angino et al. 1966).

High fluctuation was observed in the BTC of Sr. This is attributed to the more complex cation exchange interaction among divalent cations (Ca^{2+}, Mg^{2+}, Sr^{2+}) and even including monovalent cations (K^+, Na^+), as well as the very likely co-precipitation of Sr^{2+} with Ca^{2+} provided sufficient SO_4^{2+} in GWS. These factors could also contribute to the fact that the maximum effluent Sr concentration (about 42.5 ppm) is more than the influent Sr concentration (40 ppm). This fact was also reported in other BTC of strontium (Porro et al. 2000).

7. ADVANTAGES OF THE PROPOSED COLUMN TESTING SYSTEM

Albeit lower K_d and R_d values for both Cs^+ and Sr^{2+} were consistently recorded compared to the materials compiled in USEPA (1999), these lower values were justifiable considering the high ionic strength and low clay contents. Therefore, the BTCs measured using the proposed flow-through column testing system are able to produce reasonable K_d values. Given the advantages of being able to simulate constant and large range of hydraulic gradient throughout the test, and to ensure 100% saturation with backpressure technique, the proposed setup is more logically sound and practically useful in achieving accurate K_d and R_d values for engineering practice, especially those with high demand for accurate representation of the in situ condition, i.e., the transport of radioactive matters.

8. PARTICLE MIGRATION

Hydraulic conductivity of a granular material is governed by its fines portion as illustrated by Hazen's equation (Chapuis 2004; Vienken and Dietrich 2011)

$$k = C \, d_{10}^{2} \tag{3}$$

where C is a constant and d_{10} is the sieve size corresponding to 10% particle passing. When the fines content (< 75 μm, ASTM D2487-11) exceeds a threshold value (FCt), approximately from 8 to 12% (Benson et al. 1994), k would be close to that of a silt or clay; on the contrary, if fines content is lower than FCt, k would be close to that of the coarser materials. During a flow-through column test, fines could be picked up by flowing fluid, migrate downstream (upward in this study) and accumulate before the exit

(top of the sample). In this study, sieve analysis of the top, middle and bottom portion of another soil column test with similar grain size distribution (Fig. 5), hydraulic gradient and duration to the soil column reported in Fig. 5 revealed the presence of particle migration, as grain size distribution curve of the top portion increased. Because of the high fines content before and after flow-through testing ($28\% > FC > 12\%$) (Fig. 5), particle migration was not deemed significant to influence k in this study. However, k of soils with fines content no more than FCt could suffer from particle migration. In the event of extensive particle migration, k would change significantly, which requires significantly higher hydraulic gradient to maintain constant flow rate. This case, i.e. extensive particle migration, however, rarely occurs in nature. Instead, constant hydraulic gradient setup is more realistic and can be considered as reliable.

9. SUMMARY

This study developed a column test setup with constant hydraulic gradient and full soil sample saturation using a triaxial cell and peristaltic pump to measure the breakthrough curves of Sr and Cs for a natural silty sand. Following USEPA's t_{50} method, retardation factors of the sand for Sr and Cs were determined from the breakthrough curves to be 3.561 and 27.369, respectively. The distribution coefficient (K_d) of Sr and Cs, calculated from R_d values, were 0.484 and 4.986 ml/g respectively. These results were comparable to the range given by USEPA (1999) under similar but broader range of fines content and pH. The slightly lower R_d values recorded in this study were attributed to the lower fines content of the soil sample, high input concentrations of both Cs and Sr, and the competing monovalent and divalent cations in the influent with high ionic strength

(electrical conductivity of 11.31 mS/cm). Particle migration observed in this study did not influence k in this study due to the high fines content (ranging from 12-28%) before and after the column test. The column setup developed in this study eliminates the uncertainties from partial saturation and fluctuating pressure difference across the sample column in a traditional flow-through column test setup, and is recommended to use for future breakthrough curve measurements.

ACKNOWLEDGEMENTS
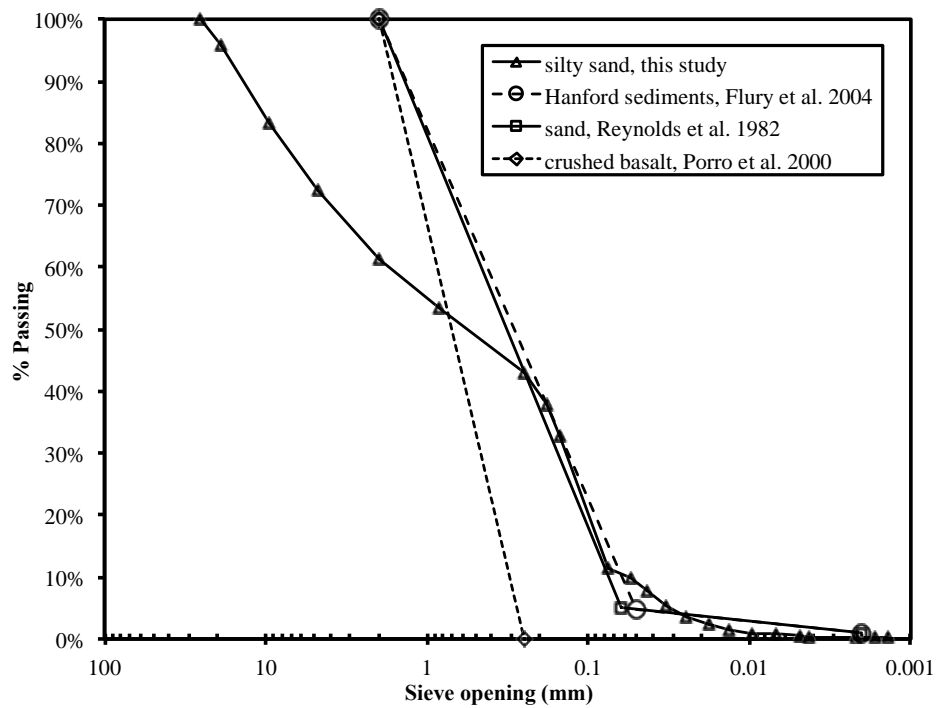
Figure 1. Grain size distribution curves.

Figure 2. (a) Soil sample submerged in GWSs; (b) frozen soil sample.
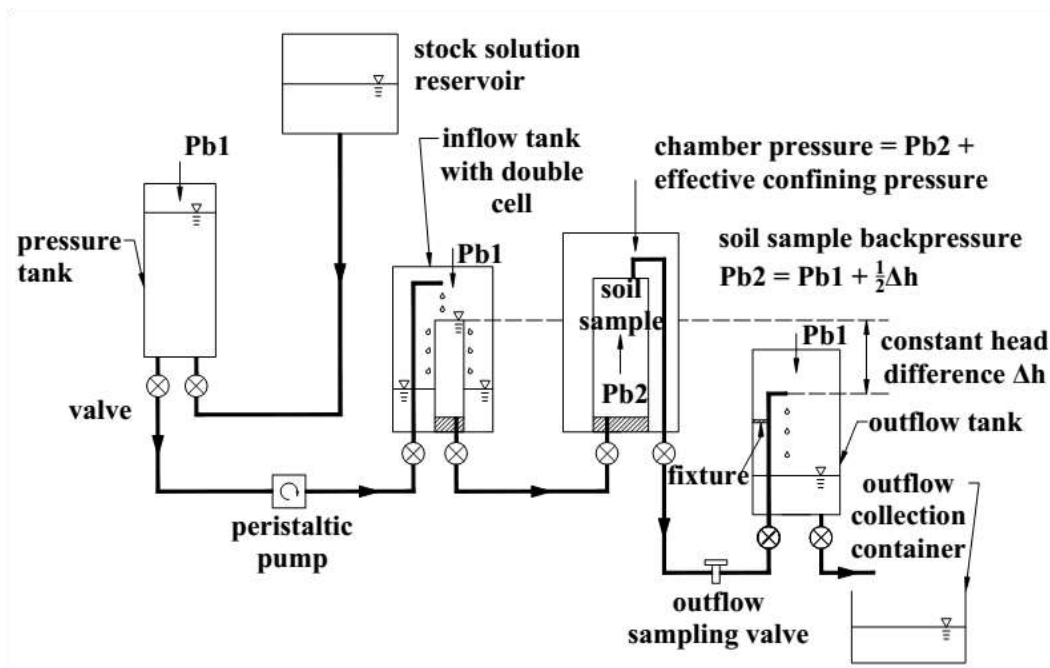
Figure 3. Schematic setup of the back pressured constant pressure difference column testing device.
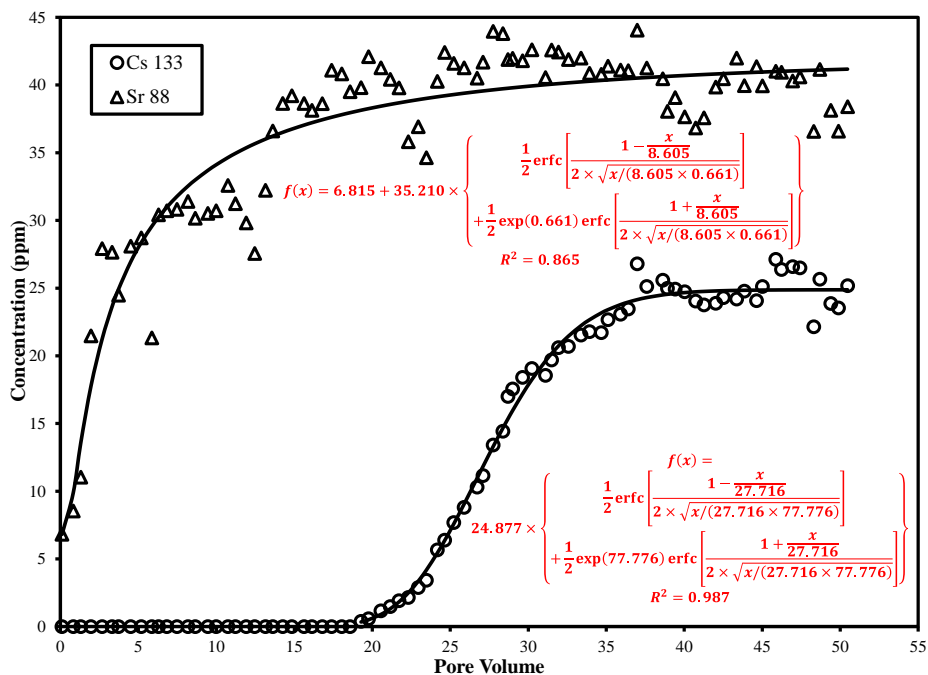
Figure 4. Sr and Cs breakthrough curves.
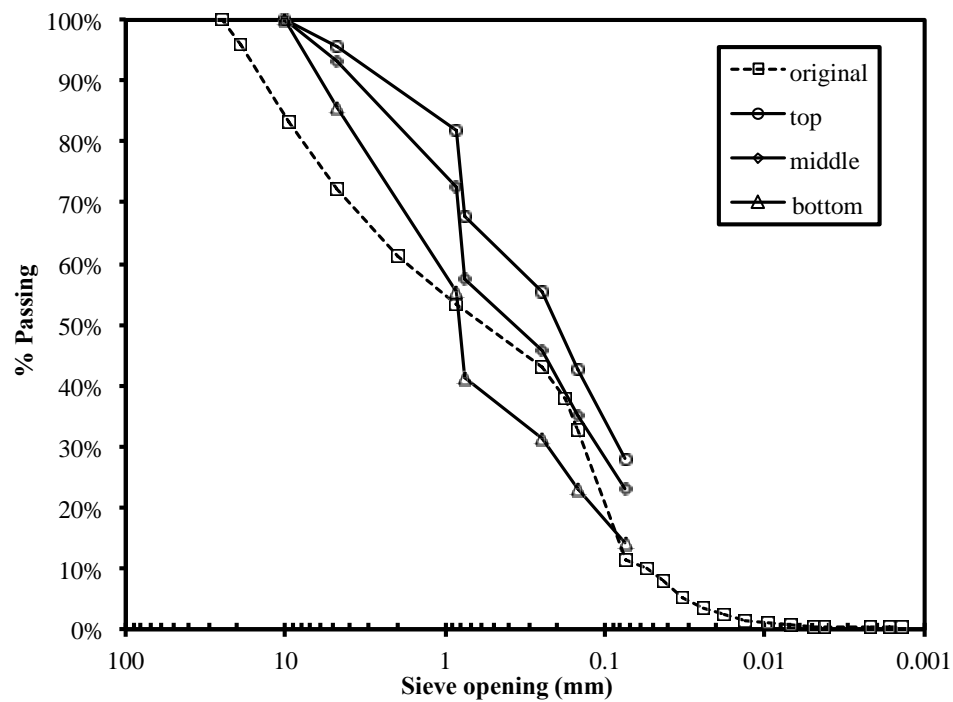
Figure 5. Particle size distribution curves at top, middle and bottom sections of the soil column after flow-through testing.

Table 1. Chemical composition of the synthetic GWS.

Chemical name	Molecular formula	mol/10L	g/10L
Magnesium sulfate	$MgSO_4$	0.19615	23.538
Sodium sulfate	Na_2SO_4	0.10223	14.517
Potassium nitrate	KNO_3	0.00769	0.777
Calcium nitrate	$Ca(NO_3)_2$	0.02803	4.597
Calcium chloride	$CaCl_2$	0.1349	14.974
Sodium chloride	$NaCl$	0.69373	40.583

Table 2. Dimensions and hydraulic parameters.

Parameters	Values
Soil sample height (H, m)	0.164
Soil sample diameter (d, m)	0.086
Mass of soil sample (m, kg)	1.936
Water content (w, %)	22.720
Porosity (n)	0.381
Specific gravity (Gs)	2.650
Cross section area of soil sample (A, m^2)	5.863×10^{-3}
Total water head difference (h, m)	0.214
Volume of water collected (V, m^3)	2.565×10^{-4}
Collecting time (t, min)	821
Hydraulic conductivity (k, m/s)	6.807×10^{-7}
Hydraulic gradient (i)	1.305

Table 3. Retardation factors and partition coefficient.

n	0.381	
ρ_b (g/ml)	2.014	
	^{88}Sr	^{133}Cs
t_{50} (h)	69.528	534.429
v_p (m/s)	2.333×10^{-6}	2.333×10^{-6}
v_c (m/s)	6.552×10^{-7}	8.524×10^{-8}
R_d	3.561	27.369
K_d (ml/g)	0.484	4.986

Table 4. Comparison of K_d from this study with USEPA and previous studies.

	Soil type	CEC (meq/ 100g)	Non-radioactive ions (mg/L)	Synthetic GWS/solution (mg/L)	K_d (mL/g)
USEPA	Soils with clay content < 4 wt.%	-	-	-	Cs: 10-3500 Sr: 1-40
This study (Column test)	SP-SM, clay content < 0.35 wt.%	4.99	$Cs^+ = 25$ $Sr^{2+} = 100$	$Mg^{2+} = 470.76$ $Na^+ = 2065.84$ $K^+ = 29.99$ $Ca^{2+} = 651.72$	^{133}Cs: 4.986 ^{88}Sr: 0.484
Inui et al. 2017 (Batch test)	Decomposed granite soil (< 2mm)	9.3	$Cs^+ = 10$	$Na^+ = 20$ or $Na^+ = 100$ or $K^+ = 20$ or $K^+ = 100$ or $Ca^{2+} = 20$ or $Ca^{2+} = 100$	Cs: 190 Cs: 160 Cs: 72 Cs: 38 Cs: 57 Cs: 37
Flury et al. 2004 (Batch and column tests)	Hanford sediments, clay content $= 1\%$	21.58	$Cs^+ = 3.4$-68.5	$Na^+ = 2300$ or $Na^+ = 23000$	Cs: 32 Cs: 3
Reynolds et al. 1982 (Batch test)	Uniform sand ($d_{50} = 0.13$ mm)	1.06	$Cs^+ = 8 \times 10^{-10}$-4×10^{-4} $Sr^{2+} = 3 \times 10^{-8}$-$0.7$	$Mg^{2+} = 1.9$ $Na^+ = 10.8$ $K^+ = 3.2$ $Ca^{2+} = 5.1$	Cs: 77±2 Sr: 15±0.6
Porro et al. 2000 (Column test)	Crushed basalt (size = 0.25-2 mm)	6.05	$Sr^{2+} = 0.5$	$Mg^{2+} = 8.3$ $Na^+ = 19.7$ $K^+ = 9.8$ $Ca^{2+} = 11.5$	Sr: 2.60-3.66

REFERENCES

ASTM D4220/D4220M-14 Standard Practices for Preserving and Transporting Soil Samples, ASTM International, West Conshohocken, PA, 2014, https://doi.org/10.1520/D4220_D4220M

ASTM D5084-16a Standard Test Methods for Measurement of Hydraulic Conductivity of Saturated Porous Materials Using a Flexible Wall Permeameter, ASTM International, West Conshohocken, PA, 2016, https://doi.org/10.1520/D5084-16A

ASTM D4767-11 Standard Test Method for Consolidated Undrained Triaxial Compression Test for Cohesive Soils, ASTM International, West Conshohocken, PA, 2011, https://doi.org/10.1520/D4767-11

ASTM D2487-11 Standard Practice for Classification of Soils for Engineering Purposes (Unified Soil Classification System), ASTM International, West Conshohocken, PA, 2011, https://doi.org/10.1520/D2487-11

Ames, L. L., and Rai, D. (1978). "Radionuclide Interactions with Soil and Rock Media." Office of Radiation Programs, U.S. Environmental Protection Agency, Las Vegas, Nevada, USA.

Angino, E. E., Billings, G. K., and Andersen, N. (1966). "Observed variations in the strontium concentration of sea water." *Chemical Geology*, 1(C), 145-153.

Benson, C. H., Zhai, H., and Wang, X. (1994). "Estimating Hydraulic Conductivity of Compacted Clay Liners." *Journal of Geotechnical Engineering*, 120(2), 366-387.

Bodansky, D. (2004). "Nuclear Energy-Principles, Practices, and Prospects (Second Edition)." D. Bodansky, ed., Springer, New York.

Chapuis, R. P. (2004). "Predicting the saturated hydraulic conductivity of sand and gravel using effective diameter and void ratio." *Canadian Geotechnical Journal*, 41(5), 787-795.

Flury, M., Czigány, S., Chen, G., and Harsh, J. B. (2004). "Cesium migration in saturated silica sand and Hanford sediments as impacted by ionic strength." *Journal of contaminant hydrology*, 71(1), 111-126.

Fredlund, D. G., Rahardjo, H., and Fredlund, M. D. (2012). *Unsaturated Soil Mechanics in Engineering Practice*, John Wiley & Sons.

Inui, T., Katsumi, T., and Takai, A. (2017). "Effects of cations on cesium sorption/desorption characteristics of soil layer for containment of radioactively polluted waste." The 19th International Conference on Soil Mechanics and Geotechnical Engineering, Seoul, South Korea, 3131-3134.

Javadi, S., Ghavami, M., Zhao, Q., and Bate, B. (2017). "Advection and retardation of non-polar contaminants in compacted clay barrier material with organoclay amendment." *Applied Clay Science*, 142, 30-39.

Li, M. H., Wang, T. H., and Teng, S. P. (2009). "Experimental and numerical investigations of effect of column length on retardation factor determination: a case study of cesium transport in crushed granite." *Journal of hazardous materials*, 162(1), 530-535.

Lindsay, W. L. (1979). *Chemical Equilibria in Soils*, J. Wiley and Sons, New York, New York.

Liu, C., Zachara, J. M., and Smith, S. C. (2004). "A cation exchange model to describe Cs+ sorption at high ionic strength in subsurface sediments at Hanford site, USA." *Journal of contaminant hydrology*, 68(3-4), 217-238.

McKinley, J. P., Zachara, J. M., Heald, S. M., Dohnalkova, A., Newville, M. G., and Sutton, S. R. (2004). "Microscale Distribution of Cesium Sorbed to Biotite and Muscovite." *Environmental Science & Technology*, 38(4), 1017-1023.

Papelis, C. (2001). "Cation and anion sorption on granite from the Project Shoal Test Area, near Fallon, Nevada, USA." *Advances in Environmental Research*, 5(2), 151-166.

Porro, I., Newman, M. E., and Dunnivant, F. M. (2000). "Comparison of Batch and Column Methods for Determining Strontium Distribution Coefficients for Unsaturated Transport in Basalt." *Environmental Science & Technology*, 34(9), 1679-1686.

Reddy, K. R., and Al-Hamdan, A. Z. (2013). "Enhanced Sequential Flushing Process for Removal of Mixed Contaminants from Soils." *Water, Air, & Soil Pollution*, 224(12), 1709.

Reddy, K. R., Al-Hamdan, A. Z., and Ala, P. (2011). "Enhanced Soil Flushing for Simultaneous Removal of PAHs and Heavy Metals from Industrial Contaminated Soil." *Journal of Hazardous, Toxic, and Radioactive Waste*, 15(3), 166-174.

Redmond, P., and Shackelford, C. D. (1994). "Design and Evaluation of a Flow Pump System for Column Testing." Geotechnical Testing Journal, 17(3), 269-281.

Reynolds, W. D., Gillham, R. W., and Cherry, J. A. (1982). "Evaluation of distribution coefficients for the prediction of strontium and cesium migration in a uniform sand." *Canadian Geotechnical Journal*, 19(1), 92-103.

Shackelford, C. D. (1995). "Cumulative Mass Approach for Column Testing." *Journal of Geotechnical Engineering*, 121(10), 696-703.

Shackelford, C. D., and Redmond, P. L. (1995). "Solute Breakthrough Curves for Processed Kaolin at Low Flow Rates." *Journal of Geotechnical Engineering*, 121(1), 17-32.

Sposito, G. (1989). *The Chemistry of Soils*, Oxford University Press, Oxford, UK.

Taylor, R. N. (2005). "Geotechnical Centrifuge Technology." Blackie Academic and Professional, an imprint of Chapman & Hall, Bishopbriggs, Glasgow.

Turekian, K. K., and Wedepohl, K. H. (1961). "Distribution of the Elements in Some Major Units of the Earth's Crust." *GSA Bulletin*, 72(2), 175-192.

USEPA (1999). "Volume I: The Kd Model, Methods of Measurement, and Application of Chemical Reaction Codes." *Understanding Variation in Partition Coefficient, Kd, Values*, Office of Air and Radiation, United States Environmental Protection Agency.

USEPA (1999). "Volume II: Review of Geochemistry and Available Kd Values for Cadmium, Cesium, Chromium, Lead, Plutonium, Radon, Strontium, Thorium, Tritium (3H), and Uranium." *Understanding Variation in Partition Coefficient, Kd, Values*, Office of Air and Radiation, United States Environmental Protection Agency.

van Genuchten, M. T., and Wierenga, P. J. (1986). "Solute dispersion coefficients and retardation factors." *Methods of Soil Analysis, part 1, Physical and Mineralogical Methods-Agronomy Monograph No. 9 (2nd Edition)*, A. Klute, ed., American Society of Agronomy-Soil Science Socieity of America, Madison, WI, USA, 1025-1054.

Vienken, T., and Dietrich, P. (2011). "Field evaluation of methods for determining hydraulic conductivity from grain size data." *Journal of Hydrology*, 400(1), 58-71.

Zachara, J. M., Smith, S. C., Liu, C., McKinley, J. P., Serne, R. J., and Gassman, P. L. (2002). "Sorption of Cs+ to micaceous subsurface sediments from the Hanford site, USA." *Geochimica et Cosmochimica Acta*, 66(2), 193-211.

Zeng, X. (2015). "Similitude for centrifuge modelling of heavy metal migration in clay barrier and method for evaluating breakthrough time." PhD, Zhejiang University, Hangzhou, China.

SECTION

3. SUMMARIES, CONCLUSIONS AND RECOMMENDATIONS

3.1. SUMMARIES

Bio-inspired improvement on geomaterials has been investigated and innovative characterization methods have been developed in this study, which includes four phases as below:

In the first phase, EICP experiment was performed on Ottawa 50-70 sand by introducing the urea and calcium chloride solutions into evenly pre-mixed sand with urease enzyme soil sample. Non-destructive spectral induced polarization (SIP) technique was used to monitor the precipitation process during the catalytic reaction. Bender element was selected to detect the shear wave velocities of the enhanced soil. A SIP-BE column was developed in order to measure SIP and shear wave velocity simultaneously. Three conceptual association models were postulated to elucidate the relationship between precipitation characteristics and the stiffness properties of geomaterials.

In the second phase, sedimentation tests on kaolinite in NaCl and biopolymers (xanthan gum, chitosan, polyacrylic acid and polyacrylamide) solutions were conducted and recorded with time-lapsed technique up to 35 days. A comprehensive set of data, including particle size, zeta potential and solid content along the elevation of the graduated cylinders, final volume and settling velocity were obtained. The interactive mechanisms between biopolymer and kaolinite particles were elucidated.

In the third phase, tempe cell with self-developed horizontal hanging column attachment was used to determine the soil water characteristic curves (SWCC) of

uniformly sized sands initially saturated with water and polymer solutions. Air entry values predicted by the pore throat size are similar to those from parameters with van Genuchten equation. A toroidal meniscus water model, incorporating the measured surface tension and contact angle values, was proposed to calculate the volume of water in pendular regime and was compared to well-received numerical methods.

In the fourth phase, a column test setup was developed with constant hydraulic gradient and full soil sample saturation using a triaxial cell and peristaltic pump to measure the breakthrough curves of Sr and Cs for a natural silty sand. Retardation factors of the sand for Sr and Cs were determined from the breakthrough curves following USEPA's t_{50} method.

3.2. CONCLUSIONS

Conclusions from four tasks can be drawn as below:

3.2.1. Enzyme Induced Calcite Precipitation. (1) Trends of real conductivity measured from SIP test can reflect the catalytic reaction of calcite precipitation during EICP. Similar trends of outflow DC conductivity and real conductivity suggests that electrolytic DC conductivity is the major component of real conductivity in this study.

(2) The evolution of imaginary conductivity reveals information about characteristics (particle size and solid content) of precipitations. Mean particle sizes are calculated from peak frequencies and Schwarz equation; solid content obtains from the normalized chargeability parameter in Cole-Cole model of complex conductivity.

(3) Three conceptual association models are postulated: surface coating, contact cementation and pore filling. β parameters, representing the possible association patterns,

are 2/3 1 and 0 for uniform surface coating, perfect contact cementation and pore filling respectively.

(4) CaCO$_3$ crystals are more prone to precipitate and accumulate near the contact areas of sand particles in bio-mediation. Contact cementation is observed to be dominant association pattern in this study.

(5) In Darcy flow, stationary eddies forming near the pore throats among sand particles seem to be the reason that larger possibilities of CaCO$_3$ precipitates attach near the contact areas of sand particles. Those eddies can also behave as the nucleation sites for the accumulation of additional CaCO$_3$ crystals.

3.2.2. Physicochemical Studies of Polymer Modified Kaolinite Suspensions. (1) Steric repulsive force between –COO$^-$ on xanthan gum chain and the negatively-charged sites on kaolinite face hinders the bridging effect between xanthan gum and kaolinite particles in 0.001 and 0.5 g/l xanthan gum solutions. On the other hand, protons released from the –COOH functional groups of xanthan gum chains accumulated on the kaolinite edges, which enhanced the attractions between positively-charged kaolinite edges and negatively-charged chain and exhibited layered structures with edge-to-edge connections between particles. As a result, large kaolinite particles (> 900nm) were presented in 0.5 g/l xanthan gum solution.

(2) The primary interactive mechanism between kaolinite and chitosan is charge neutralization. Most positively-charged chitosan chains adsorbed onto kaolinite faces in patches at 0.05 and 5 g/l solutions, leaving the interparticle bridging effect as a secondary mechanism. As a result, most small particles (< 600 nm) were presented in 0.05 and 5 g/l chitosan solutions. Some large particles (800nm-900nm) were also detected in 5 g/l

solution, which is possibly due to the bridging effect between chitosan chains and kaolinite particles. This bridging effect is also believed to cause a higher final volume (20 ml vs. 14 ml) and slightly smaller solid contents in 5 g/l solution than in 0.05 g/l solution.

(3) Small kaolinite particles (< 600 nm) were primarily detected in PAA solutions, which is postulated to be due to the adsorption of the coiled form of positively-charged PAA chains on the alumina side of kaolinite faces. This coiled form hinders the bridging effect between PAA chains and kaolinite particles, promotes the interparticle repulsion, and leaves charge neutralization to be the dominant interaction mechanism. As PAA concentration increased, charge neutralization and the subsequent interparticle repulsive forces lead to increment of final volumes, decrement of solid contents in sediment region, and decrement of settling velocity.

(4) In both 0.1 and 0.5 g/l PAM solutions, the interactive mechanism between PAM molecule and kaolinite particles is considered to be steric stabilization in the literature. Because of the interparticle repulsive force produced by the negative PAM chains adsorbed on adjacent kaolinite edges, the particle size is small (< 600 nm). Steric stabilization is short ranged, as a result, no large aggregates were formed, the final volume is low (20 ml in 0.1 g/l and 21 ml in 0.5 g/l solutions), and the solid content is high in the sediment region.

3.2.3. Soil Water Characteristic Curve. (1) Calculated upper and lower bounds by the toroidal water model encompassed all six measured SWCCs of uniformly-sized granular materials with a wide d_{50} range (0.7 - 0.04 mm) in water, which suggests meniscus water is dominant in this case.

(2) The proposed toroidal model predicted lower water contents than the measured ones.

(3) Herschel-Bulkley fluid, surface roughness, and the possible chemical interactions (such as van der Waals interaction between the polymer solution and solid surface) could contribute to retention of aqueous solution.

3.2.4. Measurement of Retardation Factors. (1) Retardation factors of the tested sand for Sr and Cs were determined from the breakthrough curves to be 3.561 and 27.369, respectively. The distribution coefficient (K_d) of Sr and Cs, calculated from R_d values, were 0.484 and 4.986 ml/g respectively.

(2) The slightly lower R_d values recorded in this study were attributed to the lower fines content of the soil sample, high input concentrations of both Cs and Sr, and the competing monovalent and divalent cations in the influent with high ionic strength (electrical conductivity of 11.31 mS/cm).

(3) The column setup developed in this study eliminates the uncertainties from partial saturation and fluctuating pressure difference across the sample column in a traditional flow-through column test setup, and is recommended to use for future breakthrough curve measurements.

3.3. RECOMMENDATIONS

Based on the results of this study, SIP-BE testing column worked well in laboratory monitoring of EICP process. However, monitoring the MICP and biofilm remediation currently is not investigated, since the bacteria with surface charges introduced in those two modification methods might influence the electrical signals of SIP. In addition, field applications of bioremediation are suggested to be further

investigated by using SIP technique as a probable efficient monitoring tool to detect the precipitated particle sizes, solid contents and also the heterogeneity of cemented soils. Results from retardation factor measurement suggested that more breakthrough tests are still needed to further valid the proposed testing system and reveal its limitations. In order to provide more accurate retardation factors for actual field applications, radioactive matters are also suggested to be investigated in the future. In summary, the following research is recommended in the future:

(1) Monitor microbial induced calcite precipitation (MICP) and biofilm remediation in laboratory scale by SIP and bender element techniques.

(2) Apply SIP technique to actual field application on MICP, EICP, biopolymer and biofilm modifications.

(3) More measurements should be done on revealing the advantages and disadvantages of the proposed constant hydraulic conductivity and backpressured saturation column testing system. Retardation factors of radioactive matters need to be considered and measured in the future.

161

APPENDIX

PROCEDURES FOR USAGE OF SIP-BE TESTING SYSTEM

Part 1: Spectral Induced Polarization Lab Unit

Step 1: Channel connection. Select one pair of stimulus (input) and one pair of response (output) channels, connecting to the current and potential electrodes designed on the tested sample, respectively.

Step 2: Turn on the lab unit and rotate front panel current resistor selection knob to the target position (Fig. 1). Typically, the target current resistor is close to the resistivity of the tested sample.
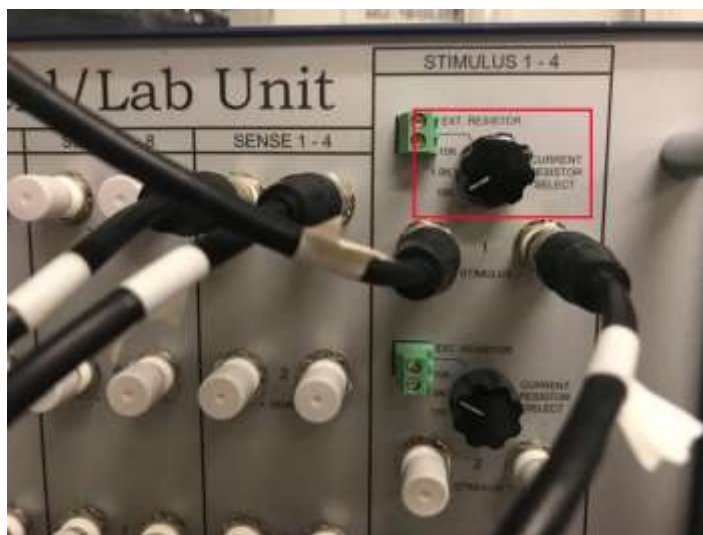
Figure 1. Current resistor selection knob.

Step 3: Open a web browser (Chrome, Firefox or Internet Explorer) and type the PSIP ip address to open the measurement software (Fig. 2).

Step 4: Input stimulus and response channel numbers in the software INPUT tool section and Channel Selection column (Fig. 2). The numbers should be the same with those for the selected pairs of measuring channels in step 1.
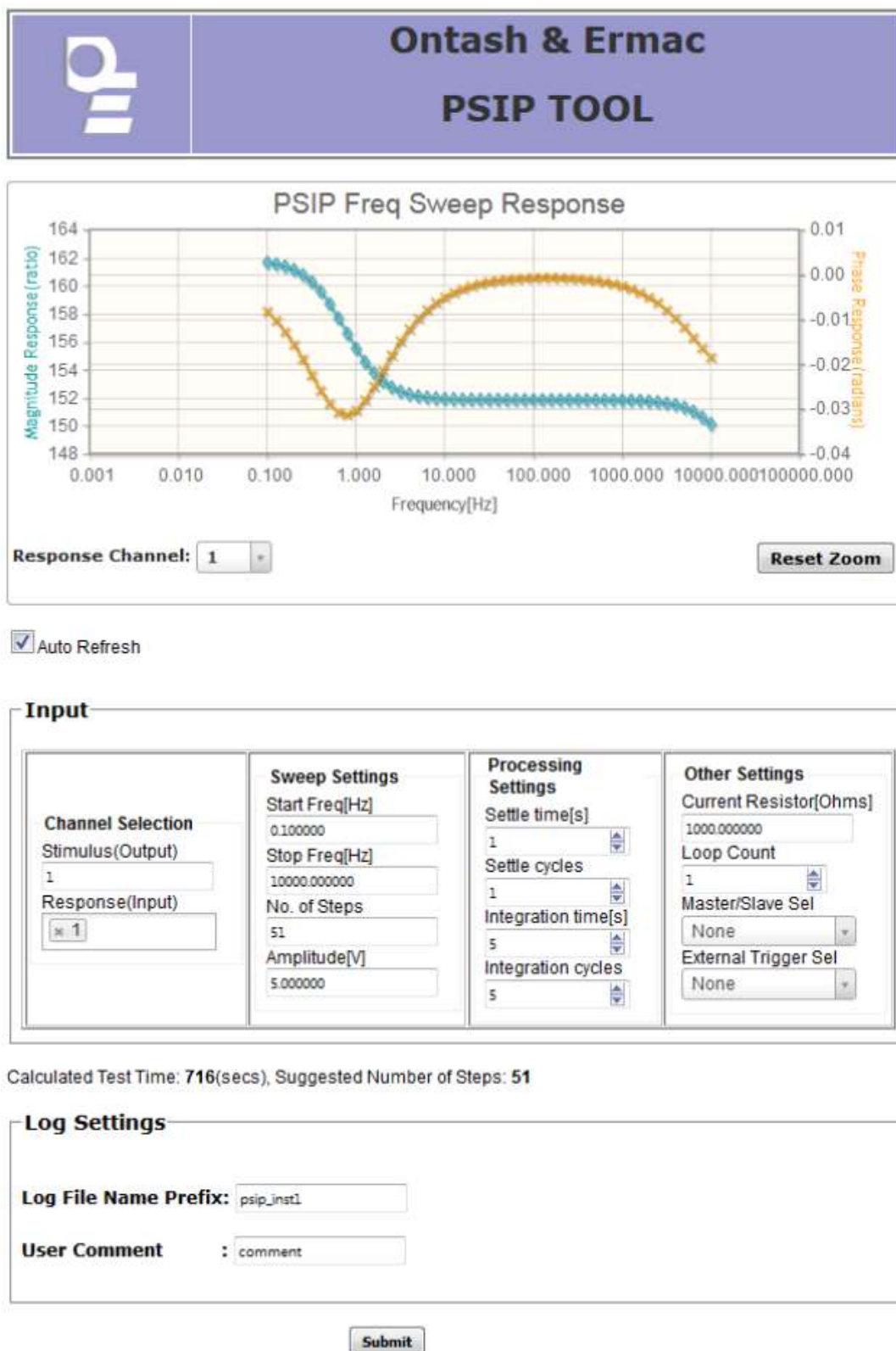
Figure 2. Example of SIP measurement software window.

Step 5: Input start and stop frequencies in INPUT tool section and Sweep Settings column (Fig. 2). How to select the proporate values of start and stop frequencies can be referred to the O&E Portable Spectral Induced Polarization (PSIP) User Guide (Ontash & Ermac, Inc.).

Step 6: Input current resistor value in INPUT tool section and Other Settings column (Fig. 2). This number should be the same with the number in step 2.

Step 7: Log file name and comments in Log Settings section (Fig. 2). Click Submit button and the SIP measurement is started.

Note: Specific meanings of the parameters shown in Fig. 2 can be reffered to the O&E Portable Spectral Induced Polarization (PSIP) User Guide (Ontash & Ermac, Inc.).

Part 2: Bender Element Testing Equipments

Step 1: Turn on the equipments. Select the specific type of the input seismic wave on signal generator equipment (Fig. 3). For example, Sine wave.

Figure 3. Signal generator.

Step 2: Click the buttons shown in the red boxes of Fig. 3, set the frequency and amplitude of the input seismic wave. Typically, the amplitude is set at 10V for soil. Frequency is selected to approximately equal the resonant frequency of the tested material.

Step 3: Set the low (H.P.) and high (L.P.) cutoff frequencies on signal filter equipment (Fig. 4). Click MODE button to switch between H.P. and L.P..
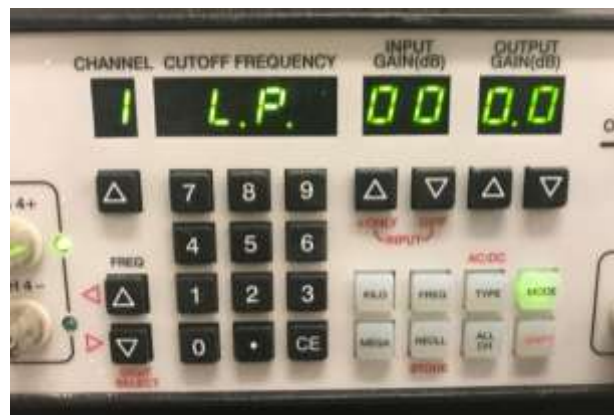
Figure 4. Signal filter and MODE button.

Step 4: Signal amplifier (Fig. 5) may be needed in case the received seismic wave is weak. Change the target amplification factor by rotating the button shown in the red box of Fig. 5.

Figure 5. Signal amplifer.

Step 5. Turn on the oscilloscope. Click BURST, TRIGGER and OUTPUT buttons on the signal generator equipment, and the received seismic wave signal will be displayed on the screen of the oscilloscope.

Note: Selection of specific frequency values can be referred to a previous study performed on investigating the performance and signal interpretation of bender elements (Lee and Santamarina 2005).

REFERENCES

ASTM D5084-16a Standard Test Methods for Measurement of Hydraulic Conductivity of Saturated Porous Materials Using a Flexible Wall Permeameter, ASTM International, West Conshohocken, PA, 2016, https://doi.org/10.1520/D5084-16A

Ates, A., 2013. The effect of polymer-cement stabilization on the unconfined compressive strength of liquefiable soils. Int. J. Polym. Sci..

Bate, B., and Burns, S. E. (2010). "Effect of total organic carbon content and structure on the electrokinetic behavior of organoclay suspensions." Journal of colloid and interface science, 343(1), 58-64.

Bate, B., and Zhang, L. M. (2013). "Use of Vacuum for the Stabilization of Dry Sand Slopes." Journal of Geotechnical and Geoenvironmental Engineering, 139(1), 143-151.

Beier, N., Wilson, W., Dunmola, A., Sego, D., 2013. Impact of flocculation-based dewatering on the shear strength of oil sands fine tailings. Can. Geotech. J.. 50, 1001-1007.

Çabalar, A. F., and Çanakci, H. (2005). "Ground improvement by bacteria." Proc, 3rd biot conference on poromechanicsA.A. Balkema, 707-712.

Cao, S. C., Bate, B., Hu, J. W., and Jung, J. (2016). "Engineering Behavior and Characteristics of Water-Soluble Polymers: Implication on Soil Remediation and Enhanced Oil Recovery." Sustainability, 8(3), 205.

Chen, R., Zhang, L., and Budhu, M. (2013). "Biopolymer Stabilization of Mine Tailings." Journal of Geotechnical and Geoenvironmental Engineering, 139(10), 1802-1807.

Dai, S., Santamarina, J. C., Waite, W. F., and Kneafsey, T. J. (2012). "Hydrate morphology: Physical properties of sands with patchy hydrate saturation." Journal of Geophysical Research, 117(B11), B11205.

DeJong, J., Martinez, B., Ginn, T., Hunt, C., Major, D., and Tanyu, B. (2014). "Development of a Scaled Repeated Five-Spot Treatment Model for Examining Microbial Induced Calcite Precipitation Feasibility in Field Applications." *Geotechnical Testing Journal*, 37, 424-435.

DeJong, J. T., Fritzges, M. B., and Nüsslein, K. (2006). "Microbially Induced Cementation to Control Sand Response to Undrained Shear." *Journal of Geotechnical and Geoenvironmental Engineering*, 132(11), 1381-1392.

DeJong, J. T., Soga, K., Kavazanjian, E., Burns, S., Paassen, L. A. v., Qabany, A. A., Aydilek, A., Bang, S. S., Burbank, M., Caslake, L. F., Chen, C. Y., Cheng, X., Chu, J., Ciurli, S., Esnault-Filet, A., Fauriel, S., Hamdan, N., Hata, T., Inagaki, Y., Jefferis, S., Kuo, M., Laloui, L., Larrahondo, J., Manning, D. A. C., Martinez, B., Montoya, B. M., Nelson, D. C., Palomino, A., Renforth, P., Santamarina, J. C., Seagren, E. A., Tanyu, B., Tsesarsky, M., and Weaver, T. (2013). "Biogeochemical processes and geotechnical applications: progress, opportunities and challenges." *Géotechnique*, 63(4), 287-301.

Di Emidio, G., Mazzieri, F., Verastegui-Flores, R. D., Van Impe, W., and Bezuijen, A. (2015). "Polymer-treated bentonite clay for chemical-resistant geosynthetic clay liners." Geosynthetics International, 22(1), 125-137.

Di Molfetta, Antonio, and Sethi, Rajandrea (2006). "Clamshell excavation of a permeable reactive barrier." Environmental Geology, 50(3)，361-369.

Espinoza, D. N., and Santamarina, J. C. (2010). "Water‐CO_2‐mineral systems: Interfacial tension, contact angle, and diffusion—Implications to CO_2 geological storage." Water Resources Research, 46(W07537).

Fredlund, D. G., Rahardjo, H., and Fredlund, M. D. (2012). Unsaturated Soil Mechanics in Engineering Practice, John Wiley & Sons.

Fredlund, D. G., Xing, A., and Huang, S. (1994). "Predicting the permeability function for unsaturated soils using the soil-water characteristic curve." Canadian Geotechnical Journal, 31, 533-546.

Javadi, S., Ghavami, M., Zhao, Q., and Bate, B. (2017). "Advection and retardation of non-polar contaminants in compacted clay barrier material with organoclay amendment." Applied Clay Science, 142, 30-39.

Jiang, N.-J., Soga, K., and Kuo, M. (2017). "Microbially Induced Carbonate Precipitation for Seepage-Induced Internal Erosion Control in Sand and Clay Mixtures." Journal of Geotechnical and Geoenvironmental Engineering, 143(3), 04016100.

Jung, J., and Jang, J. (2016). "Soil–water characteristic curve of sediments containing a polyacrylamide solution." Géotechnique Letters, 6(1), 89-94.

Hamdan, N., and Kavazanjian, E. (2016). "Enzyme-induced carbonate mineral precipitation for fugitive dust control." Géotechnique, 66(7), 546-555.

Hamdan, N., Kavazanjian, E., and O'Donnell, S. (2013). "Carbonate cementation via plant derived urease." 18th International Conference on Soil Mechanics and Geotechnical Engineering: Challenges and Innovations in GeotechnicsParis, France, 2489-2492.

Hunter, D.W., 2006. The positive impact of polymers on sediment treatment and handling. Proceedings of the Western Dredging Association Twenty-sixth Technical Conference.

Ivanov, V., and Chu, J. (2008). "Applications of microorganisms to geotechnical engineering for bioclogging and biocementation of soil in situ." Reviews in Environmental Science and Bio/Technology, 7(2), 139-153.

Kang, X., and Bate, B. (2016). "Shear Wave Velocity and Its Anisotropy of Polymer Modified High-Volume Class-F Fly Ash with Kaolinite Mixtures." Journal of Geotechnical and Geoenvironmental Engineering, 142(12), 04016068.

Kavazanjian, E., and Hamdan, N. (2015). "Enzyme Induced Carbonate Precipitation (EICP) Columns for Ground Improvement." IFCEE 2015, 2252-2261.

Kavazanjian, E., O'Donnell, S., and Hamdan, N. (2015). "Biogeotechnical mitigation of earthquake-induced soil liquefaction by denitrification: a two-stage process." 6th international conference on earthquake Geotechnical EngineeringChristchurch, New Zealand.

Kim, S., and Palomino, A. M. (2009). "Polyacrylamide-treated kaolin: A fabric study." Applied Clay Science, 45(4), 270-279.

Lee, J.-S., and Santamarina, J. C. (2005). "Bender Elements: Performance and Signal Interpretation." Journal of Geotechnical and Geoenvironmental Engineering, 131(9), 1063-1070.

Lentz, R.D., Shainberg, I., Sojka, R.E., Carter, D.L., 1992. Preventing irrigation furrow erosion with small application of polymers. Soil Sci. Soc. Am. J.. 56, 1926-1932.

Lentz, R.D., Sojka, R.E., 2000. Applying polymers to irrigation water: Evaluating strategies for furrow erosion control. Trans. ASAE. 43, 1561-1568.

Letterman, R.D., Pero, R.W., 1990. Contaminants in polyelectrolytes used in water treatment. J. AWWA. 82, 87-97.

Lin, H., Suleiman, M. T., Brown, D. G., and Kavazanjian, E. (2016). "Mechanical Behavior of Sands Treated by Microbially Induced Carbonate Precipitation." Journal of Geotechnical and Geoenvironmental Engineering, 142(2), 04015066.

Lu, N. (2016). "Generalized Soil Water Retention Equation for Adsorption and Capillarity." Journal of Geotechnical and Geoenvironmental Engineering, 142(10).

Lu, N., Kim, T.-H., Sture, S., and Likos, W. J. (2009). "Tensile Strength of Unsaturated Sand." Journal of Engineering Mechanics, 135(12), 1410-1419.

Lu, N., Wu, B., and Tan, C. P. (2007). "Tensile Strength Characteristics of Unsaturated Sands." Journal of Geotechnical and Geoenvironmental Engineering, 133(2), 144-154.

Maleki, M., Ebrahimi, S., Asadzadeh, F., and Emami Tabrizi, M. (2016). "Performance of microbial-induced carbonate precipitation on wind erosion control of sandy soil." International Journal of Environmental Science and Technology, 13(3), 937-944.

Martinez, B., and DeJong, J. (2009). "Bio-Mediated Soil Improvement: Load Transfer Mechanisms at the Micro- and Macro- Scales." Advances in Ground Improvement, 2009 US-China workshop on ground improvement technologies, 242-251.

McFarlane, A., Bremmell, K., Addai-Mensah, J., 2006. Improved dewatering behavior of clay minerals dispersions via interfacial chemistry and particle interactions optimization. J. Colloid Interface Sci.. 293, 116-127.

Mitarai, N., and Nori, F. (2006). "Wet granular materials." Advances in Physics, 55(1-2), 1-45.

Mitchell, J. K., and Santamarina, J. C. (2005). "Biological Considerations in Geotechnical Engineering." Journal of Geotechnical and Geoenvironmental Engineering, 131(10), 1222-1233.

Montoya, B. M., DeJong, J. T., Boulanger, R. W., Wilson, D. W., Gerhard, R., Ganchenko, A., and Chou, J.-C. (2012). "Liquefaction Mitigation Using Microbial Induced Calcite Precipitation." GeoCongress 2012, 1918-1927.

Mpofu, P., Mensah, A.J., Ralston, J., 2003. Investigation of the effect of polymer structure type on flocculation rheology and dewatering behavior of kaolinite dispersions. Int. J. Miner. Process.. 71, 247-268.

Nugent, R.A., Zhang, G., Gambrell, R.P.,2010. The effects of exopolymers on the erosional resistance of cohesive sediments. ICSE. 162-171.

Pefferkorn, E., 1999. Polyacrylamide at solid/liquid interfaces. J. Colloid Interface Sci.. 216, 197-220.

Puppala, A. J., Punthutaecha, K., and Vanapalli, S. K. (2006). "Soil-Water Characteristic Curves of Stabilized Expansive Soils." Journal of Geotechnical and Geoenvironmental Engineering, 132(6), 736-751.

Reddy, K. R., and Al-Hamdan, A. Z. (2013). "Enhanced Sequential Flushing Process for Removal of Mixed Contaminants from Soils." Water, Air, & Soil Pollution, 224(12), 1709.

Reddy, K. R., Al-Hamdan, A. Z., and Ala, P. (2011). "Enhanced Soil Flushing for Simultaneous Removal of PAHs and Heavy Metals from Industrial Contaminated Soil." Journal of Hazardous, Toxic, and Radioactive Waste, 15(3), 166-174.

Redmond, P., and Shackelford, C. D. (1994). "Design and Evaluation of a Flow Pump System for Column Testing." Geotechnical Testing Journal, 17(3), 269-281.

Salifu, E., MacLachlan, E., Iyer, K. R., Knapp, C. W., and Tarantino, A. (2016). "Application of microbially induced calcite precipitation in erosion mitigation and stabilisation of sandy soil foreshore slopes: A preliminary investigation." Engineering Geology, 201, 96-105.

Scalia, J., Benson, C. H., Bohnhoff, G. L., Edil, T. B., and Shackelford, C. D. (2014). "Long-term hydraulic conductivity of a bentonite-polymer composite permeated with aggressive inorganic solutions." Journal of Geotechnical and Geoenvironmental Engineering, 140(3).

van Genuchten, M. T., and Wierenga, P. J. (1986). "Solute dispersion coefficients and retardation factors." Methods of Soil Analysis, part 1, Physical and Mineralogical Methods-Agronomy Monograph No. 9 (2nd Edition), A. Klute, ed., American Society of Agronomy-Soil Science Soceity of America, Madison, WI, USA, 1025-1054.

van Paassen, L. A. (2011). "Bio-Mediated Ground Improvement: From Laboratory Experiment to Pilot Applications." Geo-Frontiers 2011.

van Paassen, L., Ghose, R., van der Linden, T., van der Star, W., and van Loosdrecht, M. (2010). "Quantifying Biomediated Ground Improvement by Ureolysis: Large-Scale Biogrout Experiment." Journal of Geotechnical and Geoenvironmental Engineering, 136(12), 1721-1728.

Wang, C., Chen, K.Y., 1977. Laboratory study of chemical coagulation as a means of treatment for dredged material (Technical Report - U.S. Army Engineer Waterways Experiment Station). Vicksburg, MS.

Weil, M., DeJong, J., Martinez, B., and Mortensen, B. (2012). "Seismic and Resistivity Measurements for Real-Time Monitoring of Microbially Induced Calcite Precipitation in Sand." *Geotechnical Testing Journal*, 35(2), 330-341.

Whiffin, V. S., van Paassen, L. A., and Harkes, M. P. (2007). "Microbial Carbonate Precipitation as a Soil Improvement Technique." *Geomicrobiology Journal*, 24(5), 417-423.

Yeom, S. H., Daugulis, A. J., and Lee, S. H. (2010). "Bioremediation of phenol-contaminated water and soil using magnetic polymer beads." Process Biochemistry, 45(9), 1582-1586.

Zhao, Q., Choo, H., Bhatt, A., Burns, S. E., and Bate, B. (2017). "Review of the fundamental geochemical and physical behaviors of organoclays in barrier applications." Applied Clay Science, 142, 2-20.

VITA

Junnan Cao was born in Yantai, China. She got her bachelor's degree in Civil Engineering in 2010 from Shandong University of Science and Technology, with excellent graduate honor. In 2013, she received her master of science in Civil Engineering (Geotechnical Engineering) from Tianjin University, China. After that, she went to Missouri University of Science and Technology, USA to pursue the doctor of philosophy (Ph.D) degree in Civil Engineering (Geotechnical Engineering). In December 2018, she received the Ph.D. degree in Civil Engineering from Missouri University of Science and Technology.